# **Interfacing Rydberg Atoms with a High Overtone Bulk Acoustic Wave Resonator on an Atom Chip**

## Samuel Germer

Masterarbeit in Physik angefertigt im Institut für Angewandte Physik

vorgelegt der Mathematisch-Naturwissenschaftlichen Fakultät der Rheinischen Friedrich-Wilhelms-Universität Bonn

October 2025

I hereby declare	that this t	thesis was	formulated	by myself	and tha	t no s	sources	or tools	other	than t	hose
cited were used											

Bonn, ...06.10.2025 ... Date

Signature

1. Gutachter: Prof. Dr. Sebastian Hofferberth

2. Gutachter: Prof. Dr. Daqing Wang

# **Contents**

1	Intro	oductio	n e e e e e e e e e e e e e e e e e e e	1				
2	High	High-Overtone Bulk Acoustic Wave Resonator						
	2.1	Funda	mental Working Principles	5				
		2.1.1	Acoustic Waves in Crystals	5				
		2.1.2	Piezoelectricity	9				
		2.1.3	Quantization of Acoustic Modes	11				
		2.1.4	Acoustic Modes of an HBAR	13				
		2.1.5	Single-Phonon Acoustic Fields	14				
	2.2	Analyt	tic Electric Field Model	16				
		2.2.1	Quasistatic Approximation	17				
		2.2.2	The Total Polarization inside the Piezoelectric Resonator	17				
		2.2.3	The Electric Field above the Piezoelectric Resonator	19				
		2.2.4	Scaling Laws of the Electric Field Strength and Effects of Dielectric Substrate.	21				
	2.3	Numer	rical Simulations	22				
		2.3.1	FEM Electrostatic Simulation: Setup	23				
		2.3.2	FEM Electrostatic Simulation: Results	26				
		2.3.3	FEM Eigenfrequency Simulation: Setup	30				
		2.3.4	FEM Eigenfrequency Simulation: Results	36				
	2.4	High-(	Q HBARs for the HQO Experiment	40				
	2.5	Toward	ds an Implementation into the Experiment	42				
3	Inte	rfacing	Rydberg Atoms with an HBAR	45				
	3.1	Coupli	ing Rydberg Atoms to an HBAR Mode	45				
		3.1.1	Scaling of Coupling Strength with Transition Frequency	47				
		3.1.2	Coupling Strength for the $85S_{1/2} \leftrightarrow 85P_{3/2}$ Transition	47				
	3.2	Rydbe	rg Atoms as a Refrigerant for Ground State Cooling of an HBAR Mode	48				
		3.2.1	Coupled Atom-Resonator System	49				
		3.2.2	Cooling with Single Rydberg Atoms	50				
		3.2.3	Cooling with Rydberg Superatoms	53				
	3.3	Simula	ation of the Cooling Process	54				
		3.3.1	Superatom HBAR Cooling Scheme	55				
		3.3.2	Simplified Superatom HBAR Cooling Scheme	59				
	3.4	Experi	imental Implementation	65				

4	Ator	n Chip	Characterization	67				
	4.1 Overview of Atom Chip Design							
	4.2	Coplai	nar Waveguide Resonator Characterization	68				
		4.2.1	Dependence of Resonance Frequency on System Parameters	69				
		4.2.2	Designed Resonator Versions	72				
		4.2.3	Measurement Method	73				
		4.2.4	Measured Resonance Spectra	73				
		4.2.5	Extraction of Resonator Parameters from Measurement Data					
	4.3	Trapping Wire Characterization						
		4.3.1	Chip Mounting and PCB Design	81				
		4.3.2	Measurement Requirements and Estimates	82				
		4.3.3	Sensing and Protection Circuit					
		4.3.4	Measurement Procedure	85				
		4.3.5	Results and Discussion	88				
5	Con	clusior	n and Outlook	91				
A	App	endix		93				
	<b>A.</b> 1	FEM I	Eigenfrequency Study: Mesh Refinenment of inner Quad Mesh of HBAR	93				
	A.2	A.2 Cooling Simulations: System Hamiltonian						
	A.3	3.3 Statement on Digital Tools and AI Assistance						
Bi	blioa	raphy		96				

# Introduction

A trend in modern quantum physics is the development of hybrid quantum systems [1, 2]. Here, distinct physical platforms are interfaced with each other to leverage complementary advantages [2]. By coupling distinct physical platforms—such as atoms to photons [3], atoms or spins to microwave circuits [4, 5], or mechanical resonators to superconducting qubits [6], these platforms aim to engineer functionalities that exceed those of their individual components [7]. Such hybrid platforms span a broad spectrum of functionalities [1] — including, but not limited to, quantum memories [8, 9], microwave—optical transducers [10, 11], integration of neutral-atom arrays with nanophotonic chips to explore strongly interacting light—matter systems [12], or coupling collective spin excitations to other physical platforms [13]. In this context, Rydberg atoms [14] and high-overtone bulk acoustic wave resonators (HBARs) [15] represent two complementary platforms. An interface between these two systems could enable coherent information transfer between atomic and mechanical degrees of freedom, opening new opportunities in quantum information processing.

Rydberg atoms are highly excited atoms with exaggerated physical properties [14], making them promising for various applications in quantum technologies [16] and fundamental physics research [17–20]. Rydberg experiments have been carried out with a wide range of atomic species [21–24], prominently with Rubidium [25–28], and more recently with a dual-species platform [29]. They offer a broad band of transitions, ranging from the optical regime to microwave frequencies [16]. Their large electric dipole moments and static polarizabilities enable high sensitivity to microwave [30–32] and static fields [33], respectively. It makes them suitable for precision electrometry and sensing applications. Apart from external fields, Rydberg atoms exhibit strong interactions with each other [16, 34–36], which can be harnessed for entanglement gates in neutral atom quantum computers [37, 38] or used to study dynamics of collective quantum systems [25, 39], using the Rydberg blockade effect [36, 40]. Despite their high sensitivity to external disturbances, Rydberg states can have long lifetimes on the ms timescale [41]. At room temperature, the lifetime is limited by blackbody radiation-induced transitions to other Rydberg states [42, 43], but in a cryogenic environment, lifetimes of several milliseconds can be achieved [44]. Rydberg atoms are thus well suited for applications requiring long coherence, high sensitivity, and transitions in both the microwave and optical domains [16].

A fundamentally different branch of quantum physics is quantum acoustics, which studies quantized vibrations, called phonons, in (macroscopic) mechanical resonators and their interactions with other quantum systems [6, 45]. Contrary to single atoms, the dynamics inside a mechanical resonator emerge from collective motion of many atoms inside the solid material [46]. There are many types

of mechanical resonators like optomechanical membranes [47] or engineered nanobeams [48], which operate at a few MHz. However, they are not limited to that as there are devices operating – like Rydberg atoms – at microwave frequencies [15, 49]. One of these devices is a High Overtone Bulk Acoustic Wave Resonator [6] which consists of a bulk material that can host long-lived [15], high overtone acoustic modes, typically in the 5 – 10 GHz frequency range [6, 50]. Lifetimes of several milliseconds have been demonstrated at GHz frequencies in cryogenic environments [50] as well as cooling to the quantum-mechanical ground state [50]. These devices are promising for fundamental physics research, e.g., probing quantum gravity [51], generating squeezed states for quantum sensing applications [52] and multi-phonon Fock states [53]. Furthermore, they are of interest for quantum technologies like superconducting qubit interfaces [6, 53], directly using it as an acoustic qubit [54], bidirectional microwave-to-optical transduction [10] or coupling to vacancy centers in diamond [45, 55]. In these experiments, the coupling is typically mediated by a piezoelectric layer on top of the resonator that converts acoustic motion into an electric field [6].

In the Nonlinear Quantum Optics group, interactions of Rydberg atoms with light at the level of single photons are studied [25–28]. Building on this expertise, the Hybrid Quantum Optics (HQO) experiment aims to extend these studies from single photons to single phonons by interfacing rubidium-87 Rydberg atoms with an HBAR via the piezoelectric effect [56]. This approach aims to combine the advantages of both systems, leveraging the strong interactions and long coherence times of Rydberg atoms with the high quality factors and GHz operation frequencies of HBARs. As a first goal, the experiment will focus on trying to cool an HBAR to its quantum mechanical ground state, using the Rydberg atoms as an active cooling agent.

To realize the interaction between Rydberg atoms and an HBAR, several key requirements must be met. First, both systems must operate in a low temperature environment. For Rydberg atoms, blackbody-induced transitions limit the lifetime at room temperature [42, 43], while for HBARs, phonon lifetimes are reduced and thermal phonon occupation is high in the resonator [15]. A cryogenic environment is therefore essential to achieve long atomic coherence times [44], high mechanical quality factors [50], and a low thermal phonon occupation of the resonator. Second, the atoms must be brought close to the resonator surface to ensure sufficient coupling to the evanescent electric field of the HBAR mode. This requires trapping ultracold atoms (in the  $\mu$ K regime) close to the resonator surface (at distances of  $\sim 35-50\,\mu\text{m}$ ). Third, excitation of the atoms to a Rydberg state demands narrow-linewidth laser systems at the relevant optical transition frequencies [57, 58].

The HQO experiment is designed to meet these requirements by combining a cryostat, providing a base temperature of 4 K, with an atom chip that integrates both a superconducting magnetic wire trap [59] and the HBAR. This architecture enables magnetic trapping and manipulation of cold rubidium-87 atoms directly above the resonator surface in a compact and fully cryo-compatible platform. A set of lasers at 780 nm, called probe laser, and 480 nm, called control laser, provide the ability for Rydberg excitation of rubidium-87.

The preparation of cold atoms, transport to the experiment, and subsequent Rydberg excitation have been implemented [60, 61]. In addition, a first-generation atom chip—without the HBAR—was designed and fabricated, incorporating a superconducting niobium wire trap and a superconducting niobium coplanar waveguide resonator to test atom trapping, Rydberg excitation, and microwave coupling [62]. Building on this, the present thesis pursued three key objectives to advance the system toward HBAR integration. The objectives were to characterize the fabricated atom chip, to quantitatively understand the coupling between Rydberg atoms and an HBAR, and to simulate HBAR cooling with Rydberg atoms. The results will guide the development of a second-generation atom chip integrating the HBAR.

In this thesis, the properties of HBARs are introduced in Chapter 2, and the coupling mechanism between Rydberg atoms and the HBAR via the piezoelectric effect is explained in Sections 2.1.2 and 2.2. This ultimately leads to quantitative results for the single phonon evanescent electric field that can couple to the Rydberg atoms in dependence of the tunable system parameters in Section 2.3.2 and the expected single phonon Rabi frequency in Section 3.1. Having established realistic parameters, Chapter 3 presents simulations of cooling the HBAR with collective Rydberg excitations, based on a master equation approach. The results in Section 3.3.2 will show that ground-state cooling of the HBAR is feasible with realistic experimental parameters and that a single collective excitation coupled to the HBAR is superior in terms of cooling performance compared to a single excited Rydberg atom coupled to it. Lastly, Chapter 4 discusses the characterization of the fabricated atom chip in terms of its microwave resonator properties and its magnetic trapping capabilities. Chapter 5 gives a summary of this thesis and an outlook for the experiment.

# **High-Overtone Bulk Acoustic Wave Resonator**

As outlined in the introduction, the aim of the HQO experiment is to interface Rydberg atoms with a high-overtone bulk acoustic wave resonator (HBAR). An HBAR is an acoustic resonator in which the wavelength of the supported acoustic modes is much smaller than the thickness of the substrate, leading to the existence of high-overtone (longitudinal) modes inside of it. In the following, we focus on a specific HBAR implementation developed in the group of Yiwen Chu [6, 46, 53, 54]. A schematic sketch of this device is shown in Fig. 2.1 (note that this coordinate system will be used throughout this Chapter without explicitly introducing it again). It consists of a  $\sim 400 \, \mu m$  thick sapphire substrate and a thin ( $\sim 1 \, \mu m$ ) Aluminium Nitride dome on top. Through the curved shaped of the dome that acts as a curved mirror for acoustic waves, the HBAR can host long-lived modes. A Gaussian mode inside the resonator is sketched in the top right inset of Fig. 2.1. These devices reach high mechanical quality factors, exceeding values of  $Q \sim 10^7$  [54] which results in linewidths below 1 kHz [54] around resonance frequencies of 6 GHz. These are in the same range as the natural linewidths of Rydberg states with n around 80 in rubidium [63].

Because the dome (AlN) is a piezoelectric material, an oscillating acoustic mode inside this dome that induces a periodic deformation of the material will generate an oscillating electric field above the surface via the piezoelectric effect [6]. This mechanism is commonly used to couple HBARs to superconducting qubits [6]. In our experiment, we aim to extend this approach to a different physical platform by positioning Rydberg atoms in close proximity to the dome surface, allowing them to couple to the electric field of the acoustic mode.

In the following, we establish the physics of the HBAR and show how the piezoelectric effect enables its acoustic mode to couple to a Rydberg atom. We then construct an analytical model of the resulting oscillating electric field, extracting its scaling behaviour with respect to important system parameters. Finally, we perform a quantitative simulation of the electric field generated by a single phonon at the atomic position, providing the input required for the coupling-strength calculation in Chapter 3. After this, real HBARs for the experiment are discussed in Section 2.4 (for readers interested only in the key simulation results, see Section 2.3.2; for an overview of a possible experimental implementation, see Section 2.5 instead).

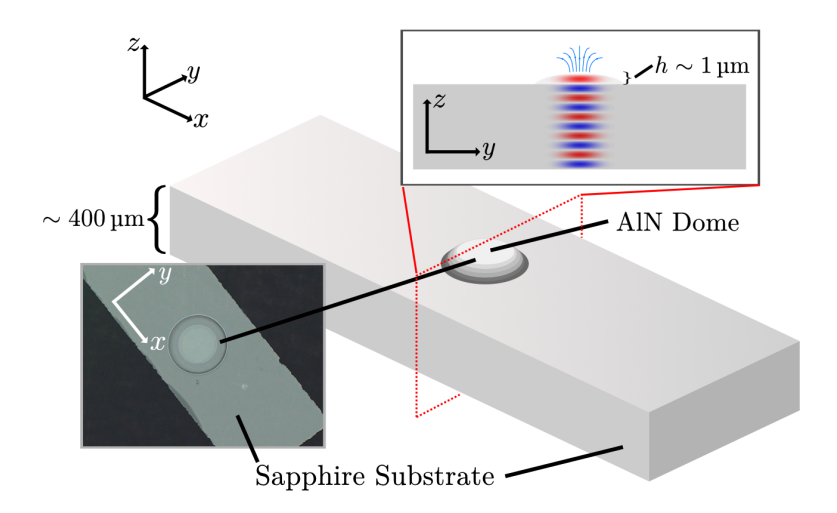


Figure 2.1: Sketch of an HBAR of same type as used in Ref [46]. It consists of a  $\sim 400 \, \mu m$  thick sapphire substrate and a curved dome on top (of height  $\sim 1 \, \mu m$ , half an acoustic wavelength), made out of Aluminium Nitride, which is a piezoelectric material. The top right inset shows an acoustic mode (strain) inside a cut through the *zy*-plane (dashed red square) of the HBAR. The red-blue pattern symbolizes the longitudinal strain amplitude inside the HBAR. The curved dome acts like a curved mirror that confines the acoustic mode inside the resonator. Because of the piezoelectric effect, the dome generates an oscillating electric field above itself. The bottom left inset (Image courtesy Raquel Garcia, ETH Zurich) shows a top view from a real device with an AlN dome which will be described in more detail in Section 2.4.

## 2.1 Fundamental Working Principles

In order to understand the physics of high-overtone bulk acoustic wave resonators (HBARs), it is useful to review some important theoretical concepts. The starting point is the description of acoustic wave propagation in crystalline solids, which can be formulated within the framework of linear elasticity theory. On this basis, we introduce the principles of piezoelectricity, which explain how mechanical strain in a crystal is coupled to an electric field. In the context of our experiment, this mechanism is essential because it allows the resonator to generate an oscillating electric field that can be coupled to the Rydberg atoms. After introducing piezoelectricity, we discuss how acoustic modes in such resonators can be quantized, and finally examine the types of modes that are present in the HBAR of interest to be able to quantitatively describe the acoustic modes as sketched in Fig. 2.1.

#### 2.1.1 Acoustic Waves in Crystals

In this section, we will investigate how acoustic waves propagate in crystals, specifically in anisotropic media, in order to understand how they propagate in the HBAR. To do so, we will begin with a brief introduction to linear elasticity theory to familiarize ourselves with the relevant physical quantities. Afterwards, we will review the acoustic wave equation in an anisotropic medium to understand how waves propagate there.

#### **Linear Elasticity Theory**

When one has a look inside a crystal, depending on the resolution, one can see individual atoms arranged in some periodic structure. Separations between individual atoms are typically on the order of a few Å [64]. In sapphire for example, the distances between atoms are about 2 Å [65]. However, the acoustic wavelength of waves in the GHz regime in sapphire is on the order of a few  $\mu m$  [6], which is about 1000 times larger. This means that we can use a continuum approximation, where individual atoms are not resolved, to describe the propagation of acoustic waves in crystals [64]. In this approximation, we can describe the crystal as a continuous medium with a density  $\rho$  and a displacement field  $\vec{u}(\vec{x},t)$ , which describes the displacement of the medium at position  $\vec{x}$  and time t. We further make the assumption that deformations inside the material are small. This means that we are in a regime where the deformation is linearly proportional to an applied force. In microscopic terms this means that individual atoms are displaced only by a small distance from their equilibrium position where the potential can be approximated to be harmonic [64]. This is known as the linear elasticity regime.

There are three important quantities to describe the state of an approximately continuous medium at a given point  $(\vec{x}, t)$ : The displacement field  $\vec{u}(\vec{x}, t)$ , the strain tensor  $S_{ij}(\vec{x}, t)$  and the stress tensor  $T_{ij}(\vec{x}, t)$  [66]. In the following, an introduction to these quantities and how they are related to each other is given based on refs. [64, 67].

First we consider an elastic body in a cartesian coordiate system where we look at a reference point p at position  $(x_1, x_2, x_3)$ . If this body undergoes a translation and/or a small deformation and/or a rotation, a point p is displaced from its original position to a new point p'. If the material is deformed non-uniformly, this displacement must be described uniquely at each point  $\vec{x}$  inside the body. This is done using the displacement field  $\vec{u}(\vec{x})$ , which is defined as the difference between the new position  $\vec{x}'$  and the old position  $\vec{x}$ :

$$\vec{u}(\vec{x}) = \vec{x}' - \vec{x} = u(\vec{x})\hat{e}_x + v(\vec{x})\hat{e}_y + w(\vec{x})\hat{e}_7. \tag{2.1}$$

Here,  $\hat{e}_i$  is the *i*-th component of the unit vector and (u, v, w) describe the displacement amplitudes in all three dimensions. The notation with  $\vec{u} = (u, v, w)$  is used as it is a very common notation in the literature and for example used in finite element simulation software like COMSOL [68], which we will use at a later point. Microscopically, the displacement field would describe how much an atom is displaced from its equilibrium position.

It is not only of interest to look at the displacement of single points in space, but also how the distance between two points changes when the body is deformed. This is described by the strain tensor  $S_{ij}$ . To understand this quantity, we have to look at how an infinitesimal line element  $d\vec{x}$  between point p and q changes when the body is deformed. If we displace point p to p' by  $\vec{u}(\vec{x})$  and point q to q' by  $\vec{u}(\vec{x} + d\vec{x})$  we can write

$$\vec{u}(x_i + dx_i) = \vec{u}(x_i) + \frac{\partial u_i}{\partial x_i} dx_j + O(dx^2) , \qquad (2.2)$$

under the assumption that the displacement field is differentiable. The new line element is then given by

$$dx_i' = dx_i + \frac{\partial u_i}{\partial x_j} dx_j . {(2.3)}$$

We can split the derivative into a symmetric and an antisymmetric part:

$$\frac{\partial u_i}{\partial x_j} = \frac{1}{2} \left( \frac{\partial u_i}{\partial x_j} + \frac{\partial u_j}{\partial x_i} \right) + \frac{1}{2} \left( \frac{\partial u_i}{\partial x_j} - \frac{\partial u_j}{\partial x_i} \right) = S_{ij} + A_{ij} , \qquad (2.4)$$

where  $S_{ij}$  is the symmetric part and  $A_{ij}$  is the antisymmetric part. The symmetric part is known as the strain tensor, which describes how much the body is deformed, while the antisymmetric part describes how much it is rotated [67]. In the following, we will only look at the strain tensor as we are not interested in rotations in this context. As for the displacement field, the strain tensor will also have different values at different space points when dealing with nonuniform deformations. It is a second rank tensor, which means that it has nine components, but only six of them are independent due to the symmetry of the tensor  $S_{ij} = S_{ji}$  [67].

Having defined the strain tensor, we have to look at another quantity which is the cause of the deformation, namely the stress tensor  $T_{ij}$ . The stress is defined as the force per unit area inside the body where i represents the direction of the force and j the normal direction of the plane where the force is applied [64]. As for the strain tensor, the stress tensor also only has six independent components  $(T_{ij} = T_{ji})$ . As already mentioned, we are only interested in small deformations, which means that the stress is linearly proportional to the strain. This can be written as:

$$T_{ij} = c_{ijkl} S_{kl} \tag{2.5}$$

$$S_{ij} = S_{ijkl} T_{kl} , \qquad (2.6)$$

where  $c_{ijkl}$  is the stiffness tensor (or sometimes called elasticity tensor) and  $s_{ijkl}$  is the compliance tensor [67]. The stiffness tensor describes how much stress is needed to create a certain strain, while the compliance tensor describes how much strain is created by a certain stress. The stiffness tensor is a fourth rank tensor, which means that it has 81 components, but only 21 of them are independent due to the symmetry of the tensor [67]. The compliance tensor is also a fourth rank tensor with 21 independent components. In following calculations we will only deal with the stiffness tensor. However, it is good to know about the compliance tensor. For example, in finite element simulations with COMSOL, one has to choose between the stiffness tensor and the compliance tensor [69], which is why it is mentioned here. The stiffness tensor and the compliance tensor are material properties and depend on the composition and internal structure of the material. While the stiffness tensor and the compliance tensor can have up to 21 independent components, this is not always the case as material properties such as crystal symmetries may introduce additional bounds on the tensor components. In case of a completely isotropic material, the stiffness tensor can be reduced to only two independent components, which are the bulk modulus and the shear modulus [67].

#### **Acoustic Wave Equation**

In the previous section, we have introduced the basic concepts of linear elasticity theory and how to describe the state of a medium with the displacement field, strain tensor and stress tensor. In this section, we will need these concepts to understand how acoustic waves propagate in a medium.

We start by writing down the equation of motion for a small volume element in the medium, which is

given by Newton's second law [67]:

$$\rho \frac{\partial^2 u_i(\vec{r})}{\partial t^2} = \frac{\partial T_{ij}(\vec{r})}{\partial x_j} + f_i(\vec{r}) , \qquad (2.7)$$

where  $f_i(\vec{r})$  are external forces acting on the body like for example gravity. In the case of acoustic waves, we assume that there are no external forces acting on the body that need to be considered, which means that  $f_i(\vec{r}) = 0$ . Next, we can use the relation between stress and strain given in Eq. (2.5) and the relation between strain and displacement given in Eq. (2.4) to rewrite the equation of motion as:

$$\rho \frac{\partial^2 u_i}{\partial t^2} = c_{ijlm} \frac{\partial^2 u_m}{\partial x_j \partial x_l} . \tag{2.8}$$

This is the acoustic wave equation in an anisotropic medium, which describes how acoustic waves propagate in a medium with a given stiffness tensor  $c_{ijkl}$  and material density  $\rho$ . Solutions of this equation are of the form [70]:

$$\vec{u}(\vec{r},t) = u_0 \hat{n}_{\text{pol}} e^{i(\vec{k}\cdot\vec{r} - \omega t)} , \qquad (2.9)$$

where  $u_0$  is the amplitude of the wave,  $\vec{k}$  is the wave vector and  $\omega$  is the angular frequency of the wave. The wave vector describes the direction of propagation by  $\vec{k} = k\hat{n}$  where  $\hat{n}$  is a unit vector in the direction of propagation and k is the absolute wave number. The direction of the displacement field of the wave is called the polarization of the wave as given by  $\hat{n}_{pol}$ . We can insert Eq. (2.9) into Eq. (2.8) and end up with the following equation which is known as the Christoffel equation [67]:

$$\left(\frac{c_{ijkl}}{\rho}n_jn_k - v^2\delta_{il}\right)u_{0l} = 0, \qquad (2.10)$$

where  $v = \omega/k$  is the phase velocity of the wave and  $n_{j,k}$  are the j,k-th component of the propagation direction unit vector  $\hat{n}$ . The nontrivial solutions determine the dispersion relation of the acoustic wave. For each propagation direction  $\hat{n}$ , there are three solutions for the eigenvectors corresponding to three possible polarizations  $\hat{n}_{pol}$  with corresponding eigenvalues determining the phase velocities of the wave, which means that there are three different acoustic modes that can propagate in the medium given a specific direction of propagation. In most cases, the polarizations of the eigenmodes are not perfectly longitudinal or transversal as for an isotropic medium, one calls the modes that closest resemble them to be quasi transversally and quasi longitudinally polarized. This dispersion relation is very similar to birefringence in optics, where the refractive index depends on the propagation direction and polarization of the light. The practical consequences of Eq. (2.10) will come clear when we discuss the acoustic modes of the HBAR in Section 2.1.4.

#### **Voigt Notation**

Before looking into the theory of piezoelectricity, we will discuss a notation to write the introduced acoustic quantities in a more compact form, which is useful for numerical simulations and analytical calculations. We will also make use of this notation later. In this notation, the strain and stress tensors are written as vectors with six components which is possible because of their symmetry properties [67]. The stiffness tensor is then written as a matrix with  $6 \times 6$  components. This simplified notation is called

Voigt notation. The Voigt notation replaces the Cartesian coordinate subscripts of the strain (stress) tensor with numbers. The notation is defined as follows [67] (stress and compliance follow analogously):

$$1 \equiv xx$$
,  $2 \equiv yy$ ,  $3 \equiv zz$ ,  $4 \equiv yz$ ,  $5 \equiv xz$ ,  $6 \equiv xy$ . (2.11)

This means, for the strain tensor components:

$$S_1 = S_{xx}, \quad S_2 = S_{yy}, \quad S_3 = S_{zz},$$
 (2.12)

$$S_4 = 2S_{yz} = 2S_{zy}, \quad S_5 = 2S_{xz} = 2S_{zx}, \quad S_6 = 2S_{xy} = 2S_{yx}.$$
 (2.13)

The stiffness coefficients  $c_{ijkl}$  are mapped to  $c_{mn}$  (6 × 6 matrix) in Voigt notation. Symmetries reduce the number of independent components to 21, meaning a symmetric matrix [67].

$$c_{ijkl} = c_{jikl} = c_{ijlk} = c_{jilk} = c_{klij} = c_{lkij} = c_{lkji} = c_{lkji} . (2.14)$$

In the following sections we will always specify whether we use Voigt or tensor notation.

#### 2.1.2 Piezoelectricity

Piezoelectricity is a property of certain materials to induce a polarization when mechanically stressed. This is known as the direct piezoelectric effect [71]. Of course, this effect is reversible and can also be used to induce a mechanical stress when an electric field is applied, which is known as the converse piezoelectric effect. In the following, we will look into the direct piezoelectric effect in more detail to understand how we can use it to couple an atom, which would normally only interact with electromagnetic fields, to an acoustic field.

Whether a material is piezoelectric depends on the internal structure, namely the microscopic charge distribution. To be more precise, a medium needs to lack inversion symmetry to be piezoelectric [72]. To understand this we can assume a crystal where we apply a stress and therefore polarize it. If we now assume that the crystal has an inversion center, and we invert the crystal and the applied stress, the crystal and the stress will not change [72], but the polarization (a vector quantity) will point into the opposite direction. This can only work in case the polarization is equal to zero meaning that the crystal has no piezoelectric properties. Microscopically this means that each microscopic dipole has a twin that points into opposite direction, and they cancel each other out. One simple example is shown in Fig. 2.2 where the distribution of charges has no inversion center. The deformation of the material leads to a deformation of the charge distribution which leads to a polarization of the material. This very simple example also shows that the polarization vector does not necessarily point in the same direction as the applied stress.

#### **Constitutive Relations**

Knowing the origin of piezoelectricity, we have to formulate this effect mathematically as we are interested in the coupling between the HBAR and an atom via the piezoelectric effect in a quantitative way (we will use Voigt noation for this). The direct piezoelectric effect can be described by

$$P_{p,i} = e_{im} S_m , \qquad (2.15)$$

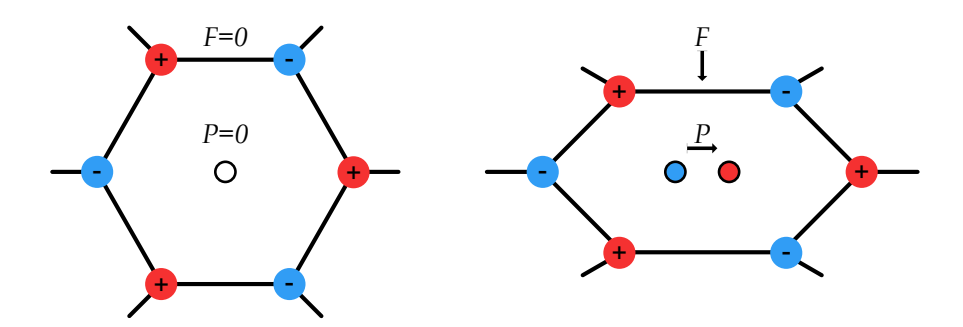


Figure 2.2: Image shows a simple example of piezoelectricity. The left image shows a charge distribution with positive (red) and negative (blue) charges. No force  $\vec{F}$  is acting on the structure and the center of positive and negative charges coincide (white circle in the middle). The right images shows the same structure but with a force applied from the top which leads to a deformations. The center of positive and negatice charges are shifted in opposite directions (red and blue circles in the middle), which leads to a net polarization  $\vec{P}$  of the structure. Example is adapted from [73].

where  $P_{p,i}$  is the *i*-th component of the strain induced polarization vector  $\vec{P}_p$ ,  $e_{im}$  is the piezoelectric tensor in Voigt notation which characterizes how strong a strain has to be to induce a certain polarization and  $S_m$  is the strain in Voigt notation. As we already saw in the simple example from Fig. 2.2 the polarization vector does not necessarily point in the same direction as the applied strain, which is why we have to use a tensor to describe this quantity. As for the stress-strain relation, we assume to be in a regime where the polarization is linearly proportional to the strain in the material.

Since we are still in an elastic and dielectric material, we can not only consider the strain induced polarization alone but also have to take into account the polarization induced by the internal electric field as well as the strain induced by an external stress. Combining these effects is described by the constitutive relations (in the so called stress-charge form) [74]:

$$T_i = c_{ij}^E S_j - e_{mi} E_m (2.16)$$

$$D_i = e_{ij}S_j + \epsilon_{ij}^S E_j , \qquad (2.17)$$

where  $T_i$  is the i-th component of the stress,  $D_i$  is the i-th component of the electric displacement field,  $c_{ij}^E$  is the stiffness tensor  $\epsilon_{ij}^S$  is the permittivity tensor and  $E_i$  is the i-th component of the electric field. The superscript E in  $c_{ij}^E$  and the superscript S in  $\epsilon_{ij}^S$  indicate that these quantities are measured at constant electric field and constant strain, respectively. This is important to note as the tensor components differ from the case where they would be measured at constant stress and constant electric displacement field. We can understand this easily for the stiffness tensor. Suppose we have a piezoelectric material between two metal electrodes (like a plate capacitor). If we connect the electrodes, the electric field inside will be constant (zero) as any strain induced surface charges are cancelled out by free moving charges. We can measure the stiffness tensor in this case by applying stress and measuring the strain to get  $c^E$ . If we now disconnect the electrodes, strain induced surface charges can not be cancelled out anymore because there are no free charges that can flow between the electrodes. This means constant displacement field (zero) but not constant electric field. If we now apply a stress, the material appears more stiff since the induced

polarization is not cancelled out by free charges anymore and counteracts the applied stress. We would now measure  $c^D \ge c^E$ . Whethere this distinction is important depends on the material, but in the case of aluminum nitride (AlN), which we will use in the HBAR, the difference can be neglected [75, 76]. However, it is important to know this destinction to not be confused when looking at material constants in literature.

Another thing to note is that solving these equations to obtain a specific quantity of interest, like the total polarization, is in general not trivial and depends on the exact boundary conditions. We will later see in Section 2.2 that we can make valid approximations to use Eq. (2.17) to calculate the total polarization to calculate the generated electric field that couples to an atom.

#### **Piezoelectricity in Aluminium Nitride**

We now understand the requirement for a material to be piezoelectric, namely that it lacks inversion symmetry, and how to describe this effect mathematically. In this section, we will take a look at the piezoelectric properties of aluminum nitride (AlN), which is the material used in the HBAR to be later able to understand the shape and strength of the generated electric field above the HBAR.

Fig. 2.3 shows the crystal structure of AlN. It is orgainzed is a so called "wurtzite"-structure [77]. This is a hexagonal crystal structure where both Al and N atoms are arranged in a hexagonal structure with alternating layers of Al (cation) and N atoms (anion). As one can see from this Figure, the two species of atoms are displaced in the z-direction in such a way that it lacks an inversion center along this axis. Looking at an Al ion surrounded by four N ions and vice versa and realize that the center of charges do not coincide (two different bond lengths) which results in a nonzero spontaneous polarization along the z-direction and the ability to generate an additional polarization when mechanically stressed in this direction [77].

Returning to Fig. 2.3 we can see that the z-axis is labeled as the c-axis (name in literature), the material is normally grown along this axis. AlN has three independent piezoelectric tensor components. For this work we are only interested in the polarization along the c-axis as all other components are negligible for our application as we will later see in Section 2.1.4. Using the material constants of AlN and Eq. (2.15), the strain induced polarization along the c-axis is given by [77] (using Voigt notation):

$$P_{p,3} = e_{33}S_3 + e_{31}(S_1 + S_2) . (2.18)$$

Because of the argument that the acoustic modes will be of longitudinal polarization,  $S_1$  and  $S_2$  are negligibly small compared to  $S_3$  (and  $|e_{31}| \le |e_{33}|$  [77]). Under this assumption we can simply write the strain induced polarization as the following:

$$P_{n,3} = e_{33}S_3 , (2.19)$$

which means a strain along the c-axis leads to a polarization along the c-axis. Eq. (2.19) is important as it will be used for the calculation of the electric field in Sections 2.2 and 2.3.1.

#### 2.1.3 Quantization of Acoustic Modes

In this section we will take a look into how acoustic modes can be quantized. This is important to understand how the coupling between the HBAR and the atoms works. The following theoretical description of the quantization of acoustic modes is based entirely on [46, 79]. For a detailed derivation

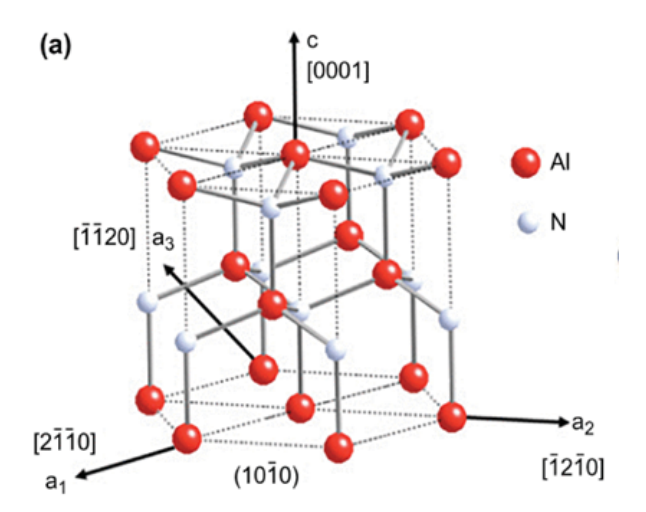


Figure 2.3: Images shows the crystal stucture of AlN. It can be decomposed into Al and N atoms organized in seperate hexagonal structures where they are displaced relative to each other along the c-axis. The displacement results in a different bond-length between Al and N along the c-axis compared to the other bonds. This causes a displacement of positive and negative charge centers leading to piezoelectric properties of the material. Figure taken from Ref [78].

and further discussion, see the original sources. For the quantization we do not have to know the exact spatial distribution of the acoust modes, this will become important later when calculating quantitative coupling strength between atoms and HBAR. Therefore, we assume the following general form for the displacement field of a mode *m* inside the resonator:

$$\vec{u}(\vec{r},t) = u(t)\vec{h}(\vec{r}) + \text{c.c.} = u_0 e^{-i\omega t} \vec{h}(\vec{r}) + \text{c.c.}$$
 (2.20)

where  $\vec{h}(\vec{r})$  is a normalized mode shape function:

$$\int_{V_{\text{HBAR}}} dV \, |\vec{h}(\vec{r})|^2 = 1 \tag{2.21}$$

The total system Hamiltonian is given by:

$$H = \int_{V_{\text{HBAR}}} dV \left( \frac{1}{2} \rho \frac{\partial u_i}{\partial t} \frac{\partial u_i^*}{\partial t} + \frac{1}{2} c_{ijlm} \frac{\partial u_i}{\partial x_j} \frac{\partial u_l}{\partial x_m} \right)$$
(2.22)

By using the ansatz (2.20) and the elastic wave equation (2.8), one can show that the Hamiltonian can be written as:

$$H = 2\rho\omega^2 |u_0(t)|^2 \tag{2.23}$$

By defining conjugate variables

$$p = -i\omega\rho(u_0(t) - \text{c.c.}), \quad q = (u_o(t) + \text{c.c.})$$
 (2.24)

we get the Hamiltonian of a harmonic oscillator:

$$H = \frac{p^2}{2\rho} + \frac{1}{2}\rho\omega^2 q^2 \tag{2.25}$$

With this we can now proceed with the quantization according to [80]. We define the creation and annihilation operators with the commutation relation  $[\hat{a}, \hat{a}^{\dagger}] = 1$ :

$$\hat{p} = -i\sqrt{\frac{\rho\hbar\omega}{2}}(\hat{a} - \hat{a}^{\dagger}), \quad \hat{q} = \sqrt{\frac{\hbar}{2\rho\omega}}(\hat{a} + \hat{a}^{\dagger})$$
 (2.26)

Plugging these definitions into the Hamiltonian (2.25) leads to the well known Hamiltonian of a quantum harmonic oscillator:

$$H = \hbar\omega \left(\hat{a}^{\dagger}\hat{a} + \frac{1}{2}\right) \tag{2.27}$$

Before we stop here we also need to express the displacement field in the quantized form as we will need this later to calculate the coupling strength between the HBAR and the atoms. By comparing (2.24) and (2.26), we can express u(t) in the quantized form:

$$\hat{u}(t) = \sqrt{\frac{\hbar}{2\rho\omega}}\hat{a}(t) \tag{2.28}$$

This gives us the quantized displacement field of a mode m inside the resonator:

$$\hat{u}(\vec{r},t) = \sqrt{\frac{\hbar}{2\rho\omega}}\hat{a}(t)\vec{h}(\vec{r}) + \text{H.c.}$$
(2.29)

Of course, there are infinity many modes inside the resonator. The Hamiltonian of the full system is then given by the sum over all modes. Here we will only consider one specific mode of the resonator that will later couple to the atoms.

#### 2.1.4 Acoustic Modes of an HBAR

The acoustic modes of an HBAR can be understood by analogy with an optical cavity. The sapphire substrate acts as the propagation medium, while the curved AlN dome provides an acoustic mirror. The thickness profile of the dome imprints a position-dependent phase on the reflected wave, resulting in transverse confinement through focusing of the wave after reflection [81].

By solving Eq. (2.10) for waves that propagate along the z-direction, one finds longitudinally polarized waves as a solution for sapphire (as well as for AlN). Here, the z-axis is aligned with the crystal c-axis. It means that the displacement field is aligned with the propagation direction along the crystal axis. We further assume that transverse k-components remain small (paraxial approximation) and the polarization can be taken as purely z-directed.

Under these assumptions, the confined acoustic mode can be described a longitudinal standing wave with a Gaussian transverse envelope [46] (here, we switched to cylindrical coordinates because of the rotational symmetry of the mode),

$$\vec{u}(z,r,t) = u_0 \,\hat{e}_z \cos\left(\frac{m\pi z}{L}\right) \exp\left(-\frac{r^2}{w^2}\right) \left(e^{-i\,\omega t} + e^{i\,\omega t}\right),\tag{2.30}$$

where m is the longitudinal mode number, L is the total thickness of the resonator (sapphire substrate plus AlN dome), and w is the mode waist determined by the dome curvature [46]. The standing-wave condition fixes

$$m = 1 + \frac{2(L - d)}{\lambda_{\text{Sap}}}$$
, (2.31)

where d is the thickness of the AlN layer and  $\lambda_{\rm Sap}$  is the acoustic wavelength in sapphire. This assumes that half an acoustic wavelength is located inside the dome. Because the longitudinal variation is much faster than the transverse one  $(\lambda_{\rm Sap} \ll w)$ , we approximate  $\partial u_z/\partial x \approx \partial u_z/\partial y \approx 0$ . The strain tensor (2.4) then reduces to a single dominant component,

$$S_3(z,r,t) = \frac{\partial u_z}{\partial z} = -\frac{m\pi}{L} u_0 \sin\left(\frac{m\pi z}{L}\right) \exp\left(-\frac{r^2}{w^2}\right) \left(e^{-i\omega t} + e^{i\omega t}\right). \tag{2.32}$$

Eq. (2.32) forms the basis for computing the piezoelectrically induced electric field in subsequent Sections. One has to note that the HBAR also hosts high order transverse modes [46]. However, we will mostly look at the fundamental Gaussian mode throughout this thesis. Numerically, the acoustic mode waist of a mode given a substrate thickness and dome curvature can be for example determined using the acoustic beam propagation method, described in Refs [46, 81, 82].

#### 2.1.5 Single-Phonon Acoustic Fields

The next step towards understanding the interaction between the HBAR and a Rydberg atom is to quantify the acoustic fields of a single phonon. So far, we discussed the quantization of the HBAR modes and their mode shapes. For the coupling strength, however, it is not enough to know the frequencies or shapes of the modes. We need the correctly normalized single-phonon displacement and strain fields to be able to calculate the results electric field of a single phonon.

In this subsection, we carry out this normalization and obtain explicit expressions for the single-phonon displacement and strain fields. These results provide the basis for the correct field normalization in the numerical simulations in Section 2.3. The following derivation is based on Ref [46] but with additional intermediate results (Eqs. (2.37) and (2.40)), that are of importance for us.

As we saw in the previous Section, the field inside the HBAR is longitudinally polarized. Therefore, the field is reduced to:

$$\vec{u}(\vec{r}) = u_0 e^{-i\omega t} h_z(\vec{r}) \cdot \hat{e}_z + \text{c.c.}$$
 (2.33)

We now have two quantities of interest: The amplitude  $u_0$  of the displacement field and the mode shape function  $h_z(\vec{r})$ . The amplitude is determined by the energy stored in the resonator. The mode shape function is determined by the geometry, the material constants and the boundary conditions of the resonator. To later calculate the coupling strength between the HBAR and the atoms, both quantities need to be known.

One can show that the energy inside the resonator is given by [46, 79]:

$$H = 2\rho\omega |u_0|^2 \,, \tag{2.34}$$

where  $\rho$  is the mass density of the substrate under the assumption that the piezo thickness is small compared to the substrate thickness. We can then set this expression equal to the energy of a single phonon and obtain the single-phonon amplitude of the displacement field:

$$u_0 = \sqrt{\frac{\hbar}{2\rho\omega}} \ . \tag{2.35}$$

This way we end up with the following expression for the single-phonon displacement field:

$$u_z(\vec{r},t) = \sqrt{\frac{\hbar}{2\rho\omega}} e^{-i\omega t} A H_z(\vec{r}) \cdot \hat{e}_z + \text{c.c.}, \qquad (2.36)$$

where  $H_z(\vec{r})$  is the unnormalized mode shape function. The product of A and  $H_z(\vec{r})$  is the normalized mode shape function  $h_z(\vec{r})$ . This separation is useful because from later numerical simulations we will get an unnormalized mode shape function. We therefore have to determine A according to:

$$A = \left( \int_{V_{\text{HBAP}}} dV |H_z(\vec{r})|^2 \right)^{-1/2} . \tag{2.37}$$

This expression can be calculated analytically if the displacement field is known analytically or numerically if the displacement field is obtained from numerical simulations.

As we will need this later in Section 2.3.1, the analytic form of the displacement field from Eq. (2.30) is used to explicitly calculate the normalized mode shape function. It is given by the following expression:

$$u_z(\vec{r},t) = u_0 A \cos\left(\frac{m\pi z}{L}\right) \exp\left\{\frac{-r^2}{w^2}\right\} \left[e^{-i\omega t} + e^{i\omega t}\right]. \tag{2.38}$$

With this, we can proceed to calculate *A*:

$$1 = A^2 \int_0^{2\pi} d\phi \int_0^{\infty} dr \, r \exp\left\{\frac{-2r^2}{w^2}\right\} \int_0^L dz \, \cos^2\left(\frac{m\pi z}{L}\right), \qquad (2.39)$$

which leads to:

$$A = \sqrt{\frac{4}{\pi L w^2}} \tag{2.40}$$

This gives us the final form of the single-phonon displacement field of a gaussian mode:

$$u_z(\vec{r},t) = \sqrt{\frac{\hbar}{2\rho\omega}} \sqrt{\frac{4}{\pi L w^2}} \cos\left(\frac{m\pi z}{L}\right) \exp\left\{-\frac{r^2}{w^2}\right\} \left[e^{-i\omega t} + e^{i\omega t}\right]. \tag{2.41}$$

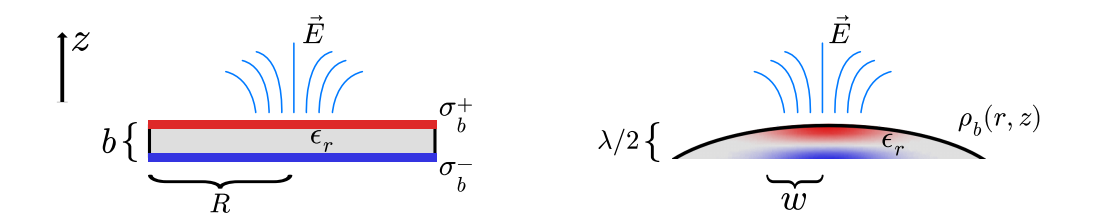


Figure 2.4: Left: Assuming a breathing mode of constant strain inside a cylindrical piezo disk of radius R and thickness b. Through the piezoelectric effect, bound surface charge densities  $\sigma_b^{\pm}$  are generated at the top and bottom of the disk which create an electric field above the disk. The disk is further characterized by its relative permittivity  $\epsilon_r$ . Right: Induced bound space charge density  $\rho_b(r,z)$  of a Gaussian mode inside an HBAR piezo dome. The piezo dome has a thickness of half an acoustic wavelenghts and is further characterized by its relative permittivity  $\epsilon_r$ . The mode is characterized by the acoustic mode waist w.

According to Eq. (2.32) the single phonon strain is then given by:

$$S_3(\vec{r},t) = \frac{\partial u_z}{\partial z} = -\sqrt{\frac{2\hbar\omega}{\pi c_{33}Lw^2}} \sin\left(\frac{m\pi z}{L}\right) \exp\left\{-\frac{r^2}{w^2}\right\} \left[e^{-i\omega t} + e^{i\omega t}\right], \qquad (2.42)$$

where  $c_{33}$  is the relevant elastic constant of the substrate.

## 2.2 Analytic Electric Field Model

Until now, we have looked into the acoustic properties of the HBAR, namely the quantization of the acoustic modes and their spatial profiles including that of single phonons. Furthermore, we discussed the piezoelectric properties of aluminum nitride (AlN) which is the piezoelectric material used in the HBAR. We now have all the necessary ingredients to understand how the HBAR generates an oscillating electric field that can couple to Rydberg atoms. Even though we will later calculate the electric field numerically, it is useful to start with a simplified analytic model. The goal is not just to get a first estimate, but to understand how the field depends on key parameters such as the resonance frequency. These scaling relations remain valid when numerically calculating the electric field of a Gaussian mode as shown in Fig. 2.4 on the right, as we will see later.

Following Ref. [56], we therefore first look at a simplified case: a piezoelectric disk of radius R and thickness b that undergoes a thickness mode oscillation, as shown in Fig. 2.4 (left). In this model the strain is assumed to be constant, which allows the electric field above the disk to be calculated directly from the induced surface charges. However, the results for the electric field strength from Ref. [56] were not matched by previous numerical simulations [62] that were about one order of magnitude off. We will therefore try to understand the reason for this discrepancy and calculate the electric field analytically which reproduces the numerical results.

#### 2.2.1 Quasistatic Approximation

For the GHz frequencies of interest, the electromagnetic wavelength in vacuum is on the order of centimeters (e.g.  $\lambda \sim 50 \,\mathrm{mm}$  at  $f = 5.8 \,\mathrm{GHz}$ ), while the atoms are located only tens of micrometers away from the HBAR surface. Since these distances are much smaller than the wavelength, retardation effects can be neglected and only the near-field contribution of the oscillating charges is relevant [83].

We can therefore calculate the electric field using electrostatics. In general, we will have oscillating bound charges inside the piezoelectric material due to the strain field of the acoustic wave of the following form:

$$\rho_b(\vec{r},t) = \rho_b(\vec{r}) \left( e^{-i\omega t} + e^{i\omega t} \right), \tag{2.43}$$

where  $\rho_b(\vec{r})$  is the static spatial distribution of charges determined by the strain field. Using the quasistatic approximation, the corresponding electrostatic field  $\vec{E}_0(\vec{r})$  is then obtained for  $\rho_b(\vec{r})$ . The time dependence of the electric field then follows that of the charges, leading to:

$$\vec{E}(\vec{r},t) = \vec{E}_0(\vec{r}) \left( e^{-i\omega t} + e^{i\omega t} \right). \tag{2.44}$$

This form will be used in the following sections to evaluate the electric field from the strain-induced bound charges and to determine the coupling to the atoms.

#### 2.2.2 The Total Polarization inside the Piezoelectric Resonator

The first step towards calculating the electric field generated by the HBAR is to understand the polarization inside the piezoelectric material. The polarization is important because it is the source of the electric field. For this we start from the constitutive Eq. (2.17):

$$D_i = e_{ij}S_j + \epsilon_{ij}^S E_j . (2.45)$$

We can decompose this equation in the following way:

$$D_i = \epsilon_0 E_i + e_{ij} S_j + \epsilon_0 \chi_{ij}^S E_j , \qquad (2.46)$$

where we used that  $\epsilon_{ij}^S = \epsilon_0(\delta_{ij} + \chi_{ij}^S)$  with  $\chi_{ij}^S$  being the electric susceptibility at constant strain. This we can compare to the known equation from electrostatics [83]:

$$D_i = \epsilon_0 E_i + P_i \,, \tag{2.47}$$

where  $P_i$  is the *i*-th component of the polarization vector. Comparing (2.46) and (2.47) we can identify the total polarization  $P_{tot}$  as:

$$P_{tot,i} = e_{ij}S_j + \epsilon_0 \chi_{ij}^S E_j = P_{S,i} + P_{D,i} . \tag{2.48}$$

The first part  $P_{S,i}$  is the polarization that is induced by the strain inside the piezoelectric material. This is the important part that only exisits inside a piezoelectric material, it shows that we can have a permanent polarization without having to apply an electric field externally. The second part  $P_{D,i}$  is the polarization that is induced by the electric field inside the piezoelectric material. This is the part that is present in all dielectric materials and is not specific to piezoelectric materials. However, it is important to understand

that  $P_{D,i}$  is still present in our case. Furthermore, it is important to realize that  $P_{D,i}$  weakens the electric field as the dielectric material will try to cancel the strain induced polarization. This is why we have to take it into account when calculating the electric field that is generated by the HBAR.

A question that arises is if we can in some ways calculate the total polarization  $P_{tot,i}$  analytically. This would allow us to access the electric field analytically. For this, we can use the fact that there are no free charges in the system (these are charges that are not the results of polarization). This means that the divergence of the displacement field is zero [83]:

$$\nabla \cdot \vec{D} = 0. \tag{2.49}$$

The second thing we know is that in vacuum, above the piezo disk, we have

$$D_i = \epsilon_0 E_i \,, \tag{2.50}$$

and we know that the normal component of  $\vec{D}$  is continuous as the piezo-vacuum boundary in case of no free surface charges (charges that are not the results of polarization) [83]. When neglecting edge effects at the disk, we can assume that the electric field is purely normal to the surface of the piezo disk which means that we only have a normal component of the displacement field  $D_{\perp}$ . Furthermore, we assume to not have contributing off-diagonal elements in the susceptibility tensor  $\chi_{ij}^S$  which means that we can write it as a scalar quantity  $\chi$ . Another assumption is that our acoustic mode is longitudinally polarized such that, according to Eq. (2.19), only a strain induced polarization along the z-axis exists. With these assumptions we can now write down the normal component of the displacement field at the piezo-vacuum interface:

$$D_{\perp}^{\text{vac}} = D_{\perp}^{\text{pz}} = \epsilon_0 E_{\perp}^{\text{vac}} \tag{2.51}$$

$$D_{\perp}^{\text{vac}} = D_{\perp}^{\text{pz}} = \epsilon_0 E_{\perp}^{\text{vac}}$$

$$\rightarrow \epsilon_0 \epsilon_r E_{\perp}^{\text{pz}} + P_{D_{\perp}}^{\text{pz}} = \epsilon_0 E_{\perp}^{\text{vac}} .$$
(2.51)

Here,  $D(E)_{\perp}^{\rm vac}$  and  $D(E)_{\perp}^{\rm pz}$  are the normal components of the displacement (electric) field in vacuum and the piezo, respectively, at the piezo-vacuum interface. Solving for the electric field  $E_{\perp}^{\rm pz}$  in the piezoelectric material gives us:

$$E_{\perp}^{\rm pz} = \frac{E_{\perp}^{\rm vac}}{1+\chi} - \frac{P_{S,\perp}}{\epsilon_0 (1+\chi)} \ .$$
 (2.53)

To now calculate the total polarization  $P_{tot\perp}^{pz}$  in the piezoelectric material, we can use the definition of the total polarization (2.48) and plug  $E_{\perp}^{pz}$  into it:

$$P_{tot\perp}^{\text{pz}} = \epsilon_0 \left( \frac{E_{\perp}^{\text{vac}}}{1+\chi} - \frac{P_{S,\perp}}{\epsilon_0 (1+\chi)} \right) + P_{S,\perp}$$
 (2.54)

$$= \frac{\epsilon_0 \chi}{1 + \chi} E_{\perp}^{\text{vac}} + \frac{P_{S,\perp}}{\epsilon_r} . \tag{2.55}$$

The electric field  $E_{\perp}^{\rm vac}$  above the piezoelectric material is not known. However, we can make the assumption that the electric field outside the piezoelectric material is small compared to the piezoelectric induced polarization  $P_{S,\perp}$  inside.

To understand why this is a good approximation, we can think of the piezo disk as a simple plate capacitor where the total polarization induces bound surface charges at the top and bottom of the disk. The electric field inside a capacitor is much larger than the electric field outside and one usually neglects the electric field outside [83]. This is the same situation we have here. Therefore, we can assume that the electric field outside is small compared to the piezoelectric induced polarization  $P_S$  and can be neglected. This means that we can set  $E_{\perp}^{\text{vac}} = 0$  in (2.55) and get:

$$P_{tot\perp}^{\rm pz} \approx \frac{P_{S,\perp}}{\epsilon_r} \ .$$
 (2.56)

This means that the total polarization in the piezoelectric material is given by the polarization induced by the strain divided by the relative permittivity of the piezoelectric material. This is a very important result as it shows that the total polarization is not only determined by the piezoelectric effect, but also by the relative permittivity of the piezoelectric material.

#### 2.2.3 The Electric Field above the Piezoelectric Resonator

The next step is now to determine the electric field above the pizeo as this is the quantity of interest to calculate the coupling strength between the HBAR and the atoms. From electrostatics we know that a polarization  $\vec{P}$  leads to a bound volume charge density  $\rho_b$  and a bound surface charge density  $\sigma_b$  [83]:

$$\rho_b = -\nabla \cdot \vec{P} \tag{2.57}$$

$$\sigma_h = -\hat{n} \cdot \vec{P} \ . \tag{2.58}$$

where  $\hat{n}$  is the normal vector to the surface.

Given a polarization  $\vec{P}$  we can now calculate thse quantities and use them for the field calculation. Analogous to the previous mentioned Ref [56], we will assume a constant strain inside the piezoelectric disk which results in a constant polarization along the z-axis. This strain we will call  $S_0$  where the index 0 indicates that this is the strain corresponding to a single phonon (this notation will be used from now on to indicate quantities that are normalized to a single phonon). From equation Eq. (2.19) and Eq. (2.56) we can derive the total polarization to be:

$$P_{tot} = \frac{e_{33}S_0}{\epsilon_r} \ . \tag{2.59}$$

As we assume the polarization to be constant and parallel to the surface normal vector  $\hat{n}$ , it directly follows that

$$\rho_b = 0 \tag{2.60}$$

$$\sigma_b^{d,u} = \pm \frac{e_{33} S_0}{\epsilon_r} , \qquad (2.61)$$

where  $\sigma_b^{d,u}$  stands for the bound surface charge density at the bottom (d) and the upper (u) surface of the piezoelectric disk. With this result we can directly calculate the electric field that a charged disk generates above itself using Coulombs law. From the rotational symmetry of the problem we know that along the z-axis above the center of the disk, the electric field will only have a z-component. It can be

calculated in the following way:

$$E^{d,u}(z) = \frac{1}{4\pi\epsilon_0} \int_0^{2\pi} d\phi \int_0^R dr \, r\sigma_b^{d,u} \frac{z}{(z^2 + r^2)^{3/2}} = \frac{\sigma_b^{d,u}}{2\epsilon_0} \left( 1 - \frac{z}{\sqrt{R^2 + z^2}} \right) , \qquad (2.62)$$

where R is the radius of the piezoelectric disk and z is the distance above the disk. The total electric field above the disk will then be given by the following equation where the surface charge densities are already plugged in:

$$E(z) = E^{u}(z) + E^{d}(z+b) = -\frac{e_{33}S_0}{2\epsilon_0\epsilon_r} \left( \frac{z}{\sqrt{R^2 + z^2}} - \frac{z+b}{\sqrt{R^2 + (z+b)^2}} \right). \tag{2.63}$$

Here, b is the thickness of the piezoelectric disk. Since our disk has the thickness of half an acoustic wavelength, so on the order of 1  $\mu$ m, we can assume that the distance b is small compared to the distance z above the disk (the atoms will be trapped around 50  $\mu$ m away). We can therefore expand Eq. (2.63) around b/z = 0 and get:

$$E(z) \approx \frac{e_{33}S_0}{2\epsilon_0\epsilon_r} \frac{R^2b}{\sqrt{R^2 + z^2}} + O\left(b^2\right) . \tag{2.64}$$

This equation allows us to consider two interesting limits.

- 1. If the radius of the piezoelectric disk is much larger than the distance z between disk and atom, we can neglect the  $z^2$  term in the denominator and therefore expect to have a weak electric field above the disk that does not change with the distance z.
- 2. If the radius of the piezoelectric disk is small compared to the distance z between disk and atom, we can neglect the  $R^2$  term in the denominator and get a dipole-like electric field with a  $1/z^3$  dependence. This is the case that the disk can be approximated as a dipole.

To explicitly evaluate the electric field above the piezo, the single phonon strain  $S_0$  needs to expressed explicitly. For a uniform strain in the disk, this can be expressed through the zero point fluctuation of the displacement field [56] and the piezo disk thickness b which results in:

$$S_0 = \sqrt{\frac{4\hbar}{\rho \pi R^2 \omega b^2}} \,, \tag{2.65}$$

where  $\rho$  is the density of the material and  $\omega$  is the angular frequency of the acoustic mode. Inserting this into Eq. (2.64) and setting  $\epsilon_r$  to one reproduces the results for the electric field strength from Ref [56] ( $E_z(z=5\,\mu\text{m})\approx 1.7\,\text{V m}^{-1}$  using same material and geometry parameters). However, as explained before, this overestimates the electric field strength as it does not take the dielectric response of the piezoelectric material into account. Taking this into account by setting  $\epsilon_r=9$  reproduces the result for the field strength expected from numerical simulations which is about one order of magnitude smaller [62].

The next thing to realize in Eq. (2.64) is that the optimal choice of the disk radius (or later the acoustic mode waist) depends on the distance we want to have between the disk and the atoms. Furthermore, it determines the homogeneity of the electric field at the atom position. A larger disk radius (or larger

mode waist) leads to a more homogeneous electric field at the atom position at the cost of an overall weaker electric field. This optimal choice of piezo disk radius can be calculated. For this we can use Eq. (2.64) from above to calculate

$$\frac{\partial E(z)}{\partial R} \stackrel{!}{=} 0 , \qquad (2.66)$$

which results in the following:

$$R^{E\max}(z) = \frac{z}{\sqrt{2}} \ . \tag{2.67}$$

This means that the disk radius that maximizes the electric field at a given distance z scales linearly with z.

In summary, the analytic model show that the relevant material figure of merit is the ratio  $e_{33}/\epsilon_r$ , rather than  $e_{33}$  alone as assumed in Ref. [56]. This follows from the derivation that the total polarization is given by  $P_{\text{tot}} \approx P_S/\epsilon_r$ , which shows that the dielectric response of the piezoelectric material reduces the effective polarization. Eq. (2.64) allows us to calculate explicit electric field strengths. Moreover, the results shows a linear dependence: The disk radius that maximizes the electric field at a given atom–surface distance scales linearly with that distance.

Beyond these results, we can use the model to derive important scaling laws of the electric field in dependence of system parameters like the resonance frequency. Furthermore, we can qualitatively predict the effect of a dielectric substrate. Both points will be addressed in the next Section.

#### 2.2.4 Scaling Laws of the Electric Field Strength and Effects of Dielectric Substrate

In the following, Eq. (2.64) will be the basis to look at the electric field dependence on resonance frequency and substrate thickness.

#### Scaling of Electric Field Strength with Resonance Frequency

In the HBAR, the resonance frequency determines the thickness of the piezoelectric dome. The dome thickness is always chossen to be half an acoustic wavelength. In case of the simple disk model, this means that the thickness b is given as

$$b = \frac{\lambda^{\text{AIN}}}{2} \propto \frac{1}{\omega}, \qquad (2.68)$$

where  $\omega$  is the mode frequency. A higher frequency reduces the thickness of the dome. According to Eq. (2.64), the electric field above the resonator fulfills the following proportionality to first order:

$$E_z(z) \propto b \cdot S_0 \,, \tag{2.69}$$

where  $S_0$  is the single phonon strain amplitude. For the Gaussian mode, we calculated this in Eq. (2.42). The amplitude scales with  $\sqrt{\omega}$ . Plugging Eqs. (2.42) and (2.68) into Eq. (2.69) leads to

$$E_z(z) \propto b \cdot S_0 \propto \frac{\sqrt{\omega}}{\omega} = \frac{1}{\sqrt{\omega}}$$
 (2.70)

As a result, the electric field decreases with increasing frequency according to Eq. (2.70). This can be understood intuitively. The strain amplitude increases for larger frequencies. However, the electric field

decreases lineary when the dome thickness decreases as the two charge densities of opposite polarity come closer together and cancel each other out stronger.

#### Scaling of Eletric Field Strength with Substrate Thickness

According to Eq. (2.64), the electric field is directly proportional to the single phonon strain amplitude  $S_0$ . From Eq. (2.42), it directly follows that

$$E_z(z) \propto \frac{1}{\sqrt{L}}$$
, (2.71)

where L is the total thickness of the resonator. Under the assumption that the dome thickness is small compared to the substrate thickness  $L_{\rm sub}$ , it follows that

$$E_z(z) \propto \frac{1}{\sqrt{L_{\text{sub}}}}$$
 (2.72)

#### **Effect of Dieletric Substrate**

To understand the effect of the dielectric repsonse it is useful to stick to the picture of a charged plate capacitor where the charges stem from the strain induced polarization. As shown before, we expect a non-zero electric field outside the capacitor in case of finite plate radii. If we now place a dielectric material directly below the lower capacitor plate, the field will induce a polarization inside the substrate which means new bound charges will appear at the substrate-piezo interface. As the polarization tries to cancle the electric field from the capacitor, these bound charges will be of opposite sign compared to the bound charges at the lower capacitor plate. In total this means that there will now be an imbalance in the charge densities of lower and upper capacitor plate. When looking at Eq. (2.63) with charge densities  $|\sigma_b^u| \ge |\sigma_b^d|$  one immediately noctices that this will lead to an enhanced field in vacuum above the piezo. Effectivelly, the dielectric substrate pushes the electric field lines out of the substrate and into the vacuum. This means that a dielectric substrate will lead to an enhanced electric field above the piezo compared to a non-dielectric substrate, an effect that will enhance the coupling to the atoms.

Two relevant aspects are not captured yet. First, the strain inside the piezo disk is not uniform but follows a Gaussian mode shape, as we saw in Section 2.1.4, which will modify the charge distribution and the resulting field above the device. Second, the effect of the dielectric property is only qualitatively understood. Both points will be addressed with the numerical simulation in the next Section.

#### 2.3 Numerical Simulations

In the previous section, we understood how the piezoelectric effect generates an oscillating electric field above the HBAR by a strain induced bound charge density where a simple constant strain breathing mode was assumed. Furthermore, we have discussed quantitatively the effect of the dielectric substrate and dervived scaling laws, e.g. for the scaling with the mode frequency. In this section, the electric field will be simulated for a real Gaussian acoustic mode of an HBAR. For these simulations we will use the finite element method (FEM) to solve the problem. We will first look into a static simulation where we will solve the electrostatic problem for a given bound charge density which will allow us to simulate the electric field above the HBAR in dependence of important design parameters as e.g. the acoustic mode

waist and the resonance frequency. The results will later be used to calculate the coupling strength to the atoms. In a second step, we will look into an eigenfrequency simulation where we will solve the coupled mechanical and electrical problem to obtain the acoustic mode shapes, frequencies and the electric field of the HBAR. This will allow us to validate the results from the electrostatics simulation and to use it in more complex simulation setups in the future.

#### 2.3.1 FEM Electrostatic Simulation: Setup

The problem is solved using the electrostatics module in COMSOL Multiphysics, a FEM simulation software [84]. The simulation procedure, physical assumptions and results are described in detail below.

#### **Geometry and Materials**

The geometry used in the electrostatic FEM simulations is shown in Fig. 2.5. It consists of three cylindrical domains: a large cylinder representing the sapphire substrate, a thin disk on top representing the piezoelectric AlN layer, and a finite cylindrical vacuum region around the resonator. In addition, a ground plane below the HBAR can be included to represent the atom chip ground plane.

The piezoelectric layer is modeled as a flat disk. In the actual device the layer has a slight dome curvature, but the radius of curvature ( $\sim 10\,\mathrm{mm}$ ) is much larger than the distance between piezo and the atoms ( $\sim 50\,\mathrm{\mu m}$ ). Therefore, this curvature has a negligible influence on the electric field distribution, which is determined by the strain induced polarization. The curvature is only important for the confinement of the acoustic modes. This will be validated in Section 2.3.4.

The material domains are represented by their dielectric properties. The vacuum region is modeled with relative permittivity  $\epsilon_r = 1$ . The AlN layer is assigned a relative permittivity of  $\epsilon_r^{\text{AlN}} = 9$ . The sapphire substrate is modeled either with its actual dielectric constant  $\epsilon_r^{\text{Sap}} = 11.6$  or artificially set to  $\epsilon_r^{\text{Sap}} = 1$ , in order to compare the case of a dielectric and a non-dielectric substrate. Mechanical material parameters are not required in this study. Instead, the source of the electric field is a fixed space charge density inside the AlN disk, which represents the bound charges that arise from the strain-induced polarization. The explicit form of this distribution and its implementation are described in the next subsection. The explicit dimensions of all domains are listed in Table 2.1.

#### **Physics Module Setup**

For this simulation, only COMSOL's *Electrostatics* interface is required. From Eq. (2.48) we know that the total polarization inside a piezoelectric material can be decomposed into a strain-induced part and a dielectric response part. If we can compute the strain-induced polarization, the induced bound charge densities can be derived from it. The dielectric response can then be included in the simulation via the material permittivities. This way, no mechanical properties are needed in the simulation.

To use this method, we start with Eq. (2.32) where we wrote down the strain component  $S_3$  of a fundamental Gaussian mode which we expect to have in our resonator. From Eq. (2.57) and Eq. (2.58) we can derive the corresponding bound charge densities that are induced by the strain via the piezoelectric

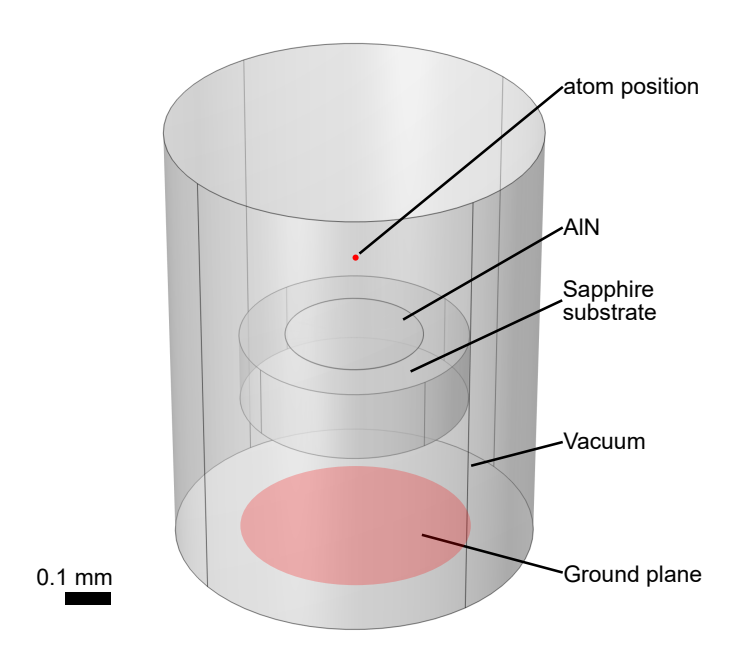


Figure 2.5: Geometry of FEM electrostatics simulation. The piezo disk (AlN) and substrate (sapphire) are modeled as cylinders, with a vacuum cylinder surrounding the entire structure. Explicit dimensions are listed in Table 2.1. The atom position is sketched qualitatively. The red circle below the substrate represents the chip ground plane.

Table 2.1: Geometry dimensions used in the electrostatics FEM simulations of the HBAR system. The piezo disk and substrate are modeled as cylinders, with a large vacuum cylinder surrounding the entire structure and a vacuum region of interest (ROI) above the piezo. The vacuum ROI is just the region where the electric field will be evaluated and has therefore a finer mesh.

Parameter	Description	Value / μm
$h_{\rm piezo}$	Piezo disk thickness	0.93
$R_{\rm piezo}$	Piezo disk radius	150
$L_{ m sub}^{ m r}$	Substrate thickness	160
$R_{ m sub}$	Substrate radius	250
$h_{\mathrm{vac,ROI}}$	Vacuum ROI cylinder height	280
$R_{\rm vac,ROI}$	Vacuum ROI cylinder radius	150
$h_{ m vac,large}$	Large vacuum cylinder height	1 000
$R_{\rm vac,large}$	Large vacuum cylinder radius	400

effect. In follows that

$$\sigma_b = 0 \tag{2.73}$$

$$\sigma_b = 0 \qquad (2.73)$$

$$\rho_b(r, z, t) = -e_{33} \frac{\partial S_3}{\partial z} = \rho_0 \exp\left(-\frac{r^2}{w^2}\right) \cos\left(\frac{\pi z}{b}\right) \left(e^{-i\omega t} + e^{i\omega t}\right) , \qquad (2.74)$$

where  $\rho_b(r,z,t)$  is the bound volume charge density inside the piezoelectric layer,  $\sigma_b$  is the bound

surface charge density at the top and bottom surfaces of the piezoelectric layer,  $\rho_0$  is the amplitude of the charge density and b is the thickness of the piezo layer. As discussed in Section 2.2.1, we can ommit the time dependence and just calculate the static electric field distribution because the atoms are located in the near field. This gives us the following expression for the static charge density distribution:

$$\rho_b(r,z) = 2\rho_0 \exp\left(-\frac{r^2}{w^2}\right) \cos\left(\frac{\pi z}{b}\right) . \tag{2.75}$$

In principle, this is already sufficient to use as an input for the simulation, however, we are intersted in the electric field that a single phonon generates. Therefore, we have to determine the amplitude  $\rho_0$  that corresponds to a single phonon in the resonator. For this, we use Eq. (2.42) where we calculated the single phonon strain field. From this it directly follows that the amplitude of the charge density is given by:

$$\rho_0 = -e_{33} \frac{S_0 \pi}{b} = \sqrt{\frac{2\hbar \omega \pi e_{33}^2}{c_{33} L w^2 b^2}} \,. \tag{2.76}$$

Since the piezo layer thickness is small compared to the thickness of the substrate, we use the stiffness constant of the substrate for  $c_{33}$  as this determines the strain amplitude. Eq. (2.76) can now be implemented into the simulation using an analytic function in the *Definitions* node. To actually set the strain induced charge density, a fixed *Space Charge Density* is set in the electrostatics node where the analytic function is used as the input. The dielectric response requires no further considerations as it is already included via the material permittivities.

#### **Meshing Procedure and Study Configuration**

Having established the electrostatic model, we proceed with the meshing and study configuration in COMSOL. In a FEM simulation, meshing refers to the discretization of the simulation volume into small, discretized volume elements on wich the associated differential equations are solved. Depending on the problem, the results can be very sensitive to the exact mesh choice [79].

Fig. 2.6 shows the full meshed geometry. The vacuum cylinder sorounding everything is meshed using a *Free Tetrahedral* of *Normal* size to reduce mesh complexity. The HBAR substrate, piezo layer and vacuum ROI cylinder are meshed using a combination of *Free Triangular* mesh and *Swept* mesh. A free triangular mesh of *Extra Fine* size is applied to the vacuum cylinder top surface and swept along the *z*-direction until the substrate piezo interface. A finer swept mesh is used in the piezo layer with 8 elements along the *z*-direction because it is cruicial to fully resolve the three-dimensional charge density distribution in this region. A second free triangular mesh is applied to the top substrate surface and swept down to along the bottom substrate to the bottom vacuum cylinder surface.

All studies are stationary studies with default settings. The substrate is set to vacuum or dielectric properties to check the influence of the dielectric response. Furthermore, from Section 2.2.3 we expect to have an optimal acoustic mode waist for each atom resonator distance. For this reason, the studies are performed for different acoustic mode waists w using a parametric sweep. In addition, the substrate thickness is varied to check the influence of the substrate on the electric field strength and the frequency of the mode is varied to check the dependence on it. The convergence of the results was checked by decreasing the mesh size until convergence of the result (the electric field) was observed.

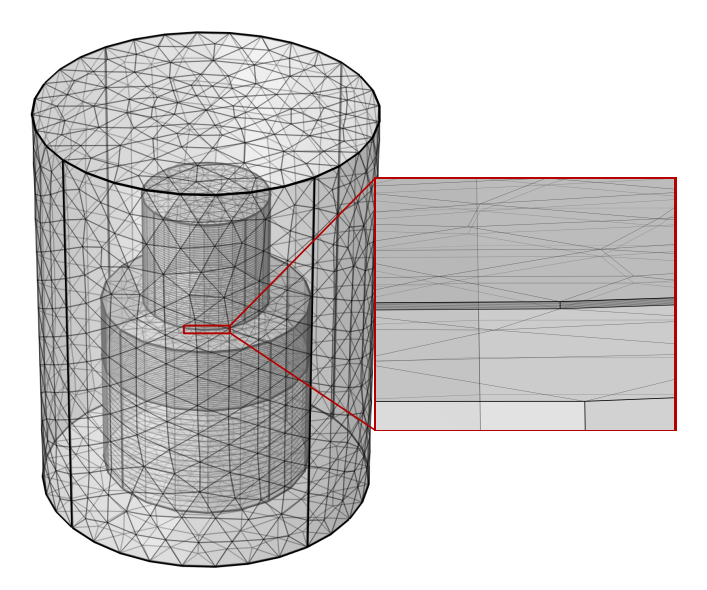


Figure 2.6: Meshed geometry of the electrostatics simulation. The right inset shows a zoom into the piezo layer with a higher number of vertical mesh nodes compared to the rest to fully resolve the charge density distribution. For dimensions check Fig. 2.5 and Table 2.1.

#### 2.3.2 FEM Electrostatic Simulation: Results

The following section presents the results from the simulation and its relevance for coupling the HBAR to Rydberg atoms. The coupling strength between the resonator and the atoms is ultimately set by the electric field amplitude at the atomic position. Understanding the field distribution above the resonator is therefore essential for estimating the achievable coupling strengths and for identifying optimal device parameters.

Several aspects are important. The dependence of the electric field strength on the atom–resonator distance directly determines how strongly atoms interact with the resonator at a given separation. The field also depends on the acoustic mode waist (see Eq. (2.67)), which sets the optimal waist for a particular atom–resonator distance and indicates how sensitive the coupling is to the exact atom position. This determines how many atoms at different positions can simultaneously couple well to the resonator. Furthermore, substrate thickness and dielectric properties influence both the distribution and the amplitude of the field and are therefore important factors in understanding the overall atom–resonator interaction. Finally, the frequency dependence of the field is relevant for understanding how the coupling strength changes when tuning the resonator frequency to different atomic transitions.

The simulation was performed for different acoustic mode waists between  $10 \,\mu\text{m}$  -  $40 \,\mu\text{m}$  and with a substrate thickness of  $160 \,\mu\text{m}$ . Fig. 2.7(a) shows the electric field above the piezo for a mode waist of  $w = 32 \,\mu\text{m}$ . The field is strongest directly above the center of the piezo and decreases with increasing distance. The streamlines in the plot represent the orientation of the electric field showing a behaviour typical to an electric dipole. As expected from Section 2.2.4, the dielectric substrate pushes the electric field out of the substrate and into the vacuum causing an asymmetry which enhance the field at the position of the atoms.

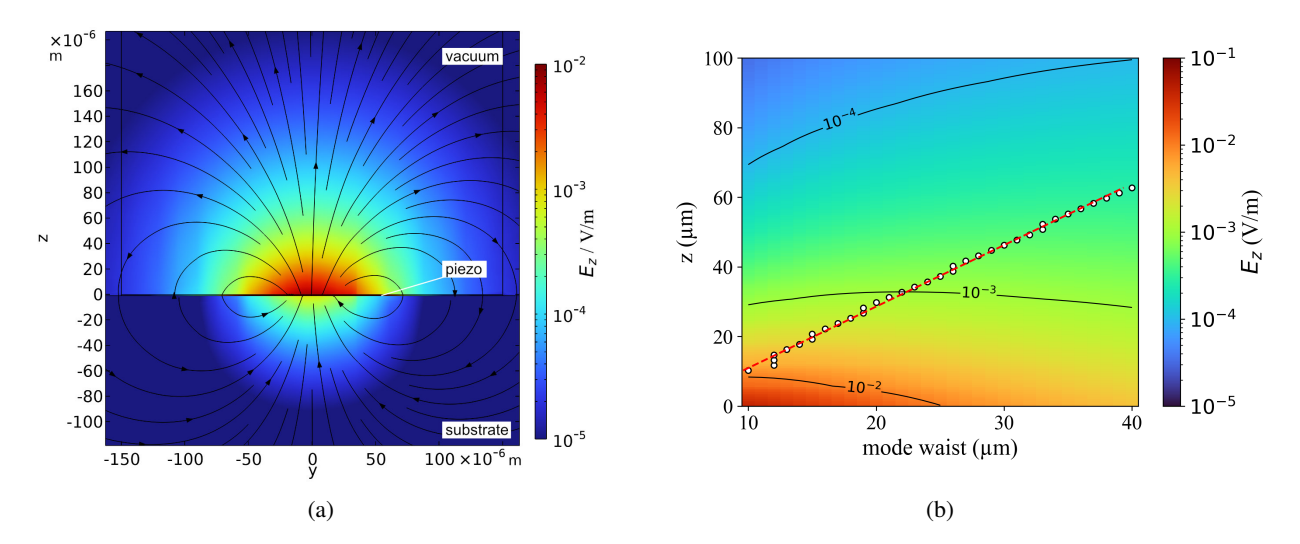


Figure 2.7: (a) shows the electric field above and inside the resonator in the yz-plane for x=0. The absolute electric field amplitude is color coded and the streamlines represent the direction of the electric field. The simulation was performed for a mode waist of  $w=32\,\mu\mathrm{m}$  and a substrate thickness of  $L_{\mathrm{sub}}=160\,\mu\mathrm{m}$ . (b) shows the electric field amplitude above the center of the piezo in dependence of distance to the disk and acoustic mode waist. The scattered points are the points of maximum electric field given a fixed atom-resonator distance. The dashed line is a linear fit to these points.

#### Dependence of the electric field on atom-resonator distance and acoustic mode waist

As mentioned above, the shape depends on the acoustic mode waist. Fig. 2.7(b) shows the amplitude of the electric field  $E_z$  above the center of the piezo in dependence of distance to the disk and the mode waist. As expected from Eq. (2.64), the dependence of the field amplitude on the distance is much stronger for smaller acoustic mode waists than for larger ones. This is because the smaller the mode waist is the faster the field lines push outwards to the left and right and therefore the field above the piezo decreases faster. However, because they are more concentrated close to the surface, the field is larger in amplitude at close distances. The scattered points in Fig. 2.7(b) are the points of maximum electric field given a fixed atom-resonator distance. One can see a linear relation between the acoustic mode waist and the distance. This agrees with the expectation from the analytic model from Eq. (2.67). A linear fit to the data gives the following results:

$$w^{E_{\text{max}}}(z) = 0.57 \cdot z + 3.79 \,\mu\text{m} \,, \tag{2.77}$$

where  $w^{E\max}(z)$  is the optimal mode waist for a given atom-resonator distance z. For comparison, the analytic result (neglecting the Gaussian mode shape completely) Eq. (2.67) gives a proportionality factor of  $\approx 0.7$ . As a rule of thumb we can conclude that the optimal acoustic mode waist for a given atom-resonator distance is roughly half the distance. However, it becomes clear that the exact choice of the mode waist becomes less cruical the further away we are. The spatial variation in electric field amplitude is smaller for larger mode waists as shown in Fig. 2.7(b).

For a better visualization of Fig. 2.7(b) we can take a look at Fig. 2.8. It shows the maximally achievable electric field above the piezo for different atom-resonator distances when choosing the optimal acoustic mode waist according to Eq. (2.77) (shown in orange). The electric field in dependence of

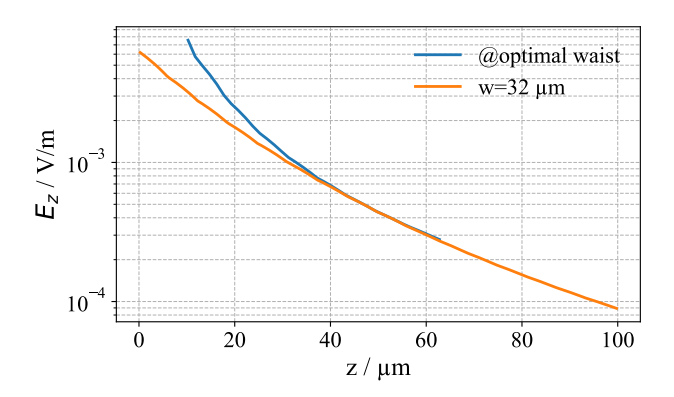


Figure 2.8: Electric field amplitude above the piezo in dependence of atom-resonator distance for a substrate thickness of  $L_{\rm sub} = 160 \, \mu \rm m$ . The orange line shows the maximally achievable electric field when choosing the optimal acoustic mode waist according to Eq. (2.77). The blue line shows the electric field for a fixed mode waist of  $w = 32 \, \mu \rm m$  which is optimal for an atom-resonator distance of 50  $\mu \rm m$ . The small deviation from the -1/2 scaling law for the non-dielectric case is caused by the fact that the piezo layer is not included in the substrate thickness.

the distance for a fixed mode waist of  $w=32\,\mu\text{m}$ , which is optimal for an atom-resonator distance of 50  $\mu\text{m}$ , is shown in blue. One can see that for distances larger than  $\sim 30\,\mu\text{m}$  there is no significant gain in changing this acoustic mode waist.

#### Dependence of the electric field on substrate thickness and dielectric properties

The next interesting thing to look at is the dependence of the electric field on the substrate thickness and its dielectric properties. For this, a fixed mode waist of  $w=32\,\mu\mathrm{m}$  is chosen and the substrate thickness  $L_{\mathrm{sub}}$  is varied between  $1\,\mu\mathrm{m}$  and  $400\,\mu\mathrm{m}$  for the the case of a dielectric substrate and a non-dielectric substrate. Fig. 2.9 shows the resulting electric field at a fixed distance of  $50\,\mu\mathrm{m}$  above the piezo. One can see that for  $L_{\mathrm{sub}} \gtrsim 20\,\mu\mathrm{m}$  the electric field amplitude scales as

$$E_z \propto \frac{1}{\sqrt{L_{\text{sub}}}}$$
, (2.78)

which was expected from Eq. (2.72). Furthermore, the electric field is significantly enhanced for the case of a dielectric substrate compared to a non-dielectric substrate by almost a factor of two. This is again expected from the qualitative discussion in Section 2.2.4. For  $L_{\rm sub} < 20\,\mu \rm m$ , the electric field starts to deviate from the scaling law in Eq. (2.78) and approaches the solution for a non-dielectric substrate for very thin substrates ( $L_{\rm sub} \sim 1\,\mu \rm m$ ). This can be explained by the fact that for very thin substrates, the layer can not screen the electric field as effectively as a bulk substrate can, leading to a behavior that is more similar to the non-dielectric case. However, the resonators we are intersted in have substrate thicknesses of > 100  $\mu \rm m$ , which means Eq. (2.78) is valid.

#### Dependence of the electric field on resonance frequency

The simulation was performed for a fixed resonance frequency of  $f_m = 5.8 \,\text{GHz}$ , but we would like to know the scaling of the electric field amplitude with frequency. In the simulation, the resonance frequency

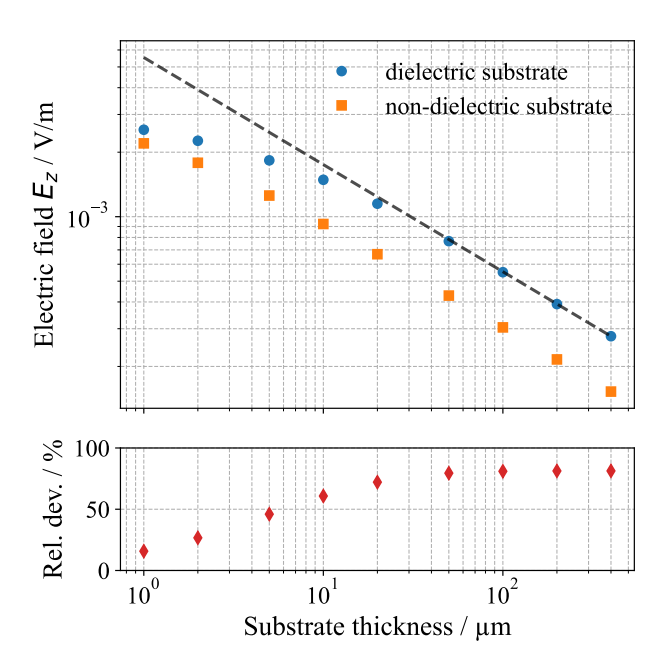


Figure 2.9: Electric field amplitude above the piezo in dependence of substrate thickness for a fixed atom-resonator distance of 50 µm and a fixed acoustic mode waist of w = 32 µm. The blue points are simulation results and show the case of a dielectric substrate ( $\epsilon_r^{\text{Sap}} = 11.6$ ) and the orange points show the case of a non-dielectric substrate ( $\epsilon_r^{\text{Sap}} = 1$ ). The dashed line is of slope -1/2 which represent the expectation from Eq. (2.78).

enters in the single phonon strain amplitude in Eq. (2.42) and in the thickness of the piezoelectric layer, which is half an acoustic wavelength  $\lambda^{AIN}$ . In Section 2.2.4, we derived Eq. (2.70) that predicts a scaling of

$$E_z \propto \frac{1}{\sqrt{f_m}}$$
 (2.79)

To verify this, the electric field was simulated for different resonance frequencies between 2 GHz and 12 GHz. Fig. 2.10 shows the resulting electric field at a distance of 50 µm above the piezo. One can see that the simulated field follows the expected scaling law from Eq. (2.79).

#### Combining the results

With the knowledge of the scaling laws for the electric field in dependence of substrate thickness and resonance frequency, we can now express the electric field at a given position z above the piezo for arbitrary substrate thicknesses, resonance frequencies and acoustic mode waists as:

$$E_z(z, L_{\text{sub}}, e_{33}, w, f_m) = E_z^{\text{sim}}(z, w) \sqrt{\frac{160 \,\mu\text{m}}{L_{\text{sub}}}} \sqrt{\frac{5.8 \,\text{GHz}}{f_m}} \frac{e_{33}}{1.55 \,\text{C} \,\text{m}^{-2}} \,, \tag{2.80}$$

where  $e_{33}$  is the piezo constant,  $L_{\rm sub}$  is the substrate thickness,  $f_m$  is the mode frequency, w is the acoustic mode waist and  $E_z^{\rm sim}(z,w)$  is the electric field for a substrate thickness of 160 µm, a piezo constant of  $e_{33}=1.55\,{\rm C\,m}^{-2}$  and a mode frequency of 5.8 GHz. The piezo constant is included here to

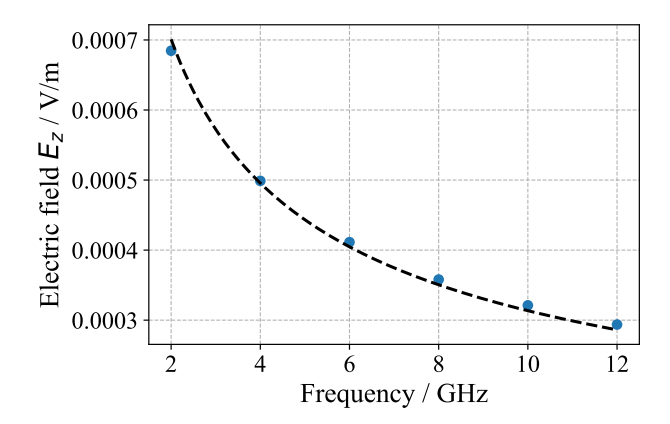


Figure 2.10: Electric field amplitude above the piezo in dependence of resonance frequency for a fixed atomresonator distance of 50 µm, a fixed acoustic mode waist of w=32 µm and a substrate thickness of  $L_{\rm sub}=160$  µm. The blue points are simulation results and the dashed line follows a function of the form  $E_z(f_m)=A\cdot f_m^{-1/2}$  which represent the expectation from Eq. (2.79) where the amplitude A is a fit parameter.

be able to scale the results in dependence of this material constants as there are significant differences in literatures where values range from  $e_{33} = 1.46$  [85] to  $e_{33} = 2.25$  [46]. A linear scaling is expected from Eq. (2.76). Another thing to note is that the existence of a ground plane mimicking the atom chip had no influence on the electric field of the HBAR and was therefore not included in any further discussions.

In summary, the electrostatic FEM simulations give us a qualitative understanding of the shape and scaling of the electric field above the HBAR. The dependence on acoustic mode waist, frequency, substrate thickness, dielectric properties, and piezoelectric material constants is now understood. Based on Eq. (2.80), the electric field at a given position z can be calculated for arbitrary system parameters. Furthermore, the simulated field shape for a given mode waist can be used to assess the spatial homogeneity of the field at the position of the atoms, which might be of interest in the future.

An important advantage of this method is that it decouples the acoustic mode simulation from the electric field simulation, which enables efficient parametric sweeps over acoustic mode waists and substrate thicknesses (and other parameters). Such studies would be more time-consuming in a fully coupled simulation. For example, the mode waist sweep between  $10\,\mu m$  and  $40\,\mu m$  with a substrate thickness of  $160\,\mu m$  can be completed in about 5 minutes on a PC with  $16\,GB$  RAM, while a coupled simulation of the same system evaluates only a single waist and a thin substrate of  $30\,\mu m$  but requires on the order of 2 hours.

The next section will compare these results to a full COMSOL eigenfrequency simulation of the coupled system, where both the acoustic and piezoelectric dynamics are included. Such a coupled simulation is valuable to verify the validity of the electrostatic method. However, since the results show good agreement (which we will see in the next Section), the electrostatic approach provides a significant speed advantage for parametric sweeps.

#### 2.3.3 FEM Eigenfrequency Simulation: Setup

In Section 2.2 we introduced a simplified analytic model of the HBAR, where the piezoelectric disk was assumed to undergo a uniform breathing mode and the substrate was treated as non-dielectric. This

Table 2.2: Geometry dimensions used in the eigenfrequency FEM simulations of the HBAR system. The substrate is modeled as half-cylinders with a dome-shaped piezo layer on top, surrounded by a vacuum half-sphere and a vacuum region of interest (ROI) above the dome.

Parameter	Description	Value / μm
	Description	value / µm
$h_{ m AlN}$	Piezo dome thickness	0.94
$R_{\rm dome, curv}$	Piezo dome radius of curvature	10 000
$h_{\mathrm{Sap}}$	Substrate thickness	28
$R_{\mathrm{Sap}}$	Substrate radius	250
$R_{\text{vac,sphere}}$	Vacuum sphere radius	300
$R_{\rm vac,ROI}$	Vacuum ROI cylinder radius	50
$h_{\mathrm{vac,ROI}}$	Vacuum ROI cylinder height	100

allowed us to estimate the oscillating electric field and gain intuition for the relevant physics but neglected realistic mode profiles and substrate effects. In Section 2.1.4 we identified that the relevant acoustic mode has a Gaussian profile, and in Section 2.2.4 we showed that the dielectric substrate modifies the field beyond a simple rescaling of the single-phonon displacement amplitude. These effects motivated the electrostatic simulations in Section 2.3.1, where the Gaussian mode shape and substrate permittivity were taken into account.

A further approximation made so far was to treat the acoustic problem independently of piezoelectricity, i.e. to determine mode shapes and frequencies solely from linear elasticity and then calculate the electric field in a separate step. In the following we relax this assumption by directly simulating the fully coupled piezoelectric system. This will allow us to quantitatively validate the electrostatic simulation results.

#### **Geometry and Materials**

The geometry of the simulation is shown in Fig. 2.11. It consists of the sapphire substrate (half cylinder of largest radius), the piezo dome (thin layer on top of the substrate), and a half sphere of vacuum surrounding the HBAR. One can see that both the piezo dome and the substrate are divided into half cylinders of different radii, which is solely for meshing purposes. The meshing will be discussed in more detail later. Furthermore, the half sphere of vacuum is also divided into the half sphere and a half cylinder above the piezo dome. This is also motivated by the meshing, as we want to have a higher mesh resolution in the region of interest above the piezo dome. Fig. 2.11 also shows a zoomed-in front view of the *yz*-plane. Here one can see the piezo dome which appears flat from further away because of the large radius of curvature compared to the thickness. Explicit dimensions of the geometry are provided in Table 2.2

The simulation volume is composed of three different materials. For the sphere around the HBAR we use *Perfect Vacuum* with a density of zero and a relative permittivity of one. The HBAR substrate and the AlN piezo dome are both user-defined anisotropic materials. For both sapphire and AlN, relative permittivity, the full stiffness tensor  $c_{ij}$ , and (for AlN) the piezoelectric tensor  $e_{ij}$  are specified in Voigt notation, as listed in Table 2.3. In particular, the constant  $c_{33}$  enters the simple velocity estimate used below. The z-axis of the global coordinate system is aligned with the crystallographic c-axis of both materials, so that the longitudinal acoustic propagation we simulate corresponds directly to the experimentally relevant c-axis orientation.

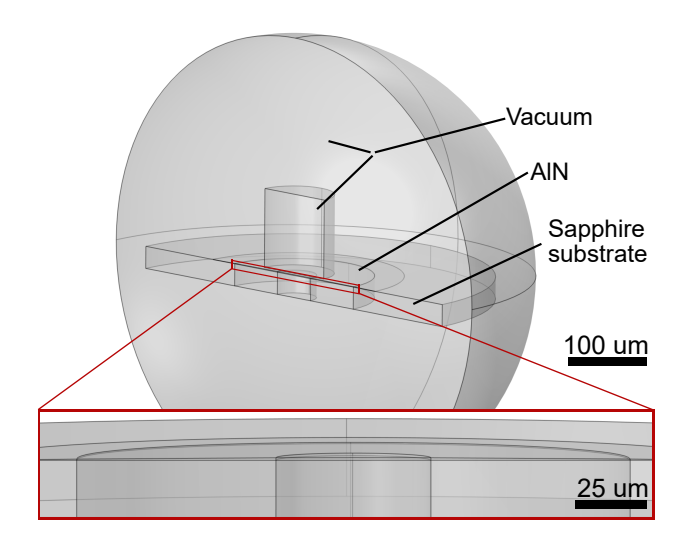


Figure 2.11: Geometry used in the eigenfrequency FEM simulation of the HBAR system. The geometry consists of a sapphire substrate, an AlN piezo dome, and a surrounding vacuum region. The lower inset shows a zoomed-in front view of the *yz*-plane, where the piezo dome is visible. The dimensions are listed in Table 2.2.

The thicknesses  $h_{\rm Sap}$  of the substrate and  $h_{\rm AlN}$  of the piezo layer are chosen such that the longitudinal standing-wave condition is fulfilled at the target frequency  $f_m$ . For the AlN layer we set the thickness to half an acoustic wavelength,

$$h_{\text{AIN}} = \frac{\lambda_{\text{AIN}}}{2} \,, \tag{2.81}$$

while for the sapphire substrate the thickness corresponds to m-1 half-wavelengths,

$$h_{\text{Sap}} = (m-1)\frac{\lambda_{\text{Sap}}}{2} , \qquad (2.82)$$

where m is the longitudinal mode index. Using the longitudinal acoustic velocities  $v = \sqrt{c_{33}/\rho}$  in the respective materials, the thicknesses can be expressed in terms of the target frequency  $f_m$  as

$$h_{\text{AlN}} = \frac{1}{2f_m} \sqrt{\frac{c_{33}^{\text{AlN}}}{\rho^{\text{AlN}}}} \tag{2.83}$$

$$h_{\rm Sap} = \frac{m-1}{2f_m} \sqrt{\frac{c_{33}^{\rm Sap}}{\rho^{\rm Sap}}} \ .$$
 (2.84)

#### **Physics Modules Setup**

To simulate the eigenmodes of the HBAR we use three physics modules: solid mechanics, electrostatics, and the piezoelectric multiphysics interface which couples the first two. In the following we summarize the key settings and boundary conditions that are not automatically implied by the software but are essential to reproduce the correct physics.

Table 2.3: Relevant material parameters for sapphire (substrate) and AlN (piezo) used in the simulation. Matrix elements are given in Voigt notation. Values are taken from [79] (except  $\epsilon_r^{\text{Sap}}$  which was set to 9 in Ref [79]).

Parameter	sapphire (Substrate)	AlN (Piezo)
Relative permittivity $\epsilon_r$	11.6	9.0
Density $\rho$ / kg m <sup>-3</sup>	3980	3300
Elasticity matrix $c_{ij}$ / GPa	$c_{11} = 496$	$c_{11} = 411$
·	$c_{33} = 499$	$c_{33} = 389$
	$c_{44} = 146$	$c_{44} = 125$
	$c_{12} = 159$	$c_{12} = 149$
	$c_{13} = 114$	$c_{13} = 99$
	$c_{14} = -23$	
Piezoelectric matrix $e_{ij}$ / C m <sup>-2</sup>	_	$e_{33} = 1.55$
		$e_{31} = -0.58$
		$e_{15} = -0.48$

**Solid mechanics.** The elastic response is described within linear elasticity, using the full anisotropic stiffness tensor  $c_{ij}$  (see 2.1). The global coordinate system is aligned such that the z-axis coincides with the crystallographic c-axis of both sapphire and AlN. This ensures that longitudinal propagation along z corresponds to the experimentally relevant orientation. All outer boundaries are stress-free, representing the case of a mechanically free-standing resonator. To suppress spurious transverse solutions we constrain the in-plane displacements  $(u_x$  and  $u_y)$  to zero (according to [79]), so that the solver preferentially converges to longitudinally polarized modes, in line with the physics of interest. To avoid artificial reflections from the truncation of the computational domain, low-reflecting boundary conditions are imposed at the outer radial boundary of the substrate.

**Piezoelectric coupling.** Piezoelectricity is included via the multiphysics coupling, which links the elastic strain to the electric polarization through the tensor  $e_{ij}$  using the constitutive equations that were introduced in Eq. (2.16).

**Electrostatics.** No additional conditions are required beyond those automatically applied, apart from the treatment of symmetry (see below). The surrounding vacuum is modeled as a dielectric medium with  $\epsilon_r = 1$ , which allows the piezo-induced field to extend out of the resonator into free space.

**Symmetry.** Because the expected solutions of Laguerre and Hermite-Gaussian modes [79] are invariant under mirror reflection through the xz-plane, we can exploit this symmetry to reduce the simulation volume. We therefore restrict the domain to a half cylinder (cut through the xz-plane) and apply a symmetry boundary condition at the cut plane. This reduces the computation time. Care must be taken, however, when later normalizing fields by volume integrals, as the integration has to be rescaled to account for the reduced simulation domain.

In case one is only interested in modes that are rotationally symmetric one could even reduce the problem to a two-dimensional simulation having z and r as coordinates. However, we would like to have the possibility to look at non-rotationally symmetric modes as well, as they would allow to

couple to different types of atomic transitions (will be discussed in Section 3.1) which is why the full three-dimensional simulation it kept.

#### Meshing procedure and study configuration

Since the accuracy of any FEM simulation is limited by the quality of the spatial discretization, we first outline the meshing strategy adopted for the HBAR geometry which was guided by a publication that simulates the coupling of an HBAR to a superconducting qubit [79, 86]. Afterwards, we describe the solver configuration used to extract the eigenfrequencies.

When solving for the eigenmodes of the HBAR with FEM it is essential that the discretization resolves the relevant physical length scales. In the GHz regime, acoustic wavelengths in sapphire are only a few micrometers (acoustic wavelength at 6 GHz is about 2 µm) whereas the electromagnetic wavelength is several centimeters. This large scale separation means that the mesh must be fine in the acoustic resonator but can be much coarser elsewhere. In particular, the z-direction requires sufficient resolution to capture the standing-wave pattern of longitudinal modes. We therefore impose at least 8 elements per acoustic wavelength in the substrate and piezo layers. Radially, a coarser discretization is sufficient, as the mode profile varies more slowly.

The resulting mesh distribution is illustrated in Fig. 2.12. To keep the problem tractable, the mesh density is gradually reduced away from the active region: the inner resonator volume (substrate plus thin piezo layer) is discretized with a structured mesh of high resolution, which transitions into a coarser unstructured mesh in the surrounding substrate and vacuum. In the vacuum domain, where the electric field varies only slowly, the mesh is refined only in the small region above the piezo dome where the field will later be sampled. The convergence of the results was checked using a mesh refinement study. For that, the mesh density inside the active region was varied (number of elements in z direction and number of mesh nodes in the plane). As a figure of merit, the deviation between the simulated strain profile and a perfect Gaussian envelope (in the plane in the middle of the piezo) was used. An example for the mapped mesh (inner mesh of HBAR cylinder) is shown in Section A.1.

To compute the eigenmodes we used COMSOL's Eigenfrequency Study with the iterative ARPACK solver. The solver was instructed to search for eigenvalues around a shift frequency close to the simple standing-wave estimate from Section 2.3.3. This procedure accelerates convergence and ensures that the physically relevant solutions are found. We typically requested 60 eigenfrequencies around the shift to capture at least the fundamental Gaussian mode and ideally a few higher order modes as well. Apart from these settings, the default solver parameters were used.

#### **Field Normalization**

The eigenfrequency solver returns the mode shapes and frequencies. An output mode shape of e.g. the displacement field will have the following form:

$$\vec{u}(\vec{r}) = H_z(\vec{r})e^{i\phi}\hat{e}_z \,, \tag{2.85}$$

where  $H_z(\vec{r})$  is the spatial mode function and  $\phi$  is an arbitrary phase. The same form applies to the other physical quantities such as the electric field. However, the absolute amplitudes of the fields are arbitrary because the solver does not impose any normalization condition. Since all differential equations are linear, any scaled version of a solution is also a valid solution. To extract physically meaningful quantities such as the single-phonon electric field, we therefore need to impose a normalization condition.

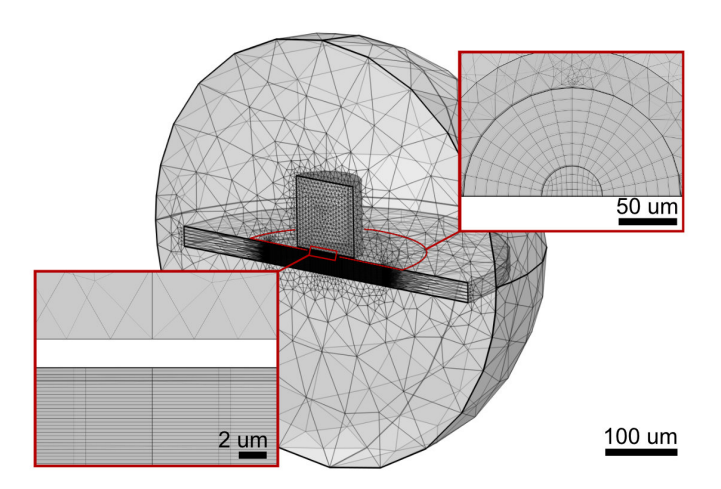


Figure 2.12: Mesh used in the eigenfrequency FEM simulation of the HBAR system. The mesh is fine along the *z*-direction in the resonator region to resolve the acoustic wavelength, and gradually coarsens away from the resonator. The left inset shows a zoomed-in view of the mode confining region of substrate and piezo dome and a small part of the vacuum above. The mesh node density in *z*-direction is high in the resonator compared to the radial direction and the vacuum region. The right inset shows a zoomed-in view of the HBAR center from the top which shows the in plane mesh structure in the mode confining region.

To do so, we use Eq. (2.36) where we calculated the single phonon strain field for an acoustic mode. We ended up with the following result:

$$u_z(\vec{r},t) = \sqrt{\frac{\hbar}{2\rho\omega}} e^{-i\omega t} A H_z(\vec{r}) \cdot \hat{e}_z + \text{c.c.}, \qquad (2.86)$$

where  $H_z(\vec{r})$  is the unnormalized mode shape function we now get from our simulation (here assuming a polarization only in z-direction). The product of A and  $H_z(\vec{r})$  is the normalized mode shape function  $h_z(\vec{r})$ . Therefore, we only have to numerically calculate A according to:

$$A = \left(2 \int_{V_{\text{HBAR}}} dV |H_z(\vec{r})|^2\right)^{-1/2} . \tag{2.87}$$

Important to note is the extra factor of 2 when comparing Eq. (2.37) with Eq. (2.87). This is because we only simulate half of the HBAR volume due to the symmetry condition (see Section 2.3.3). The integral therefore has to be rescaled by a factor of 2 to account for the full volume.

In COMSOL, we implement this normalization in the following way: A *Volume Integration* node is added under the *Definitions* node with the operator name *intop1*. The integration volume is choosen to include the complete substrate and the piezo dome. The normalization constant is then calculated using the integration results by adding a *Variable* node in the *Definitions* with the following definition:

$$A' = (2 \cdot \operatorname{intop1}(\operatorname{real}(w) \cdot \operatorname{real}(w))) , \qquad (2.88)$$

where w is the displacement field in z-direction as given by the solver. Note that we use the real part of

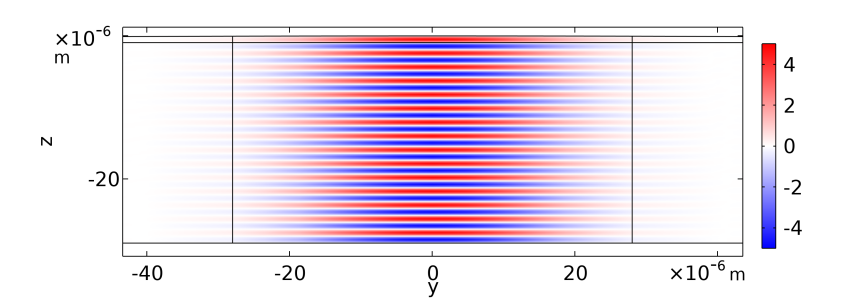


Figure 2.13:  $S_3$  component of strain in the yz-plane at x = 0 for the fundamental Gaussian mode. The strain is normalized to a single phonon using the procedure described in Section 2.3.3 and is given in units of  $10^{-11}$ . The mode has a frequency of 5.81 GHz. The black lines represent the boundaries of the geometry domains. The part below and above the mode is vacuum.

the field, real(w), in the normalization calculation. This is an arbitrary choice, one could e.g. also use the imaginary part imag(w) or the magnitude |w|. Is is only important to stick to one convention in all consequtive calculations.

With this result, all relevant physical quantities such as the electric field can now be properly normalized to a single phonon by multiplying the raw solver output with the normalization constant  $\sqrt{A'}$  and the single phonon displacement amplitude  $u_0 = \sqrt{\frac{\hbar}{2\rho^{\mathrm{Sap}}\omega}}$  (the reason for calculating  $A' = A^2$  is that COMSOL can not handle square roots of numbers with units of odd dimensions. Therefore, in COMSOL we actually apply the square root to the product of A' and  $u_0^2$ ).

#### 2.3.4 FEM Eigenfrequency Simulation: Results

The coupled eigenfrequency simulation serves to verify the results of the electrostatics-based FEM approach and provides access to higher-order acoustic modes and their associated electric fields. Beyond this validation, the method offers a framework to study more complex systems, such as coupling the HBAR to a coplanar waveguide resonator, which will be briefly discussed in Section 2.5. In the following, the results of the coupled simulation are presented and analyzed.

As discussed before, the substrate and piezo thickness were chosen to target the fundamental Gaussian mode of mode index m = 30 where the resonance frequency was expected to lie at 5.8 GHz, only taking acoustics into account. The mode was found at 5.81 GHz which is close to the expected value (dev. of about 0.2%). The strain profile of this mode is shown in Fig. 2.13 where the strain amplitude is normalized using the method from Section 2.3.3. As expected, the strain follows a standing wave pattern in z-direction, half a wavelength lies within the piezo and the mode is confined within the piezo dome in y-direction. Fig. 2.14 shows the displacement field in the xy-plane (also normalized to a single phonon) at the interface of substrate and piezo which follows a Gaussian shape.

#### Comparing the single phonon strain and electric field to the electrostatic simulation

One question that arises is if the strain inside the piezo follows the expected Gaussian profile from Eq. (2.42). Especially it is of interest if the strain amplitudes match as this determines the amplitude of the electric field. Fig. 2.15 shows the simulated strain profile along the y-axis at x = 0 and  $z = -\frac{\lambda^{AIN}}{4}$  (center of piezo layer) for the fundamental Gaussian mode. A Gaussian profile was fitted to the data.

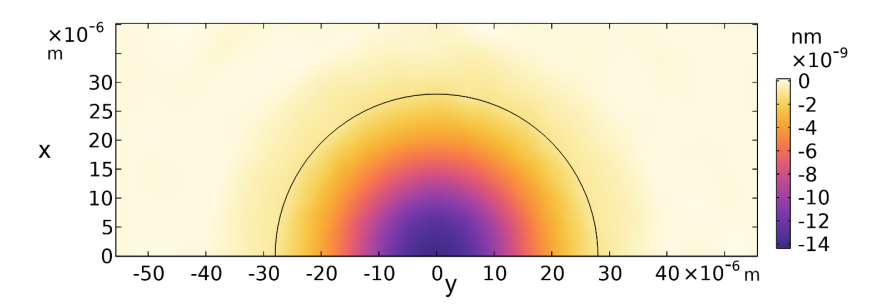


Figure 2.14: *z*-component of the displacement field of fundamental Gaussian mode (same as in upper plot) at the interface of substrate and piezo. The amplitude is normalized to a single phonon.

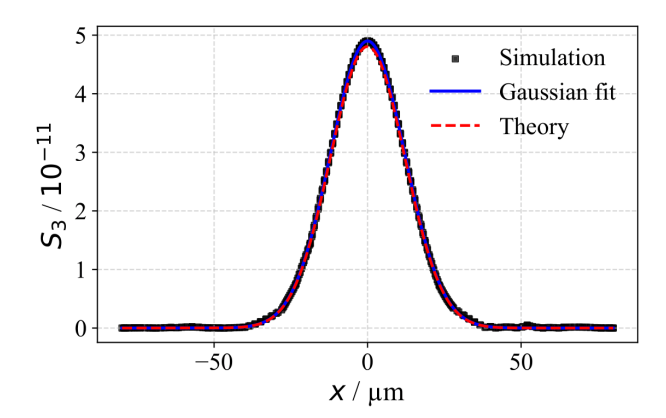


Figure 2.15: Single phonon strain profile inside the piezo (along the y-axis for x = 0 at  $z = -\frac{\chi^{\text{AIN}}}{4}$ ): Squares represent the numerical result from the FEM eigenfrequecy simulation. A Gaussian profile was fitted to the data to determine amplitude and acoustic mode waist. The second Gaussian profile shows the theoretically expected profile (Eq. (2.42)) using the determined mode waist as an input.

Visually, the simulated profile matches the Gaussian profile. The determined mode waist and amplitude is

$$w = 17.13 \,\mu\text{m}$$
 (2.89)

$$S_0 = 4.90 \cdot 10^{-11} \ . \tag{2.90}$$

The mode waist can be used as an input to the expected single phonon strain amplitue from Eq. (2.42) to obtain the theoretically expected amplitude. This gives a value of  $S_0^{\text{theo}} = 4.81 \cdot 10^{-11}$  which deviates about 2% from the fit. This is also shown in Fig. 2.15. It means that the simulated strain profile is in very good agreement with the analytic expression. The remaining deviation can be explained by the fact that the stiffness constant and the material density of AlN and sapphire differ (see Table 2.3) which means a small impedance mismatch. We would therefore expect to not have the exact same amplitude in piezo layer and substrate.

The next thing to look at is the electric field. Fig. 2.16 shows the electric field that is generated by the mode. Qualitatively the shape is the same as we already saw in the electrostatics simulation. One

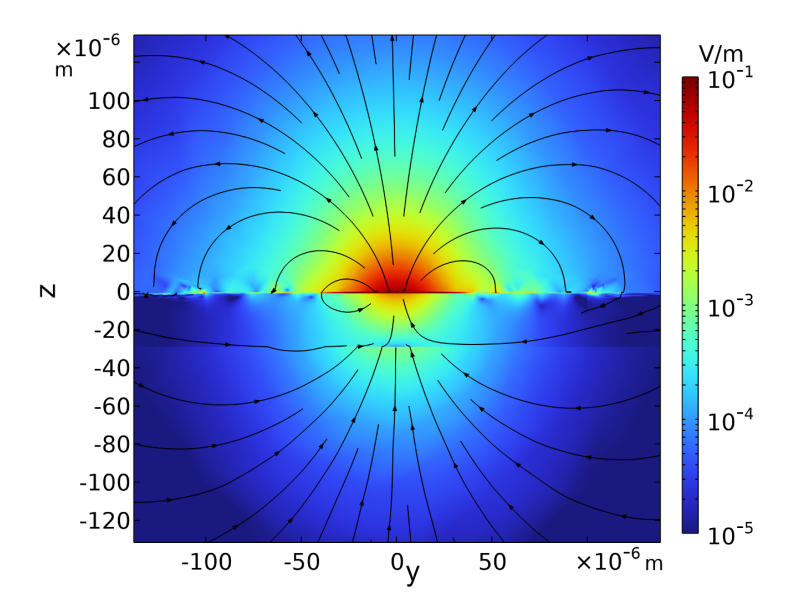


Figure 2.16: Electric field above the piezo dome. The absolute value of the electric field  $|\vec{E}|$  is shown in units of V m<sup>-1</sup>, normalized to a single phonon. The mode is the fundamental Gaussian mode with a frequency of 5.81 GHz. The black stream lines represent the orientation of the electric field vector. Artefacts at the interface of the piezo dome with vacuum towards left and right are unphysical and stem from the coarser mesh distribution at these positions.

thing to note are the artefacts at the vacuum piezo interface at the outer regions (left and right), this is most likely due to the transition from the fine to coarse mesh which was discussed in Section 2.3.3. However, as they are not apparent at the position of the mode or above they should not influence the results significantly. To now compare this quantitavely to the results from the electrostatics simulation we take a look at Fig. 2.17. Here, the electric field above the center of the piezo dome is shown as a function of the distance to the dome surface. The result from the electrostatics simulation is included for comparison. We can see very good agreement between both results. The deviation of 2% of the strain amplitude is taken into account in the plot by normalizing the analytic strain amplitude to the numerically simulated strain amplitude. This means that the electrostatics simulation indeed captures the physics of the HBAR and can be used to efficiently calculate the electric field for different mode waists and substrate thicknesses.

#### Higher order transverse modes

As mentioned in the beginning, we can not only look at the fundamental Gaussian mode but also at higher order transverse modes. One example is shown in Fig. 2.18 where the strain profile of a higher order transverse mode at 5.126 GHz is shown. Fig. 2.19 shows the displacement field of this mode at the interface of substrate and piezo. IThe charge density that arises from this mode we can be thought of as two separated dipoles with opposite phase which effectively leads to a quadrupole like bound charge density distribution. We would therefore expect to see a quadrupole like electric field above the piezo where the field should now point parallel to the piezo surface. This is indeed what we see in Fig. 2.20(a), where the electric field above the piezo dome is shown. The electric field has a quadrupole like structure as expected. In Chapter 3, we will discuss what kind of atomic transitions could be driven with such a

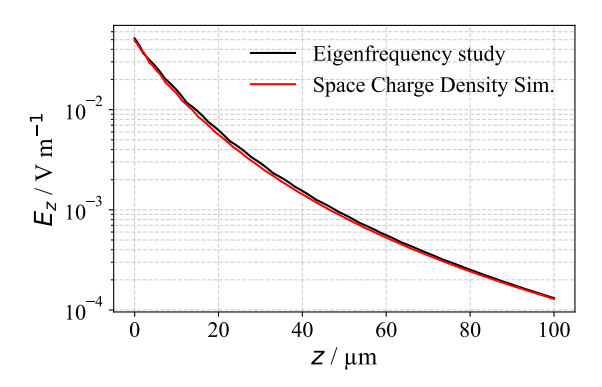


Figure 2.17: Simulated electric field E(z) above the center of the piezo dome as a function of the distance to the dome surface. Result from the FEM Eigenfrequency Analysis is shown in black, while the result from the electrostatic simulation is shown in red. Here, both strain amplitudes are normalized to the same value (the numerically calculated one).

field. For completeness, Fig. 2.20(b) shows the electric field  $E_y(z)$  above the piezo disk which is smaller compared to the fundamental mode (Fig. 2.17) but in the same order of magnitude.

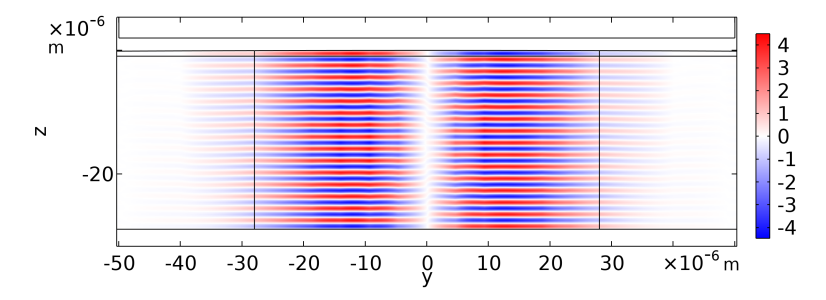


Figure 2.18:  $S_3$  component of strain in the yz-plane at x = 0 for a higher order transverse mode. The strain is normalized to a single phonon using the procedure described in Section 2.3.3 and is given in units of  $10^{-11}$ . The mode has a frequency of 5.8126 GHz. The black lines represent the boundaries of the geometry domains. The part below and above the mode is vacuum.

#### **Conclusion and Outlook**

To conclude, the coupled eigenfrequency simulation reproduces the results of the electrostatics-based approach. The strain profile inside the piezo and the electric field above the center of the dome are consistent with the electrostatics simulation. Furthermore, a higher-order transverse mode was examined, and the electric field distributions follow the expected quadrupole bahviour. With this simulation framework established, it can also be applied to more complex coupled systems in the future, for example including a coplanar waveguide resonator to study the coupling between HBAR and the resonator. We will discuss in Section 2.5 why this is of interest for the experiment.

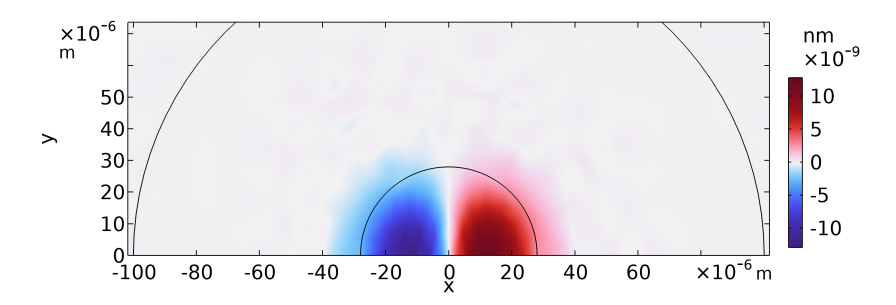
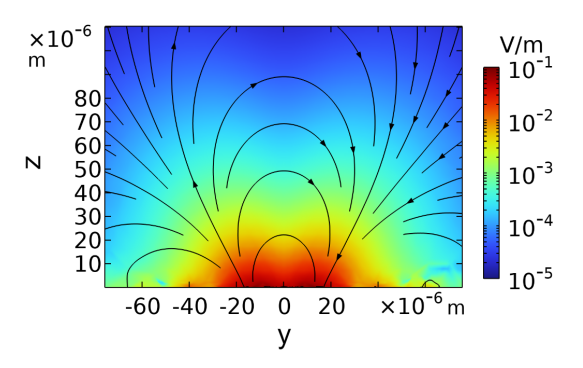
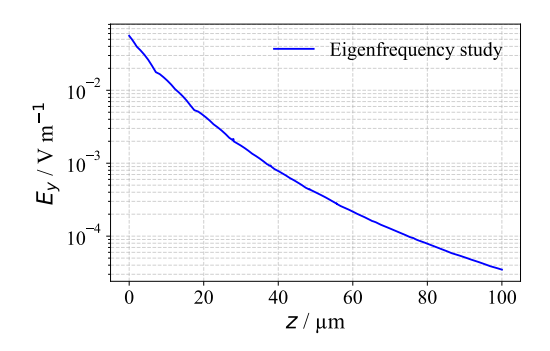


Figure 2.19: *z*-component of the displacement field for a higher order transverse mode (same as in upper plot) at the interface of substrate and piezo, amplitude is normalized to a single phonon.





(a) Electric field above the piezo dome. The absolute value of the electric field  $|\vec{E}|$  is shown in units of V m<sup>-1</sup>. The black stream lines represent the orientation of the electric field vector.

(b) Electric field  $E_y(z)$  above the center of the piezo dome as a function of the distance to the dome surface.

Figure 2.20: Electric field distribution above the piezo dome for a higher order transverse mode with a frequency of 5.8126 GHz. Both results are normalized to a single phonon.

## 2.4 High-Q HBARs for the HQO Experiment

When we want to interface Rydberg atoms with an HBAR, we need to have an HBAR with sufficiently high quality factor to get into the strong coupling regime. For this reason we decided to collaborate with the group of Prof. Yiwen Chu at ETH Zürich, who are working with HBARs in their experiments and reach high quality factors of  $\sim 10^7$  [54] in their experiments at frequencies around 6 GHz. Therefore, Julia Gamper and me went to visit the research group in May 2025.

One important point for us is that the HBAR should have a high quality factor at 4 K. This is important to check as their experiments are conducted at a few mK [46]. Fig. 2.21(a) shows quality factors of a batch of HBARs measured at 4 K for different mode frequencies. One can see that slightly below 6 GHz, where the 85S-85P Rydberg-Rybderg transition lies (the transition we plan to work with), that the best HBARs have quality factors exceeding  $10^7$  which corresponds to linewidths of  $\sim 0.5$  kHz (see Fig. 2.21(b)). These values correspond to HBARs with 420  $\mu$ m substrate thickness. In general, they work with two different substrate thicknesses,  $160 \mu$ m and  $420 \mu$ m. This is important to keep in mind as the substrate thickness influences both the coupling strength and the quality factor. A thicker substrate corresponds to a higher quality factor but lower coupling strength (the best choice for the experiment

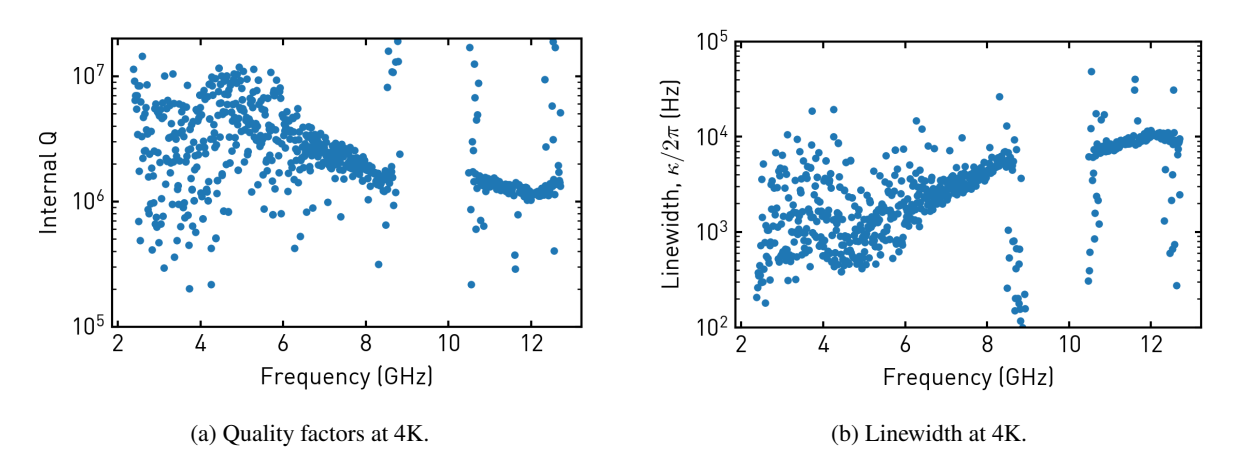


Figure 2.21: High-Q HBAR characterization measurements of fundamental mode for a batch of HBAR chips with a substrate thickness of 420 μm. Images courtesy of Raquel Garcia, ETH Zurich.

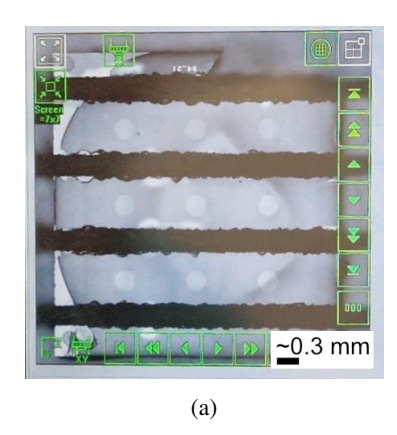
needs to be specified in the future depending on the concrete atom chip design).

Another important point for our experiment is the width of the HBAR chip. For the Rydberg excitation, two lasers need to be focused at the position of the trapped atoms. This means we will have focused beams (few 10 µm) close to a chip surface. Ideally we do not want to have any clipping of the beams at the chip edge for two reasons: Clipping would mean a distortion of the intensity profile of the beam. Second, any heating by the lasers should be prevented. The second point is especially relevant for the blue control laser at 480 nm as it usually outputs a few hundred milliwatts of power. As a consequence, an HBAR chip as narrow as possible is beneficial to have more freedom in the choice of laser beam waist and height position relative to the chip surface. For this reason, it was successfully tried out by members of the group to dice HBAR chips into thin bars with widths < 1 mm. An image that was taken during the dicing in shown in Fig. 2.22(a). Fig. 2.22(b) shows all ten HBARs that were brought to Bonn.

Fig. 2.23(b) shows a microscope image of one of the diced HBAR chip bars. The width was measured to be around 700 µm. This gives us a figure of merit how thin we can get with the chip. Going for chips of smaller widths is challenging for different reasons. The most obvious reason is that the dome of the HBAR has to fit onto the chip. Second, a chip of smaller width is more likely to just fly away during the dicing process. The last point is mechanical handling of the chip which gets a difficult for smaller widths.

To show that a width of around 700  $\mu$ m is already sufficient for our experiment we can look at the plots in Fig. 2.24(a) and Fig. 2.24(b). (a) shows the 780 nm probe beam profile and the top of the HBAR chip for one slice through the center of chip and beam for a focus waist of 8  $\mu$ m (as it is currently built in our experiment [58]). (b) shows the same plot for the control beam at 480 nm (with a focus waist of 15  $\mu$ m, which is not fixed yet). The Figures show the scenario that both beams are positioned 35  $\mu$ m above the chip surface. This distance is already very optimistic but geometry wise possible, first experiments will most likely be performed with the atoms further away (50  $\mu$ m – 100  $\mu$ m). For the chosen parameters, there is no significant clipping (no clipping within twice the beam waist).

The available HBARs could already be used in the experiment, but their resonance frequencies and quality factors need to be characterized first. At the same time, the simulation tools developed in the previous Section now allow us to determine the electric field amplitude for any atomic transition, mode waist, and substrate thickness. This enables us to think about the parameters most suitable for our



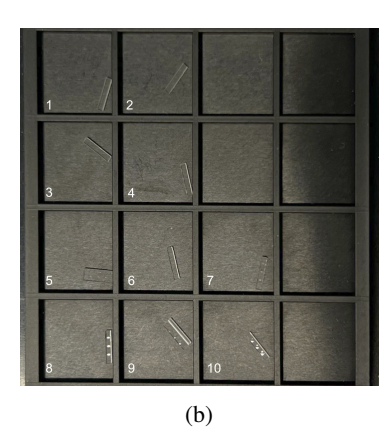
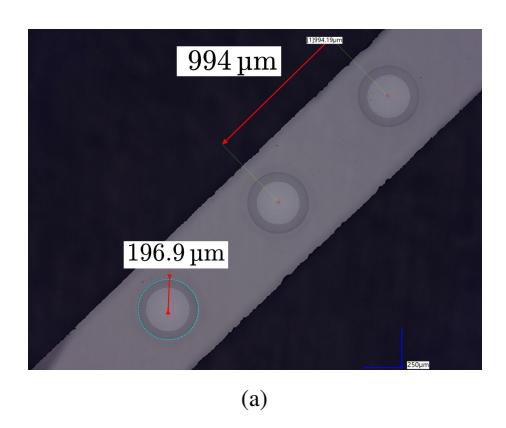


Figure 2.22: Image (a) taken during the dicing process at ETH Zurich. It shows a sapphire chip with 3x3 HBARs. The chip was diced horizontally to get 3 thin bars with 3 domes on each bar. The domes are visible as the filled ring structures on the bars. The black areas are the parts that were taken apart by the dicing saw. Image courtesy of Julia Gamper. (b) shows ten diced HBAR chip bars (two flew away during the dicing) that were taken to Bonn, in some of them one can see the three domes as light reflections. White numbers represent assigned labels which will become important at the moment the HBARs are characterized.



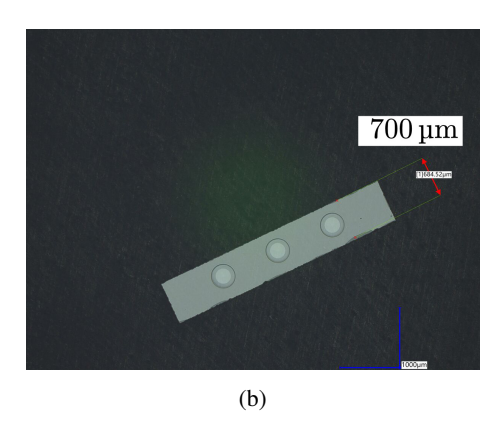


Figure 2.23: Size measurements of one of the diced HBAR chip bars. (a) shows the characterization of the dome (dome radius and distance to neighbour). (b) shows the chip width along the beam propagation axis. The width was measured to be around 700 µm. Images courtesy of Raquel Garcia, ETH Zurich.

experiment and to consider the fabrication of an HBAR optimized for our experiment.

## 2.5 Towards an Implementation into the Experiment

Up to this point, we have discussed how an HBAR works and simulated the electric field that it generates. Additionally, real HBARs for our experiment that originated from a collaboration with Prof. Yiwen Chu's research group in Zurich were presented. In this section, we will discuss the qualitative aspects of how an implementation in the HQO experiment could look like. For more details about the atom chip, the reader is referred to Section 4.1 and Ref [62].

An idea for an implementation is shown in Fig. 2.25. The HBAR is attached to two holders which are attached to the atom chip surface. The holders have two functions. First, the active acoustic region of the

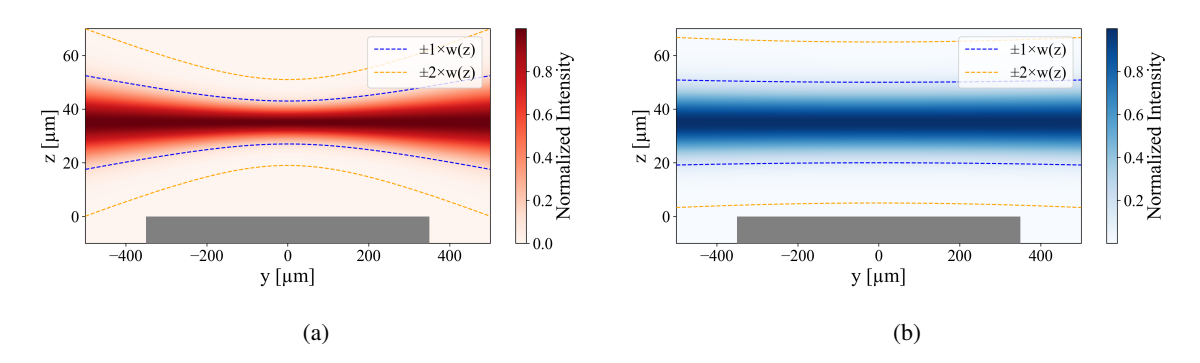


Figure 2.24: Plots show the intensity profile of probe and control beam above the HBAR chip. (a) shows the probe beam (780 nm) and (b) shows the control beam (480 nm). The beams are focused to a waist of 8  $\mu$ m and 15  $\mu$ m with the waist position 35  $\mu$ m above the HBAR. The beams are propagating in y-direction and the top of the HBAR is placed at z=0 (The dome is not plotted as it is negligibly small in height). One sees no clipping at the chip within two times the waist size.

HBAR is sorounded by vacuum which is necessary to have no losses into the chip. Second, the holders are chosen of such a height that the laser beams do not clip at the edges of the atom chip. Fig. 2.26 shows a cut through the probe beam profile above the atom chip. At a distance of about 400 µm above the chip, there is no clipping of the beam at the chip edge. The control beam is not shows as the beam divergence is smaller and therefore never the limiting factor.

The supercoducting trapping wire in Fig. 2.25 can trap the atoms above the HBAR dome. The exact trapping position and relative distance to the dome can be controlled by the applied currents and external magnetic fields. More details on that can be found in Ref [62]. In addition to the trapping wire, a superconducting coplanar waveguide resonator is present on the chip. It is coupled capacitively to the microwave feed lines (more details also in Ref [62]). This resonator can be used to classically drive the HBAR. This would provide strong classical atom–HBAR coupling and a practical first step before single-phonon interactions. In this regime the atoms can also serve as probes of the resonator surface (e.g., mapping adsorbate-induced stray fields). Here, care must be taken to stay in the undercoupled regime such that the quality factor is still determined by the high intrinsic quality factor of the HBAR and not through the external coupling [87].

One cruicial part, which is not shown in the sketch, is the required precise electric field compensation at the position of the atoms via electrodes with externally applied electric fields. This is necessary to compensate for any stray electric fields from e.g. adsorbates on the chip surface [88–91]. Here, more time will be needed to specify the exact requirements on these compensation electrodes and to design them accordingly.

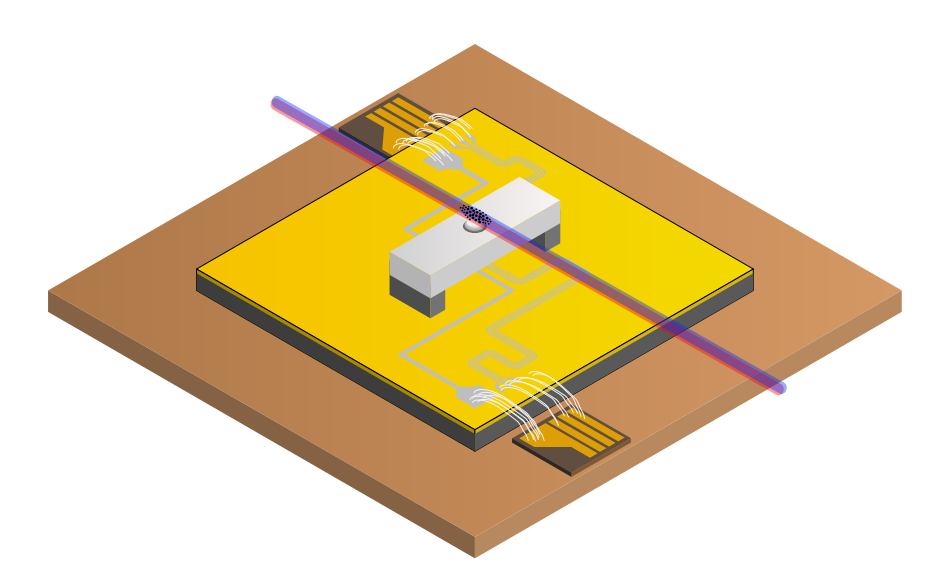


Figure 2.25: Sketch of a possible implementation of the HBAR into the HQO experiment. The HBAR is mounted on two holders which are attached to the atom chip surface. The holders have two functions: First, they sorround the active acoustic region of the HBAR with vacuum which is necessary to have no losses into the chip. Second, they are chosen of such a height that the laser beams do not clip at the edges of the atom chip. The atoms can be trapped above the dome of the HBAR via a superconducting trapping wire on the atom chip. A superconducting coplanar waveguide resonator is capacitively coupled to microwave feed lines and can be used to drive the HBAR and/or the atoms.

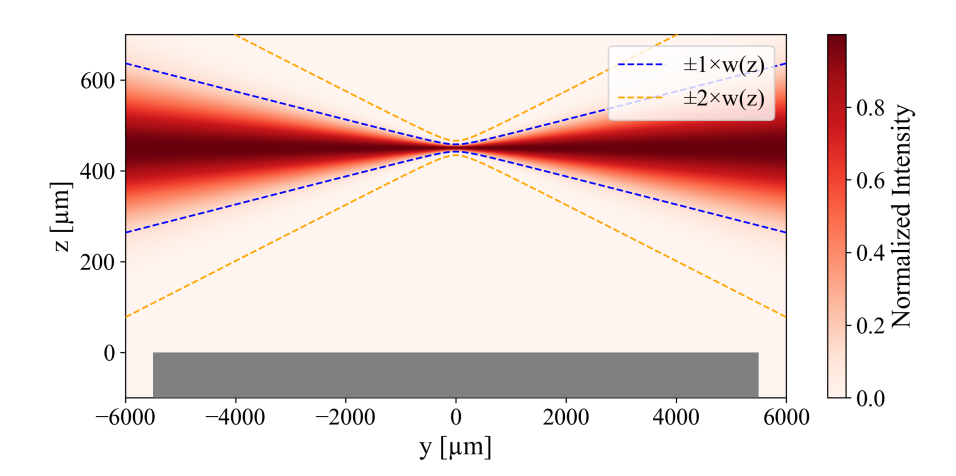


Figure 2.26: Cut through the probe beam profile above the atom chip (HBAR is not shown in this image, it would sit on top of the atom chip). The beam is focused to a waist of  $8 \, \mu m$  with the waist position  $\sim 400 \, \mu m$  above the atom chip. The beam is propagating in y-direction. One sees no clipping at the chip within two times the waist size for a chip width of  $11 \, mm$  (our current design [62]).

# Interfacing Rydberg Atoms with an HBAR

In the previous chapter we had a quantitative look into the physics of high overtone bulk acoustic wave resonators. We discussed how acoustic modes can be confined in the resonator, how piezoelectricity works, and how we can use the piezoelectric effect to couple atoms to the acoustic field of the resonator. Ultimately, the oscillating electric field of the HBAR was simulated. The electric field is essential to calculate how well a Rydberg atom can couple to the resonator. In this chapter we will now look into the calculation of the coupling strength between the two using the simulated electric field. After this, we will look into one application of the coupling which is the cooling of one resonator mode close to the quantum mechanical ground state using Rydberg atoms as a refrigerant. The cooling mechanism will be explained and a simulation of the cooling process will be presented.

## 3.1 Coupling Rydberg Atoms to an HBAR Mode

Assume we have an atom excited to a Rydberg state, in the following called  $|nS\rangle$ , that is coupled to a higher lying Rydberg state  $|nP\rangle$  via the electric field of an HBAR mode. The two states form a two level system with transition frequency  $\omega_{SP}$ . The HBAR, as discussed in Section 2.1.3, can be treated as a harmonic oscillator. If the atomic transition frequency  $\omega_{SP}$  is resonant with the frequency of the HBAR mode  $\omega_m$ , we can describe the coupled system with the Jaynes-Cummings model in the following form [92]:

$$H = \hbar \omega_m \hat{a}^{\dagger} \hat{a} + \hbar \omega_m |nP\rangle \langle nP| + \hbar \frac{\Omega_{\text{HBAR}}}{2} \left( |nP\rangle \langle nS| \, \hat{a} + |nS\rangle \langle nP| \, \hat{a}^{\dagger} \right) \,, \tag{3.1}$$

where  $\hat{a}$  and  $\hat{a}^{\dagger}$  are the annihilation and creation operators for the oscillator mode, respectively,  $|nS\rangle$  and  $|nP\rangle$  are the ground and excited states of the two-level system,  $\omega_m$  is the frequency of the HBAR mode and the Rydberg-Rydberg transition and  $\Omega_{\rm HBAR}$  is the single-phonon Rabi frequency. The single-phonon Rabi frequency is given by:

$$\Omega_{\rm HBAR} = \frac{\langle nP|\hat{e}_p \cdot \hat{d}|nS\rangle E_0}{\hbar} , \qquad (3.2)$$

where  $\hat{e}_p$  is the electric field polarization vector at the position of the atom,  $\hat{d}$  is the dipole moment operator, and  $E_0$  is the real amplitude of the electric field. Throughout this thesis we will work with



Figure 3.1: Sketches of electric field shape for two different HBAR modes with external magnetic field and defined coordinate system. The left shows the case for a fundamental Gaussian mode where the electric field points orthogonal to the piezo surface. The right shows a higher order mode where the electric field points parallel to the piezo surface. The red and blue ellipses indicate the strain profile inside the resonator.

 $\Omega_{\rm HBAR}$  as the figure of merit of the coupling strength between the atom and the resonator mode. Note that in the literature the coupling strength is often given as  $g = \frac{\Omega_{\rm HBAR}}{2}$ , which is half the single-phonon Rabi frequency [80].

Fig. 3.1 shows the situation we consider for the calculation of  $\Omega_{HBAR}$ . The atoms will be trapped by a magnetic trap above the piezo surface. The magnetic trapping results in a non-vanishing magnetic field at the trap potential minimum (more details in ref [62]). We will use the field to define the quantization axis of the atoms. We stick to the coordinate system from Fig. 3.1 as it is consistent with standard notation in atomic physics. From Section 2.3.4 we know that there are two cases for the electric field, it either points in the orthogonal direction to the piezo surface, which we will call  $\vec{E}_{\perp}$ , or parallel to it, called  $\vec{E}_{\parallel}$ . Using the circular basis, we can write both fields in the following form:

$$\vec{E}_{\perp} = E_0^{\perp} \hat{e}_y = \frac{E_0^{\perp}}{\sqrt{2}} (\hat{e}_{\sigma+} + \hat{e}_{\sigma-})$$
 (3.3)

$$\vec{E}_{\parallel} = E_0^{\parallel} \hat{e}_z = E_0^{\parallel} \hat{e}_{\pi} \tag{3.4}$$

where  $\hat{e}_{\pi}$  and  $\hat{e}_{\sigma\pm}$  are the electric field polarization vectors in the circular basis. As a result, a parallel pointing field couples to  $\pi$  transitions, while a perpendicular field couples to both  $\sigma^+$  and  $\sigma^-$  transitions. In case the levels are split too far apart by the Zeeman shift, only coupling to either the  $\sigma^+$  or  $\sigma^-$  transition is possible, which reduces the Rabi frequency by a factor  $\sqrt{2}$ . Under these assumptions, the single-phonon Rabi frequencies reduce to:

$$\Omega_{\rm HBAR}^{\perp} = \frac{d_{\sigma \pm} E_0^{\perp}}{\hbar \sqrt{2}} \tag{3.5}$$

$$\Omega_{\rm HBAR}^{\parallel} = \frac{d_{\pi} E_0^{\parallel}}{\hbar} \tag{3.6}$$

where  $d_{\sigma^{\pm}}$  and  $d_{\pi}$  are the absolute values of the dipole matrix elements for the corresponding transitions. In the first place there are no plans to work with higher order transversal modes of the HBAR, and the fundamental mode only results in an electric field perpendicular to the piezo surface. Therefore, we only consider  $\Omega^{\perp}_{\text{HBAR}}$  in the following sections.

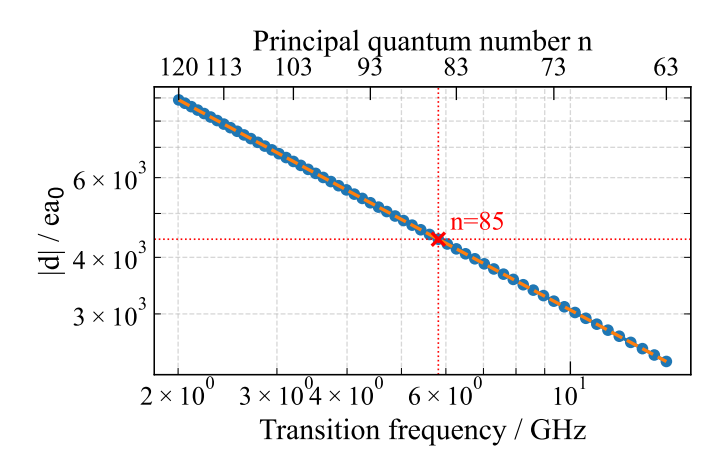


Figure 3.2: Dipole matrix elements for different  $\sigma^+$ ,  $nS \leftrightarrow nP$  transitions as a function of the transition frequency. The dashed line has a slope of -2/3 and indicates a scaling of  $|d| \propto f^{-2/3}$ . The red cross indicates the dipole matrix element for the  $85S_{1/2} \leftrightarrow 85P_{3/2}$  transition at 5.8 GHz. Matrix elements were calculated using the ARC library [63].

#### 3.1.1 Scaling of Coupling Strength with Transition Frequency

Using the results from Chapter 2, we can now calculate explicit values for  $\Omega_{\rm HBAR}$ . Before calculating the value of  $\Omega_{\rm HBAR}$  for a specific transition, we first consider how  $\Omega_{\rm HBAR}$  scales with the resonator frequency  $\omega_m$ . In Section 2.3.2 we derived the frequency dependence of the electric field amplitude. We found that the electric field amplitude scales with the resonator frequency  $\omega_m$  as  $E_0 \propto 1/\sqrt{\omega_m}$ . However, we are interested in the coupling strength which scales with the product of the electric field amplitude and the corresponding transition dipole matrix element (see Eqs. (3.5) and (3.6)). Fig. 3.2 shows the dipole matrix element of the  $\sigma^+$  transition as a function of the transition frequency. The dipole matrix element scales as  $|d| \propto \omega^{-2/3}$ , and therefore, the single-phonon Rabi frequency scales as:

$$\Omega_{\rm HBAR} \propto E_0 \cdot |d| \propto \omega_m^{-7/6} .$$
(3.7)

#### 3.1.2 Coupling Strength for the $85S_{1/2} \leftrightarrow 85P_{3/2}$ Transition

In this Section, we will calculate concrete values for the coupling strength  $\Omega_{\rm HBAR}$  for the  $|85S_{1/2}\rangle \leftrightarrow |85P_{3/2}\rangle \sigma^+$  transition. This transition has a frequency of  $\omega/2\pi \approx 5.82$  GHz and a dipole matrix element of  $d_{\sigma+}\approx 4400$  ea<sub>0</sub> (calculated using the ARC library [63]).

The calculations are performed for different parameter combinations, specifically we vary the atomresonator distance, the substrate thickness and the piezo coupling constant. The results are shown in Table 3.1. For the atom-resonator distance, we use two different distances, the originally planned distance of 50 µm, and a shorter distance of 35 µm, which is theoretically achievable (see Section 2.4). For the substrate thickness, we align our calculations with the samples produced by the ETH group as discussed in Section 2.4. The group produces two different substrate thicknesses. Finally, we also use two different values for the piezo coupling constant, the value  $e_{33} = 1.55 \,\mathrm{C\,m^{-2}}$  and the very optimistic case of  $e_{33} = 2.25 \,\mathrm{C\,m^{-2}}$ .

Table 3.1: Single–phonon electric field amplitudes and resulting coupling strengths for the  $\left|85S_{1/2}\right\rangle \leftrightarrow \left|85P_{3/2}\right\rangle \ \sigma^+$  transition at  $f_m \approx 5.82$  GHz for different atom–resonator distances z, substrate thicknesses L, and piezoelectric coefficients  $e_{33}$ .  $w_{\rm opt}$  is the acoustic mode waist used (from Section 2.3.2).  $E_0$  is the simulated single–phonon field amplitude at z.  $\Omega_{\rm HBAR}$  is the single–phonon Rabi frequency;  $\Omega_{\rm HBAR}^{\rm (eff)}$  includes the  $1/\sqrt{2}$  reduction from Eq. (3.5).

z / μm	L/μm	$e_{33}$ / C m <sup>-2</sup>	w <sub>opt</sub> / μm	$E_0$ / mV m <sup>-1</sup>	$\Omega_{ m HBAR}/2\pi$ / kHz	$\Omega_{ m HBAR}^{ m (eff)}/2\pi$ / kHz
35	160	1.55	23.74	0.897	50.4	35.6
35	160	2.25	23.74	1.303	73.1	51.7
50	160	1.55	32.29	0.434	24.3	17.2
50	160	2.25	32.29	0.629	35.3	25.0
35	420	1.55	23.74	0.554	31.1	22.0
35	420	2.25	23.74	0.804	45.1	31.9
50	420	1.55	32.29	0.268	15.0	10.6
50	420	2.25	32.29	0.388	21.8	15.4

We can define the cooperativity as a measure for how deep in the strong-coupling regime the system is [92]

$$C = \frac{\Omega_{\rm HBAR}^2}{\gamma_R \kappa} \,, \tag{3.8}$$

where  $\gamma_R$  is the decay rate of the Rydberg state and  $\kappa$  is the linewidth of the resonator mode. Assuming a Rydberg decay rate of  $\gamma_R \sim 2\pi \cdot 1$  kHz and a resonator linewidth of  $\kappa = 2\pi \cdot 0.5$  kHz (see Section 2.4), we can calculate the cooperativity for the different scenarios in Table 3.1 and see that we are in the strong coupling regime with C > 1 for all cases. However, the values are calculated without taking thermal population of the resonator mode into account, which we will discuss in the next Section.

# 3.2 Rydberg Atoms as a Refrigerant for Ground State Cooling of an HBAR Mode

We have now established the coupling mechanism between the HBAR mode and a Rydberg atom. Using the results for the electric field from Section 2.3.2, we quantified the expected coupling strength in Section 3.1. Due to the small linewidths of the HBAR and the Rydberg states, we determined that the coupled system is in the strong coupling regime. However, the experiment will happen at a finite temperature of 4 K. As a result, the oscillator will be in a thermal state described by the mean phonon number  $\langle n_{\rm th} \rangle$  [93], and not in the vacuum fock state:

$$\langle n_{\rm th} \rangle = \frac{1}{e^{\hbar \omega_m / k_B T} - 1} \,, \tag{3.9}$$

where  $\omega_m$  is the frequency of the resonator mode and T is the temperature. At 5.8 GHz and 4 K this would result in a mean occupation number of  $\langle n_{\rm th} \rangle \approx 14$ . This thermal occupation prohibits coherent atom–resonator dynamics unless the HBAR is first cooled close to its ground state. This would be possible by going to even lower temperatures, e.g. to a few mK as can be reached in a dilution refrigerator [6, 53]. However, a dilution refrigerator would make the experiment much more complicated, especially

in the combination with trapped atoms and optical lasers as dilution refrigerators have significantly less cooling power than a convetional 4 K cryostat [94, 95]. However, with the Rydberg atoms we already have a tool at hand that we can use to cool the resonator mode. By coupling to the resonator, the atoms can absorb excitations, and through a controlled dissipation channel, this energy can be removed from the system before it returns to the resonator. In the following, it will be motivated how this can be realized. In the following Sections, we will discuss how to simulate this cooling process and how one could implement it experimentally.

#### 3.2.1 Coupled Atom-Resonator System

Fig. 3.3 shows the complete system. It consists of the HBAR at finite temperature T, where one mode is coupled to ultracold Rydberg atoms, loaded above the chip and close to the resonator surface. The atoms are excited to the Rydberg state by the red and blue laser using a two photon transition. Because of the finite temperature, we can treat the HBAR mode of interest as coupled to a thermal bath at temperature T. There is a heating  $\Gamma_h$  and a cooling rate  $\Gamma_c$  associated with this bath [93]:

$$\Gamma_h = (\langle n \rangle + 1) \langle n_{\text{th}} \rangle \kappa \tag{3.10}$$

$$\Gamma_c = -\langle n \rangle (\langle n_{\rm th} \rangle + 1) \kappa \tag{3.11}$$

where  $\kappa = \frac{\omega_m}{Q_m}$  is the linewidth of the resonator mode,  $Q_m$  is the quality factor of mode m,  $\omega_m$  is the frequency of mode m, and  $\langle n \rangle$  is the mean phonon number of the mode. The thermal bath will lead to a steady state mean phonon number of  $\langle n_{\rm th} \rangle$  in the resonator mode if there is no other interaction mechanism.

Now, the HBAR mode is coupled to the Rydberg atoms, and can therefore exchange energy with them. The upper Rydberg state of the atoms is coupled to a decay channel which dissipates the energy once the excitation via an acoustic phonon happened (depicted as  $\Gamma_{dis}$  in Fig. 3.3). This means going from the strong coupling regime to the weak coupling regime on purpose to only allow for energy transfer out of the resonator. After the dissipation happened, the atom can be excited back to the lower Rydberg state. In this way, the atom can continuously absorb energy from the resonator and dissipate it into the environment. The aim would be to achieve an energy dissipation via the atoms that is significantly faster than the heating rate from the thermal bath to significantly reduce the phonon number in the HBAR mode

If we have N atoms participating in the cooling process, and we assume that the dissipation rate does not depend on the phonon number in the resonator, we can write the change of the mean phonon number as [93]:

$$\frac{d\langle n\rangle}{dt} = \Gamma_h + \Gamma_c - N \cdot \Gamma_{\text{dis}} \cdot \langle n\rangle , \qquad (3.12)$$

where the equilibrium phonon number  $\langle n \rangle_{\rm eq}$  is given by setting  $\frac{d\langle n \rangle}{dt} = 0$ :

$$\langle n \rangle_{\rm eq} = \frac{\langle n_{\rm th} \rangle_{\kappa}}{\kappa + N \cdot \Gamma_{\rm dis}} \ .$$
 (3.13)

Under the assumption that the resonator linewidth is small compared to  $N \cdot \Gamma_{\text{dis}}$ , Eq. (3.13) can be written as:

$$\langle n \rangle_{\rm eq} \approx \frac{\langle n_{\rm th} \rangle \kappa}{N \cdot \Gamma_{\rm dis}} \ .$$
 (3.14)

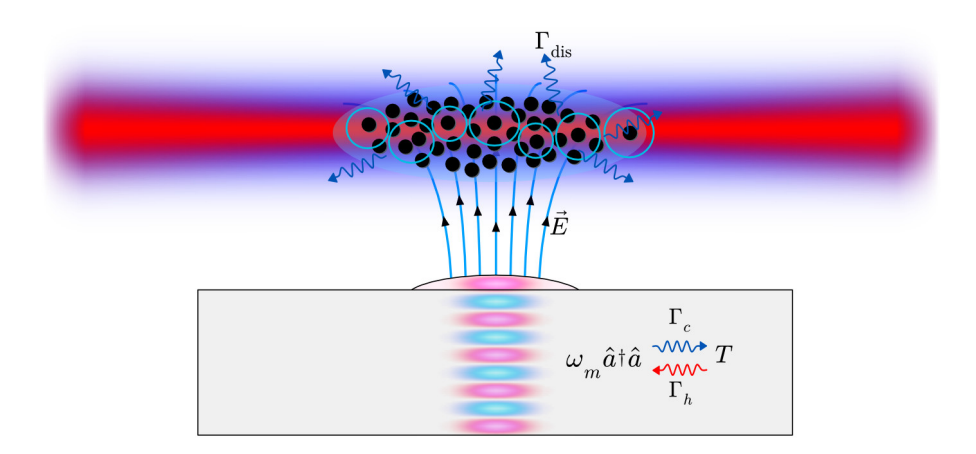


Figure 3.3: A sketch of the coupled atom–resonator system. The HBAR mode is coupled to a thermal bath at temperature T which leads to a heating and cooling rate  $\Gamma_h$  and  $\Gamma_c$ , respectively. The Rydberg atoms are coupled to the resonator mode via the piezoelectric effect and can dissipate energy via a controlled dissipation channel with rate  $\Gamma_{\rm dis}$ . The two lasers represent excitations lasers to excite atoms to the Rydberg state via a two photon transition.

This means to bring the HBAR mode close to its ground state, we require

$$N\Gamma_{\rm dis} > \langle n_{\rm th} \rangle \kappa ,$$
 (3.15)

which can be achieved by either increasing the number of atoms N and/or the dissipation rate  $\Gamma_{\rm dis}$ . Eq. (3.13) provides useful intuition and yields a simple condition for near-groundstate cooling. However, it relies on the simplifying assumption that the dissipation rate  $\Gamma_{\rm dis}$  is independent of the resonator state. To capture the full dynamics and determine  $\Gamma_{\rm dis}$  for our system, we next turn to a Lindblad master equation description of the coupled atom–resonator system. We will return to Eq. (3.13) later to estimate the scaling of  $\langle n \rangle_{\rm eq}$  with atom number and compare it to the simulation results.

#### 3.2.2 Cooling with Single Rydberg Atoms

In order to simulate the system shown in Fig. 3.3, we first consider the simplest case of just a single atom. This could for example be achieved by trapping a single atom inside an optical tweezer above the HBAR. Fig. 3.4 shows an implementation of a continuous-wave based cooling scheme. The ground state  $|g\rangle$  of the atom is coupled to a lower Rydberg state  $|nS\rangle$  with effective Rabi frequency  $\Omega$  and detuning  $\Delta$ . The lower Rydberg state is coupled to an upper Rydberg state  $|nP\rangle$  via the interaction with the HBAR mode with strength  $\Omega_{\rm HBAR}$ . To introduce the required dissipation channel, the upper Rydberg state is coupled to an intermediate state  $|e\rangle$  with effective Rabi frequency  $\Omega'$  and detuning  $\Delta'$ . The intermediate state decays fast with rate  $\gamma_e$  to the ground state  $|g\rangle$ . The Rydberg states themselves are characterized by their natural linewidths  $\gamma_{nS}$  and  $\gamma_{nP}$ , respectively, which are assumed to be much smaller than  $\gamma_e$ . The HBAR is coupled to the thermal bath at temperature T which leads to the heating and cooling rates discussed in Eqs. (3.10) and (3.11). This cooling process has been theoretically studied in Ref [96], where the authors simulate cooling of a superconducting microwave cavity using Caesium Rydberg atoms. Mathematically, this system is equivalent to ours (the mathematical description of this system will not be covered here,

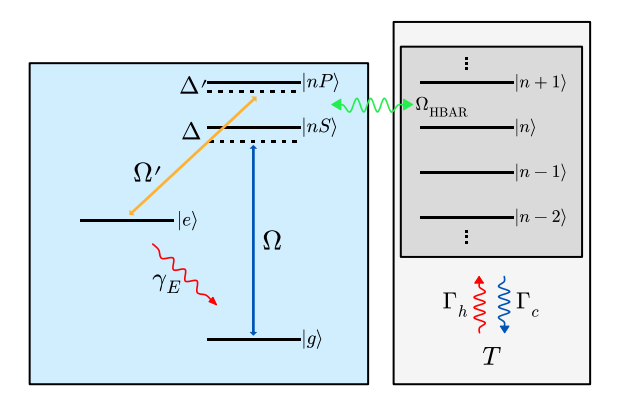


Figure 3.4: The atomic level scheme for the cooling process with single atoms. The ground state  $|g\rangle$  is coupled to the lower Rydberg state  $|nS\rangle$  with effective Rabi frequency  $\Omega$  and detuning  $\Delta$ . The upper Rydberg state  $|nP\rangle$  is coupled to the intermediate state  $|e\rangle$  with effective Rabi frequency  $\Omega'$  and detuning  $\Delta'$ . The lower and upper Rydberg states are coupled to the HBAR mode with strength  $\Omega_{\rm HBAR}$ . The intermediate state  $|e\rangle$  decays with rate  $\gamma_e$  to the ground state. The HBAR is coupled to the thermal bath at temperature T which leads to the heating and cooling rates discussed in Eqs. (3.10) and (3.11).

please refer to Ref [96] or to Section 3.3.1 where we will discuss the mathematical description for the ensemble case, the single atom case can be inferred from that). Here, we will discuss some results that are of interest for us. The main motivation is to understand why it is beneficial to have an ensemble of atoms instead of single atoms, where we can make use of the Rydberg blockade effect.

Fig. 3.5(b) shows the phonon number distribution in the resonator mode, which is a reproduced result from Ref [96]. The distribution is shown before the cooling process (thermal state with  $\langle n_{\rm th} \rangle = 5.1$ ) and after the cooling process, in the thermal equilibrium. Interestingly, the final state in the resonator is not a thermal state anymore, as the deviation from a thermal distribution with the same mean phonon number shows. The final state has an increased population of the zero phonon fock state and a decreased population of the next higher fock states. For the larger phonon numbers (n > 7) the population is increased again compared to the thermal state. As explained in Ref [96], this is a result of a larger splitting for higher lying fock states which shifts these out of resonance in the cooling process. This is the reason why the dissipation rate  $\Gamma_{\rm dis}$  in Eq. (3.12) is not independent of the phonon number in the resonator. We will come back to this in the outlook (Section 3.3.2) where we discuss possible improvements of the resonator cooling process.

The second result of interest is shown in Fig. 3.5(a). It shows the time evolution of the expectation values of the atomic state population as a function of time for the same simulation parameters as in Fig. 3.5(b). We can see that after the thermal equilibrium is reached, we still have a significant fraction of the population in  $|g\rangle$  ( $\sim 40\%$ ) and in  $|e\rangle$  ( $\sim 15\%$ ). The fraction in these two states does not participate in the cooling process, which reduces the cooling efficiency.

In order to reduce the population in the states that do not contribute to the cooling, we first consider how to reduce the population fraction in  $|e\rangle$ . This state is populated via the dissipation channel. The population in this state can be reduced by increasing the decay rate  $\gamma_e$ . However, one is experimentally limited by the achievable decay rate. Assuming the fastest decay rate in Rb-87 of the 5*P*-state of  $\sim$  6 MHz [97] for the state  $|e\rangle$  one could maximally achieve an effective decay rate of the upper Rydberg state of  $\gamma_e/2/2\pi \sim$  3 MHz [80]. In case the coupling strength between the atoms in the resonator is on the

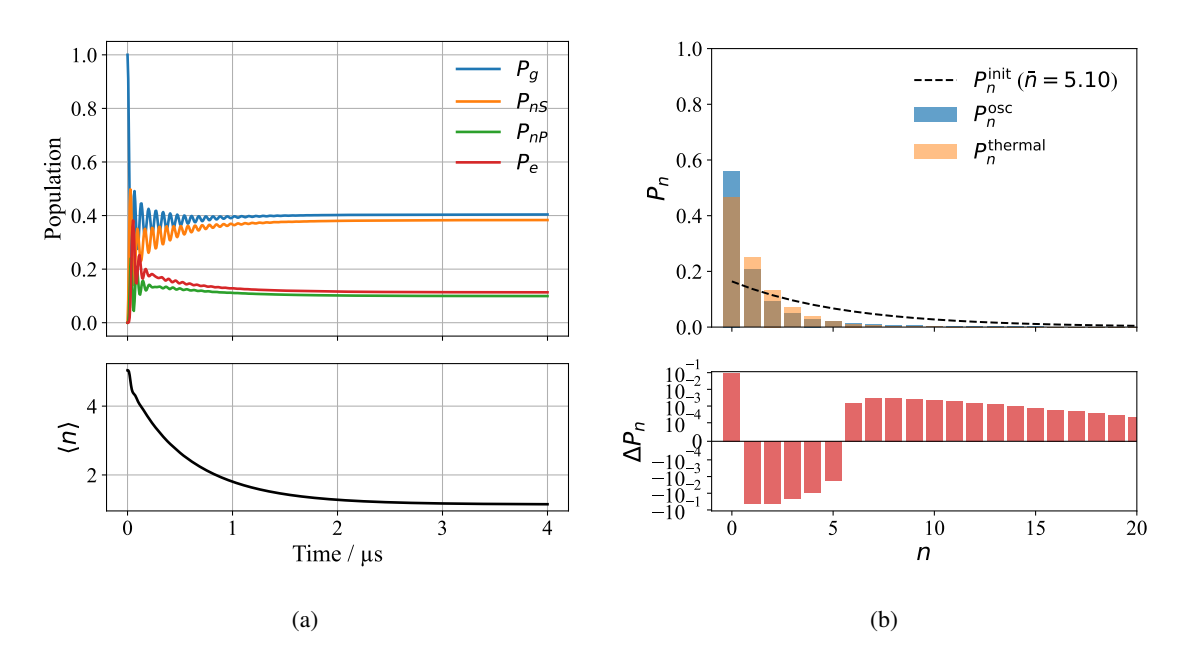


Figure 3.5: (a) Lower plot is a reproduction of Fig. 4.b) from Ref [96]. It shows the mean phonon number of the resonator as a function of time. Upper plot shows the population of the atomic states as a function of time for the same simulation parameters. (b) A reproduction of Fig 4.b) from Ref [96]. It shows the phonon number distribution in the resonator mode before the cooling process (thermal state with  $\langle n_{\rm th} \rangle = 5.1$ ) and after the cooling process in the thermal equilibrium. Simulation parameters are the same as in the reference. The thermal distribution with the same mean phonon number as the final state is shown for comparison. The lower plot shows the deviation of the final state from the thermal distribution of same mean.

same order of magnitude or larger than  $\gamma_e/2$ , the cooling efficiency is fundamentally limited by the possible effective decay rate of the upper Rydberg state (also mentioned in Ref [96]). To circumvent this bottleneck, one can make all other timescales in the system smaller by reducing the coupling strength between the atoms and the resonator and also the decay rate of the resonator itself (meaning higher quality factors). In this way, the smaller coupling strength is compensated by an increase of the resonator lifetime, but one is not limited by the effective decay rate of the upper Rydberg state anymore. This is the case for our system where we expect to have smaller coupling strengths on the order of  $\geq 10 \, \mathrm{kHz}$  (see Section 3.1.2) compared to  $\geq 1 \, \mathrm{MHz}$  in ref [96] but also two orders of magnitude better quality factors of  $Q \sim 10^7$  (see Section 2.5) compared to the values used in Ref [96] where they assumed  $Q = 10^5$  for calculating the time evolution shown in Fig. 3.5(a).

Population in  $|g\rangle$  is also a problem in the proposed system of Ref [96]. In our system, however, population in  $|g\rangle$  does not pose a big problem. This difference is caused by a very important difference between the system proposed in Ref [96] and our system. Ref [96] considers a single atom coupled to the resonator, while we will have an ensemble of atoms (a cloud) coupled to the resonator. We will discuss why this enables us to reduce the fraction of ground state population for the cooling process and how we can model this cooling process in the next Section.

#### 3.2.3 Cooling with Rydberg Superatoms

In the case of an ensemble of atoms, the interaction between Rydberg atoms must be considered. Due to the large polarizability of Rydberg states, two Rydberg atoms excited to an S-state will interact strongly via van-der-Waals interactions [35]. If we have two atoms excited to a Rydberg state, there will be an energy shift of the doubly excited state due to this interaction that depends on the separation of the two atoms which scales with  $1/r^6$  [98] where r is the distance between them. This leads to the so called Rydberg blockade effect. There is a radius related to the distance where the interaction-induced energy shift of the pair state exceeds the linewidth of the excitation laser, called the blockade radius  $r_b$ . If  $N_a$  atoms are inside the volume defined by the blockade radius, only one of  $N_a$  atoms can be excited to a Rydberg state. A typical blockade radius is on the order of  $10 \, \mu m$  [40].

For now, we will assume to have a cloud of atoms, that can be adressed by the exciation lasers, with a volume that is smaller than the blockade volume. As in Section 3.2.2, we have a single Rydberg atom available for the cooling process. But there is one important distinction: The  $N_a$  atoms inside the blockade volume will form a collective state [36], a so called superatom. There will be a collective ground state

$$|G\rangle = \left|g_1, g_2, ..., g_{N_a}\right\rangle$$

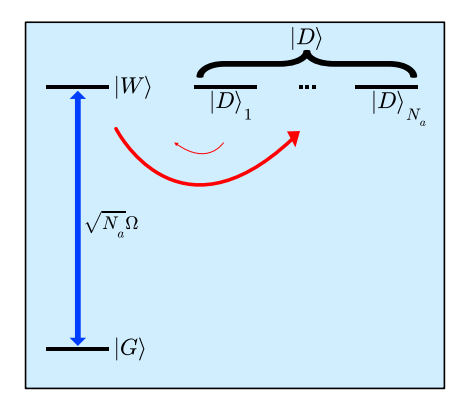
and a collective bright state

$$|W\rangle = \frac{1}{\sqrt{N_a}} \sum_{i=1}^{N_a} \left| g_1, g_2, ..., r_i, ..., g_{N_a} \right\rangle$$

where  $|r_i\rangle$  is the Rydberg state of atom i. One feature of this collective state is the enhanced coupling between the collective ground state and the collective bright state, which scales as  $\sqrt{N_a}\Omega$  [25, 39], where  $\Omega$  is the single atom Rabi frequency. However, there are also  $N_a-1$  other states  $|D\rangle_1,...,|D\rangle_{N_a-1}$  that are orthogonal to the bright state. They do not couple to the ground state via the driving field [25]. However, there are dephasing mechanism, such as atomic motion [99], that can lead to a dephasing of the bright state into the dark states. In case  $N_a\gg 1$ , the probability to rephase from a dark state back into the bright state is very small [100]. This allows to combine all  $N_a-1$  dark states into a single dark state  $|D\rangle$  where we now have a single dephasing rate  $\gamma_D$  from the bright state  $|W\rangle$  into the dark state  $|D\rangle$ . This 2+1 level system is illustrated in Fig. 3.6.

Most experiments put a lot of effort into keeping the dephasing into the dark states low, as they are a loss channel for the coherent dynamics between the ground state and the bright state which leads to a fast dephasing of the collective Rabi oscillations [28, 101]. However, in our case, this dephasing into the dark states is beneficial. The dark states are still Rydberg states and can therefore couple to the resonator mode. However, they are not coupled to the atomic ground state via the driving field anymore. In the past, this feature was used to realize a single photon absorber [26, 100]. Here, the idea is that if a single photon excites the collective bright state, it will quickly dephase into the dark states. Since the dark states do not couple to the ground state anymore, they cannot emit the photon back.

This means that atoms can be transferred fast into a long-lived Rydberg state that is decoupled from the driving field. This is exactly what we want for the cooling process, as it allows reducing the fraction of atoms in the ground state and therefore increases the number of atoms that can participate in the cooling process. By tuning the ratio between the Rabi frequency  $\Omega$  of the driving field and the dephasing rate  $\gamma_D$ , one can control the dynamics of the population transfer from the ground state to the dark states



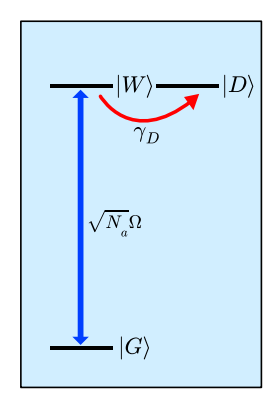


Figure 3.6: Left side shows the states of the collective system. The ground state  $|G\rangle$  is coupled to the bright state via a driving field with Rabi frequency  $\Omega$ . The  $N_a-1$  dark states are not coupled to ground state via the driving field. There are dephasing rates between the bright state and any dark state. The dephasing into the dark states can be combined into a single dephasing rate  $\gamma_D$  from the bright state into a representative dark state  $|D\rangle$  and the dephasing back into the bright state can be neglected for  $N_a \gg 1$ . The right side shows the simplified 2+1 level system where all dark states are combined into a single dark state  $|D\rangle$ .

[100]. Fig. 3.7 shows the time evolution of the driven 2+1 level system for three different cases (here, any decays to the ground state are neglected which is justified because the drive and the dephasing can be made much larger than the decay [25]). The blue line represent the underdamped case where Rabi oscillations between  $|G\rangle$  and  $|W\rangle$  are still visible. The green line shows the overdamped case where the population is transferred to the dark states without oscillations. The orange line shows the critically damped case where the population is transferred to the dark states in the shortest time. As a reference, we assume an experimentally determined dephasing rate of  $\gamma_D/2\pi=1.4\,\mathrm{MHz}$  [25] which can be increased by e.g. increasing the temperature of the atoms to increase atomic motion. Comparing this to the coupling to the HBAR we find

$$\gamma_D \gg \Omega_{\rm HBAR}$$
.

This already suggests that by making use of the Rydberg blockade effect which gives rise to collective effects, we will be able to significantly increase the number of atoms that can participate in the cooling process as the pumping process from  $|G\rangle$  into the Rydberg state happens on fast time scales compared to the atom-resonator interaction. In the next Section, we will simulate the cooling process using the 2+1 level system described here.

## 3.3 Simulation of the Cooling Process

In the last Section, we motivated why it is beneficial to use an ensemble of atoms instead of single atoms for the cooling process. In the following, we will discuss how to simulate this cooling process and show results for experimentally realistic parameters.

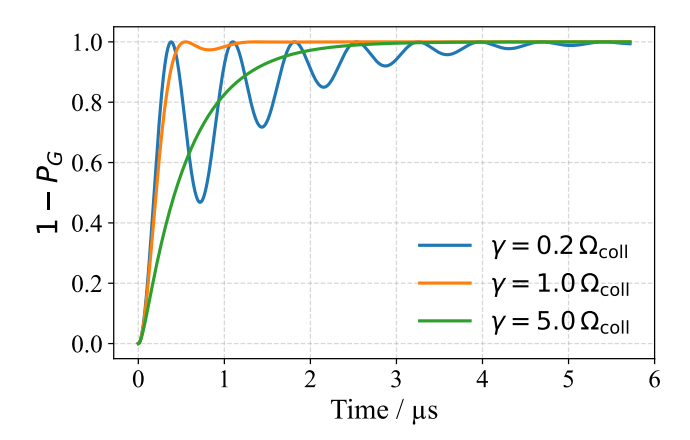


Figure 3.7: Rydberg population dynamics are shown for three different ratios of dephasing rate  $\gamma_D$  and collective Rabi frequency  $\sqrt{N_a}\Omega$ . The critically damped case (orange) shows the fastest transfer of population from the ground state into the dark state. The overdamped case (green) shows a slower transfer without oscillations. The underdamped case (blue) shows Rabi oscillations between the ground state and the bright state before the population is transferred to the dark state. Simulation parameters:  $\sqrt{N_a}\Omega/2\pi = 1.4\,\mathrm{MHz}$ .

#### 3.3.1 Superatom HBAR Cooling Scheme

We will now couple a Rydberg superatom to the HBAR mode and simulate the cooling process. For now, we will stick to the case that our ensemble of atoms, that is addressable by our lasers, is smaller than the blockade volume which only allows for a single Rydberg excitation in the ensemble. In Section 3.3.2 we will discuss how the cooling scheme performs in case of multiple Rydberg excitations.

#### **System Description**

The system we now consider is shown in Fig. 3.8. Additionally to the shown drives and decays, each of the three Rydberg states has its natural linewidth  $\gamma_{nS}$  and  $\gamma_{nP}$ . Before we discuss the Hamiltonian of the system, we will point out the relevant properties of the collective states. As stated in the last Section, there is a single collective bright state  $|W\rangle$  and  $N_a-1$  collective dark states. We combine all  $N_a-1$  dark states into a single representative dark state  $|D\rangle$  and assume that the bright state dephases into this state with rate  $\gamma_D$  without a dephasing mechanism back to  $|W\rangle$ . For the coupling to the resonator mode, it does not matter in which exact dark state we are because the resonator only couples to the single Rydberg excitation that is present in the ensemble and not to the collective state. The single Rydberg excitation is present in all states, also all dark states.

Having established that we can treat our ensemble of atoms as a single superatom, we can now write down the Hamiltonian of the complete system. It consists of the Hamiltonian of the collective atomic system, the Hamiltonian of the resonator mode, and the interaction between the two:

$$H_{\text{tot}} = H_{\text{atom}} \otimes \mathbb{I}_{\text{osc}} + \mathbb{I}_{\text{atom}} \otimes H_{\text{osc}} + H_{\text{int}}, \qquad (3.16)$$

where  $H_{\rm atom}$  is the Hamiltonian of the collective atomic system,  $H_{\rm osc}$  is the Hamiltonian of the resonator mode, and  $H_{\rm int}$  describes the interaction between the two.  $\mathbb{I}_{\rm atom}$  and  $\mathbb{I}_{\rm osc}$  are identity operators in the respective subspaces. The collective atomic system consists of five states: the collective ground state

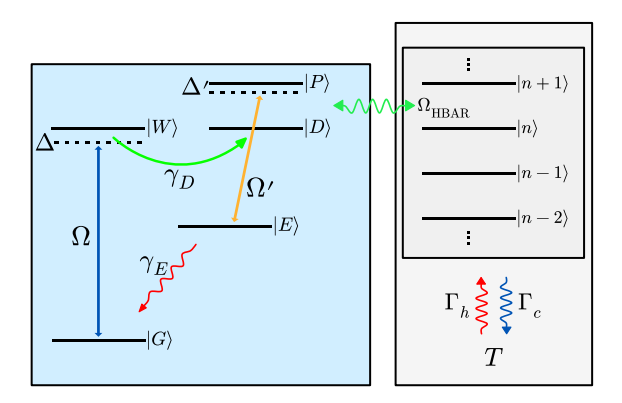


Figure 3.8: The atomic level scheme for the cooling process with an ensemble of atoms. The collective ground state  $|G\rangle$  is coupled to a collective bright Rydberg state  $|W\rangle$  with collective Rabi frequency  $\Omega$  and detuning  $\Delta$ . There are  $N_a-1$  collective dark states that are degenerate with the bright state, which are combined into a single dark state  $|D\rangle$ . The bright state dephases into  $|D\rangle$  with rate  $\gamma_D$ . The upper Rydberg state is now a collective state as well, called  $|P\rangle$ . It is coupled to an intermediate state  $|E\rangle$  with effective Rabi frequency  $\Omega'$  and detuning  $\Delta'$ . The intermediate state decays with rate  $\gamma_E$  to the collective ground state. The lower and upper collective Rydberg states are coupled to the HBAR mode with strength  $\Omega_{\rm HBAR}$ . Natural decay rates of the Rydberg states are not shown.

 $|G\rangle$ , a collective bright Rydberg state  $|W\rangle$ , a collective dark Rydberg state  $|D\rangle$  (representative for all  $N_a-1$  dark states), an upper Rydberg state  $|P\rangle$ , and an intermediate state  $|E\rangle$  that provides a dissipation channel. There are two classical drives present in the atomic system (for the simulation, we treat two photon transitions as an effective one photon transition with an associated effective driving strength): One between the ground state and the bright Rydberg state with Rabi frequency  $\Omega$  and laser frequency  $\omega$ , and one between the upper Rydberg state and the intermediate state with Rabi frequency  $\Omega'$  and laser frequency  $\omega'$ . The bright and dark Rydberg states are assumed to be degenerate. Note that we set  $\hbar=1$  for the rest of this Section.

To work with this Hamiltonian, we transform into an appropriate rotating frame for the atomic system and apply the rotating wave approximation (RWA). We end up with the following time-independent Hamiltonian (see Section A.2 for a derivation):

$$\begin{split} H &= \omega_m \hat{a}^\dagger \hat{a} & \text{HBAR mode} \\ &- \Delta \left| W \right\rangle \left\langle W \right| - \Delta \left| D \right\rangle \left\langle D \right| & \text{lower Rydberg state (bright and dark)} \\ &- \left( \Delta - \omega_m \right) \left| P \right\rangle \left\langle P \right| & \text{upper Rydberg state} \\ &- \left( \Delta - \Delta' - \omega_m \right) \left| E \right\rangle \left\langle E \right| & \text{intermediate state for energy dissipation} \\ &+ \frac{\Omega}{2} \left( \left| W \right\rangle \left\langle G \right| + \left| G \right\rangle \left\langle W \right| \right) & \text{Rabi drive: ground} \leftrightarrow \text{Rydberg} \\ &+ \frac{\Omega'}{2} \left( \left| E \right\rangle \left\langle P \right| + \left| P \right\rangle \left\langle E \right| \right) & \text{Rabi drive: } \left| P \right\rangle \leftrightarrow \left| E \right\rangle \text{ for energy dissipation} \\ &+ \frac{\Omega_{\text{HBAR}}}{2} \left( \left| P \right\rangle \left( \left\langle D \right| + \left\langle W \right| \right) \otimes \hat{a} + \left( \left| D \right\rangle + \left| W \right\rangle \right) \left\langle P \right| \otimes \hat{a}^\dagger \right) & \text{coupling to HBAR mode} \end{split} \tag{3.17}$$

where  $\Delta = \omega - (\omega_W - \omega_G)$  and  $\Delta' = \omega' - (\omega_P - \omega_E)$  are the detunings of the two-photon transitions

from the respective atomic transitions, and  $\omega_{\rm Ryd} = \omega_P - \omega_W = \omega_m$  is the Rydberg-Rydberg transition frequency which is set to be resonant with the resonator mode frequency. The operators  $\hat{a}$  and  $\hat{a}^{\dagger}$  are the annihilation and creation operators for the resonator mode, respectively, and  $\Omega_{\rm HBAR}$  is the single-phonon Rabi frequency that characterizes the coupling strength between the upper Rydberg state and the dark Rydberg state via the resonator mode (see Section 3.1).

On top of the coherent dynamics described by the Hamiltonian, there are several incoherent processes present in the system. As discussed, the bright state  $|W\rangle$  dephases into the dark state  $|D\rangle$  with a rate  $\gamma_D$ . All three Rydberg states have a natural decay rate  $\gamma_{nS}$  (for  $|W\rangle$  and  $|D\rangle$ ) and  $\gamma_{nP}$  (for  $|P\rangle$ ), respectively. In addition, the bright state  $|W\rangle$  has an enhanced spontaneous emission rate due to the driving field [25] into the driving field mode. Since we do not care about the mode of the emitted photon, we can combine the natural decay and the enhanced decay into a single decay rate called  $\gamma_W$ . The intermediate state  $|E\rangle$  decays with rate  $\gamma_E$  to the collective ground state  $|G\rangle$ . The oscillator is coupled to the thermal bath at temperature T which leads to the heating and cooling rates discussed in Eqs. (3.10) and (3.11). From this, the following collapse operators can be constructed:

$$\begin{split} L_{\gamma_D} &= \sqrt{\gamma_D} \, |D\rangle \, \langle W| & \text{dephasing: } |W\rangle \to |D\rangle \\ L_{\gamma_{nS}} &= \sqrt{\gamma_{nS}} \, \sqrt{\gamma_{nS}} \, |G\rangle \, \langle D| & \text{decay: } |D\rangle \to |G\rangle \\ L_{\gamma_W} &= \sqrt{\gamma_W} \, |G\rangle \, \langle W| & \text{decay: } |W\rangle \to |G\rangle \\ L_{\gamma_{nP}} &= \sqrt{\gamma_{nP}} \, |G\rangle \, \langle P| & \text{decay: } |P\rangle \to |G\rangle \\ L_{\gamma_E} &= \sqrt{\gamma_E} \, |G\rangle \, \langle E| & \text{decay: } |E\rangle \to |G\rangle \\ L_{\Gamma_c} &= \sqrt{\kappa} \, (\langle n_{th} \rangle + 1) \hat{a} & \text{cooling: } |n\rangle \to |n-1\rangle \text{ in HBAR mode} \\ L_{\Gamma_h} &= \sqrt{\kappa \langle n_{th} \rangle} \hat{a}^\dagger & \text{heating: } |n\rangle \to |n+1\rangle \text{ in HBAR mode} \end{split} \tag{3.18}$$

With this, we can write down the master equation of the system in Lindblad form (we use the notation from Ref [102]):

$$\dot{\rho}(t) = -i[H, \rho(t)] + \sum_{k} \frac{1}{2} \left( 2L_{k}\rho(t)L_{k}^{\dagger} - \{L_{k}^{\dagger}L_{k}, \rho(t)\} \right) , \qquad (3.19)$$

where  $\rho(t)$  is the density matrix of the system, H is the Hamiltonian from Eq. (3.17), and  $L_k$  are the collapse operators that describe the incoherent processes and are defined above.

This system can be numerically solved with the Quantum Toolbox in Python (QuTiP) [102] to obtain the time evolution of the expectation values and the steady state solution. For the simulation, the parameters from Table Table 3.2 are fixed. The decay rates of the Rydberg states are calculated with the ARC library [63]. For the decay rate of the  $|E\rangle$  state, we use the rate of the 5P state of Rb-87 [97]. The coupling strength  $\Omega_{\rm HBAR}/2\pi$  is set to  $20\,\rm kHz$ , which was obtained in Section 3.1.2 for a substrate thickness of 420  $\mu$ m and an atom-resonator distance of 35  $\mu$ m. For the dephasing rate into the dark states, experimental values from Ref [25] were used. The drive  $\Omega$  was chossen according to Section 3.2.3 to get the fastest population transfer into the Rydberg state. The enhanced decay rate of the bright state  $|W\rangle$  can be controlled by the number of atoms and the strength of the driving field [25]. For now, a value of  $100\,\rm kHz$  is used.

- D	X 7 1	D ' ' '
Parameter	Value	Description
$\gamma_D/2\pi$	1.4 MHz	Bright-to-dark dephasing rate
$\gamma_E/2\pi$	$6\mathrm{MHz}$	Decay rate of intermediate state $ E\rangle$
$\gamma_{ m nS}/2\pi$	$1.4\mathrm{kHz}$	Natural decay rate of lower Rydberg state $ nS\rangle$
$\gamma_{ m W}/2\pi$	$100\mathrm{kHz}$	Enhanced decay rate of bright state $ W\rangle$
$\gamma_{ m nP}/2\pi$	$0.7\mathrm{kHz}$	Natural decay rate of upper Rydberg state $ nP\rangle$
$\kappa/2\pi$	$0.5\mathrm{kHz}$	Linewidth of the HBAR mode
$\omega_m/2\pi$	5.8 GHz	Frequency of the HBAR mode (and the atomic transition)
$\Omega/2\pi$	1.4 MHz	Collective Drive Rabi frequency $ G\rangle \leftrightarrow  W\rangle$
$\Delta/2\pi$	$0\mathrm{MHz}$	Detuning of the ground-to-Rydberg drive
T	4 K	Bath temperature

Table 3.2: Fixed simulation parameters for the 5-Level Superatom-Resonator Cooling Simulation from Section 3.3.1

#### Results

With the simulation, it is possible to determine the performance of the cooling scheme and optimize the dissipation channel parameters. Here, we can tune the drive  $\Omega'$  between  $|E\rangle$  and  $|P\rangle$  and the detuning  $\Delta'$  to optimize the effective decay rate of the upper Rydberg state. Fig. 3.9 shows the mean phonon number in the HBAR in the steady state in dependence of these two parameters. We can see that there is an optimum for the drive and detuning where the mean phonon number is minimized at

$$\Omega'/2\pi = 0.56 \,\text{MHz}$$

$$\Delta'/2\pi = 0 \,\text{MHz}. \tag{3.20}$$

The result that a detuning of zero yields the best results agrees with Ref [96]. One can see a steep increase of the final mean phonon number when reducing  $\Omega'$  and a slower increase when increasing  $\Omega'$ . This can be explained by the fact that for small  $\Omega'$ , energy can not be extracted before it is transferred back to the resonator which means we start to enter the strong coupling regime between the atom and the resonator which we on purpose want to avoid for the cooling. For large  $\Omega'$ , the upper Rydberg state linewidth is broadened too much to efficiently extract energy from the resonator. Because of the broad linewidth of  $|E\rangle$ , the mean phonon number is not very sensitive to the exact value of  $\Delta'$  compared to the drive  $\Omega'$ .

Using the engineered dissipation channel, we can now look at the time evolution of the system. Fig. 3.10(a) shows the time evolution of the mean phonon number in the HBAR mode and the expectation values of the population of the atomic states. We can see that the mean phonon number decreases from the initial thermal value of  $\langle n \rangle \approx 14$  to a final value of

$$\langle n \rangle \approx 1.78$$
.

The population of the atomic states shows that we were able to completely depopulte  $|E\rangle$  (bellow 0.1% in the steady state) and significantly reduce the population in  $|G\rangle$  to about 1% in the steady state. Furthermore, after short initial dynamics, there is no significant population in the bright state  $|W\rangle$  left. The majority of the population is now in either  $|D\rangle$  or  $|P\rangle$ . About 87% of the atomic population is in the dark state  $|D\rangle$  which acts as the cooling reservoir. This is a significant enhancement compared to the single atom case shown in Fig. 3.5(a) where the population in the lower Rydberg state is only about 40%.

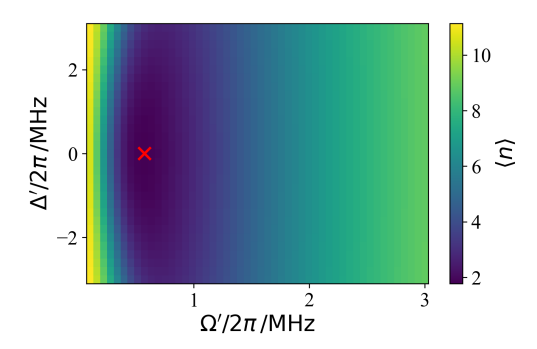


Figure 3.9: A heatmap of the final mean phonon number in dependence of the drive  $\Omega'$  and detuning  $\Delta'$ , that engineer the dissipation channel, is shown. An optimum can be observed at  $\Omega'/2\pi = 0.56$  MHz and  $\Delta'/2\pi = 0$  MHz where the mean phonon number is minimized at  $\langle n \rangle \approx 1.78$  (marked by a red cross). Simulation parameters are the same as in Table 3.2.

As a results, we can conclude that cooling with an ensemble of atoms is significantly more efficient than cooling with a single atom, although we can in both cases have only a single Rydberg atom excited at a time.

Two points remain of interest. We would like to know how the final state resonator population depends on the number of superatoms that take part in the cooling process. So far, we only simulated the cooling scheme performance for a single superatom. Furtheremore, the described observation of reduced population in  $|W\rangle$  and  $|E\rangle$  suggests to conceptionally simplify the system which would also allow for simulation of more atoms. We will disucss both points in the next Sections.

#### 3.3.2 Simplified Superatom HBAR Cooling Scheme

From the discussion, it becomes clear that we can conceptually simplify this system which will allow for easier interpretation and simulation of multiple superatoms coupled to the HBAR. The simplified system is shown in Fig. 3.11. The five level atomic system is now reduced to a three level system. We have a collective ground state  $|G\rangle$ , a collective Rydberg state  $|S\rangle$  (representative for the dark state  $|D\rangle$ ), and an upper Rydberg state  $|P\rangle$ . The irreversible transfer from the ground state to the dark states via the superatom dephasing is now modeled with a pump rate  $\gamma_{\text{pump}}$  that pumps population from  $|G\rangle$  to  $|S\rangle$ . The two Rydberg states are still coupled via the interaction with the HBAR mode. The upper Rydberg state can decay via a dissipation channel to the ground state with a decay rate  $\gamma_P$  that can be engineered. The natural decay rates of the Rydberg states are still included. We now assume to have N superatoms coupled to the same HBAR mode. For simplicity, we will assume the same coupling strength between the atom and the HBAR for all N atoms. Note that this N now specifies the number of superatoms and is different from  $N_Q$  from the previous Section which was the number of atoms inside a single superatom.

The Hamiltonian of this simplified system with *N* superatoms is given by the following expression, which is just *N* two-level systems coupled to a harmonic oscillator:

$$H = \omega_{m} \hat{a}^{\dagger} \hat{a} + \sum_{i}^{N} \omega_{m} |P\rangle_{i} \langle P|_{i} + \sum_{i}^{N} \frac{\Omega_{\text{HBAR}}}{2} \left( |P\rangle_{i} \langle S|_{i} \otimes \hat{a} + |S\rangle_{i} \langle P|_{i} \otimes \hat{a}^{\dagger} \right). \tag{3.21}$$

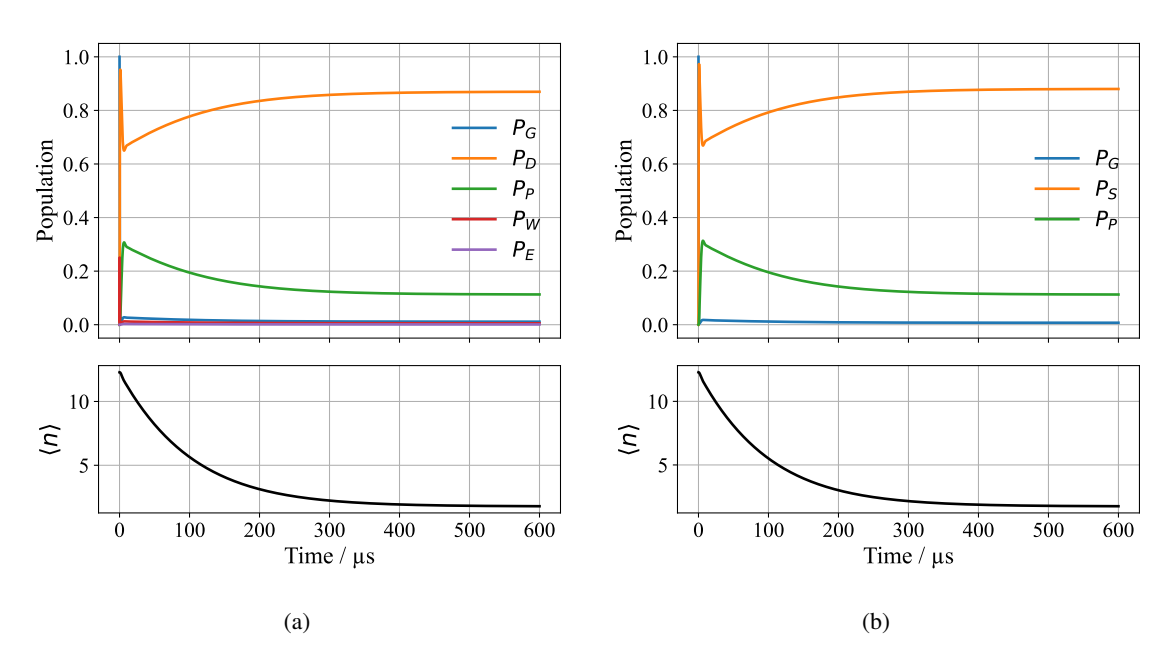


Figure 3.10: (a) shows the time evolution of expectation values of the atomic state population for the 5-level superatom system (upper plot). The lower plot shows the time evolution of the mean phonon number in the HBAR mode for the same simulation parameters. The mean phonon number decreases to a final value of  $\langle n \rangle \approx 1.78$ . As expected from the discussion in Section 3.2.3, the ground state population is significantly reduced compared to the single atom case in Fig. 3.5(a) as well as the population of the intermediate state  $|E\rangle$ . Because of the fast dephasing into the dark state  $|D\rangle$ , population in the bright state  $|W\rangle$  is negligible after short initial dynamics. The majority of the population is now in either  $|D\rangle$  or  $|P\rangle$ . (b) shows the time evolution of expectation values of the atomic state population for the simplified 3-level superatom system (upper plot) from Section 3.3.2. The lower plot shows the time evolution of the mean phonon number in the HBAR mode for the same simulation parameters.

The coupling of the resonator to the bright state is neglected as the population in this state is negligible (as discussed in Section 3.3.1). The collapse operators of this system are given by the following expressions. Here, collapse operators related to the atomic states apply for each of the *N* superatoms:

$$\begin{split} L_{\gamma_{\text{pump}}} &= \sqrt{\gamma_{\text{pump}}} \, |S\rangle \, \langle G| & \text{pump: } |G\rangle \to |S\rangle \\ L_{\gamma_{nS}} &= \sqrt{\gamma_{nS}} \, |G\rangle \, \langle S| & \text{decay: } |S\rangle \to |G\rangle \\ L_{\gamma_{nP}} &= \sqrt{\gamma_{nP}} \, |G\rangle \, \langle P| & \text{decay: } |P\rangle \to |G\rangle \\ L_{\gamma_{P}} &= \sqrt{\gamma_{P}} \, |G\rangle \, \langle P| & \text{engineered decay: } |P\rangle \to |G\rangle \\ L_{\Gamma_{c}} &= \sqrt{\kappa \, (\langle n_{th} \rangle + 1)} \hat{a} & \text{cooling: } |n\rangle \to |n-1\rangle \text{ in HBAR mode} \\ L_{\Gamma_{b}} &= \sqrt{\kappa \, \langle n_{th} \rangle} \hat{a}^{\dagger} & \text{heating: } |n\rangle \to |n+1\rangle \text{ in HBAR mode} \end{split} \tag{3.22}$$

The master equation of this system can be written down analogously to Eq. (3.19) and simulated using QuTiP. Apart from the engineered decay rate  $\gamma_P$  and the pump rate  $\gamma_{pump}$ , all other parameters are the same as in Table 3.2.

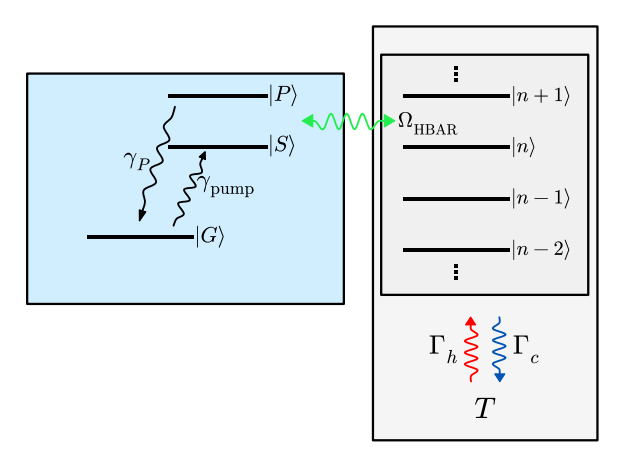


Figure 3.11: Simplified 3-level system for the superatom-HBAR cooling scheme. The collective ground state  $|G\rangle$  is pumped with rate  $\gamma_{\text{pump}}$  into the collective Rydberg state  $|S\rangle$ . The upper Rydberg state  $|P\rangle$  can decay with an engineered decay rate  $\gamma_P$  to the ground state. The two Rydberg states are coupled via the interaction with the HBAR mode with coupling strength  $\Omega_{\text{HBAR}}$ . The natural decay rates of the Rydberg states  $\gamma_{nS}$  and  $\gamma_{nP}$  are also included but not shown in the level scheme.

#### Results

For the moment, we assume a pump rate of  $\gamma_{\text{pump}}/2\pi=1$  MHz. First, we look at the time evolution of the atomic system and the resonator. Fig. 3.10(b) shows the time evolution of the expectation values of the atomic state population and the mean phonon number in the HBAR mode for a single superatom, using the optimized engineered decay rate of  $\gamma_P$ , which will be discussed later. We can compare this to Fig. 3.10(a) and indeed find the same dynamics as for the more complex 5-level atomic system. The mean phonon number decreases from the initial thermal value of  $\langle n \rangle \approx 14$  to a final value of  $\langle n \rangle \approx 1.74$ .

Having checked that we can reproduce the dynamics and cooling performance from Section 3.3.1, we can now look at the dependence of the system parameters that we can tune. As in the last section, we will first look at the dependence of the final mean phonon number on the engineered decay rate  $\gamma_P$  of the upper Rydberg state. Fig. 3.12(a) shows the mean phonon number in the HBAR mode in the steady state in dependence of  $\gamma_P$  and the number of superatoms N. Similarly to Fig. 3.9, there is an optimum for  $\gamma_P$  where the mean phonon number is minimized. Reducing the decay rate below the optimum also leads to a steep increase of the phonon number because the energy can not be extracted fast enough from the resonator before it is transferred back. Increasing the rate also increases the phonon number because of broadening of the upper Rydberg state, but less steep. Furthermore, increasing the number of superatoms shifts the position of the optimal decay rate to smaller values and decreases the minimum mean phonon number. For N=1, the optimal decay rate is  $\gamma_P/2\pi=54\,\mathrm{kHz}$  with a minimum mean phonon number of  $\langle n \rangle \approx 1.74$ . For N=3, the optimal decay rate is  $\sim 40\,\mathrm{kHz}$  with a minimum mean phonon number of  $\langle n \rangle \approx 0.5$ . This can be explained by the dependence of the coupling strength between atom and resonator on the phonon number. The Rabi frequency is given by

$$\Omega_{\text{HBAR},n} = \sqrt{n+1} \,\Omega_{\text{HBAR}} \,. \tag{3.23}$$

Here,  $\Omega_{\text{HBAR}}$  is the single-phonon Rabi frequency, n is the phonon number in the resonator, and  $\Omega_{\text{HBAR},n}$ 

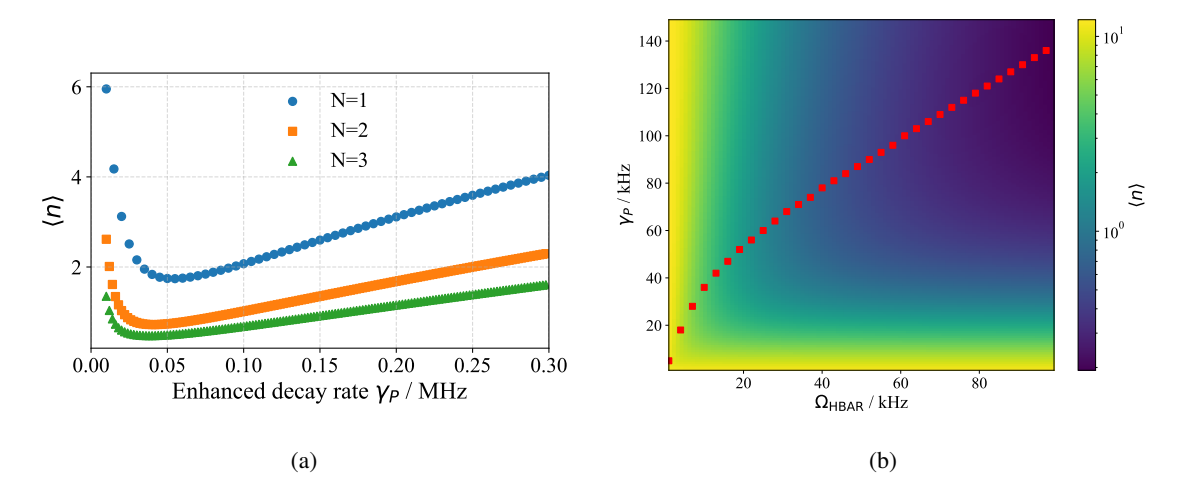


Figure 3.12: (a) shows the mean phonon number  $\langle n \rangle$  in the HBAR mode in the steady state in dependence of the engineered decay rate  $\gamma_P$  of the upper Rydberg state for different numbers of superatoms N. The pump rate is set to  $\gamma_{\text{pump}}/2\pi=1$  MHz. The other simulation parameters are the same as in Table 3.2. Increasing the number of superatoms leads to a decrease of the mean phonon number and the optimal engineered decay rate. The mean phonon number is very sensitive to changes in the engineered decay rates smaller than the optimum as we enter the strong coupling regime in this case. For larger decay rates, the phonon number increases as well because of the broadening, but less steep. (b) shows a heatmap of the mean phonon number in dependence of  $\gamma_P$  and the single-phonon Rabi frequency  $\Omega_{\text{HBAR}}$ . The number of superatoms is set to N=1, all other simulation parameters are kept the same. Increasing the coupling strength leads to a decrease in the mean phonon number. The red squares mark the optimal decay rate given a fixed atom-resonator coupling.

is the Rabi frequency for the transition between states with n and n+1 phonons. For a larger coupling, a larger optimal decay rate is needed to extract the energy before it is transferred back to the resonator. We can now imagine adding another superatom to the cooling process. Since the phonon number inside the resonator is already reduced compared to the thermal equilibrium, the coupling strength between the resonator and the atom is smaller. Therefore, a smaller decay rate is needed to extract the energy before it is transferred back. This explains why the optimal decay rate shifts to smaller values when increasing the number of superatoms. However, since the optimal decay value shifts to lower values for more atoms, there is no significant increase in cooling performance between the optimal decay rate for N=3 instead for N=1. The phonon number distribution for N=1 and N=3 is shown in Fig. 3.13. For N=1, there is a visible deviation of the final state from a thermal distribution with the same mean phonon number. For N=3, the deviation is less visible.

In addition to using more superatoms, we can also increase the coupling strength  $\Omega_{\rm HBAR}$  between the atoms and the resonator to increase the cooling performance. Fig. 3.12(b) shows a heatmap of the final mean phonon number in dependence of  $\gamma_P$  and  $\Omega_{\rm HBAR}$  for N=1. The mean phonon number decreases for increasing coupling strength as expected. The optimal decay rate also shifts to larger values for increasing coupling strength. For  $\Omega_{\rm HBAR}$ , there is a linear dependence between the coupling strength and the optimal decay rate. However, for now we will stick to the coupling strength of  $\Omega_{\rm HBAR}=20\,{\rm kHz}$  that was calculated in Section 3.1.2.

The next parameter of interest in the pump rate  $\gamma_{\text{pump}}$ . Fig. 3.14 shows the mean phonon number in the HBAR mode in the steady state in dependence of the pump rate for N=1. As expected from the

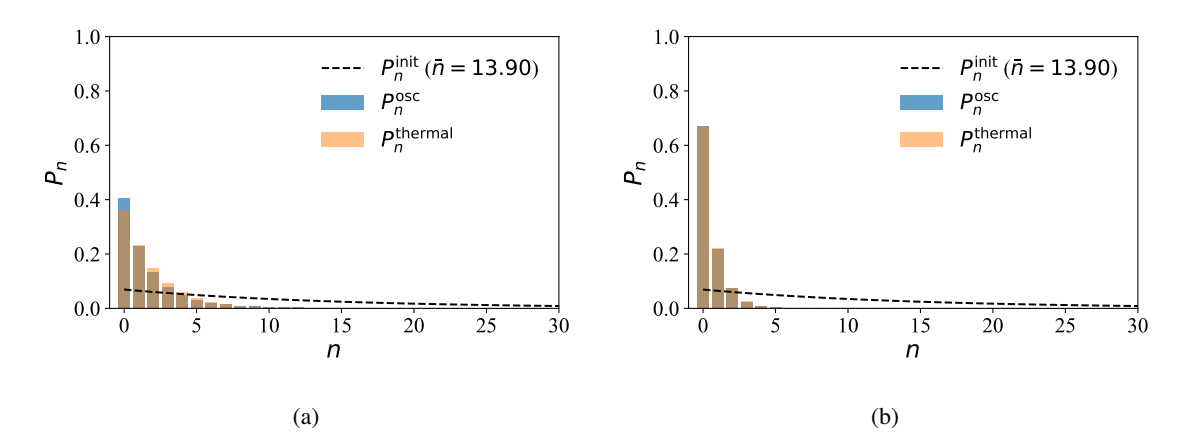


Figure 3.13: (a) shows the phonon number distribution after the cooling process with a single Superatom (N=1). The steady state solution with a mean phonon number of  $\langle n \rangle \approx 1.74$  is shown blue, the initial thermal distribution is marked by the dotted line. The thermal distribution with a mean phonon number of  $\langle n \rangle \approx 1.74$  is shown in orange for comparison. A deviation of the final state from the thermal distribution can be observed. (b) shows the same for N=3. Here, the mean phonon number in the steady state is  $\langle n \rangle \approx 0.5$ . The simulation parameters are the same as in Table 3.2 with  $\gamma_{\text{pump}}/2\pi=1\,\text{MHz}$  and  $\gamma_P/2\pi=54\,\text{kHz}$ .

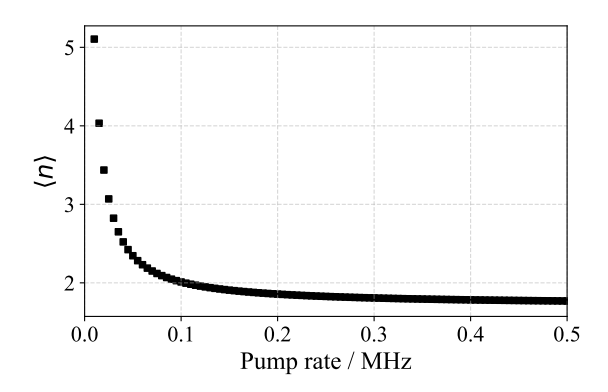


Figure 3.14: Mean phonon number  $\langle n \rangle$  in the HBAR mode in the steady state in dependence of the pump rate  $\gamma_{\text{pump}}$  for N=1. The engineered decay rate of the upper Rydberg state is set to  $\gamma_P/2\pi=54\,\text{kHz}$ . The other simulation parameters are the same as in Table 3.2. As expected from the discussion in Section 3.3.2, increasing the pump rate leads to a decrease in the mean phonon number. However, the phonon number saturates for large pump rates.

discussion in Section 3.2.3, increasing the pump rate leads to a decrease in the mean phonon number. However, the phonon number saturates for large pump rates. Increasing the pump rate from 0.5 MHz to 1 MHz only decreases the mean phonon number from  $\langle n \rangle \approx 1.77$  to  $\langle n \rangle \approx 1.74$ , meaning a reduction of about 2%. This is the case because we are in a regime where the pump rate is not the limiting factor as the coupling strength is much weaker than the pump rate. For smaller pump rates, comparable to the coupling strength, Fig. 3.14 shows a steeper increase of the mean phonon number with decreased pump rate. A case where having a higher pump rate becomes intereting again is for larger decay rates  $\gamma_{nS}$  of the lower Rydberg state. Here, the pump rate needs to compensate to keep the population in the lower Rydberg state, the cooling reservoir, high.

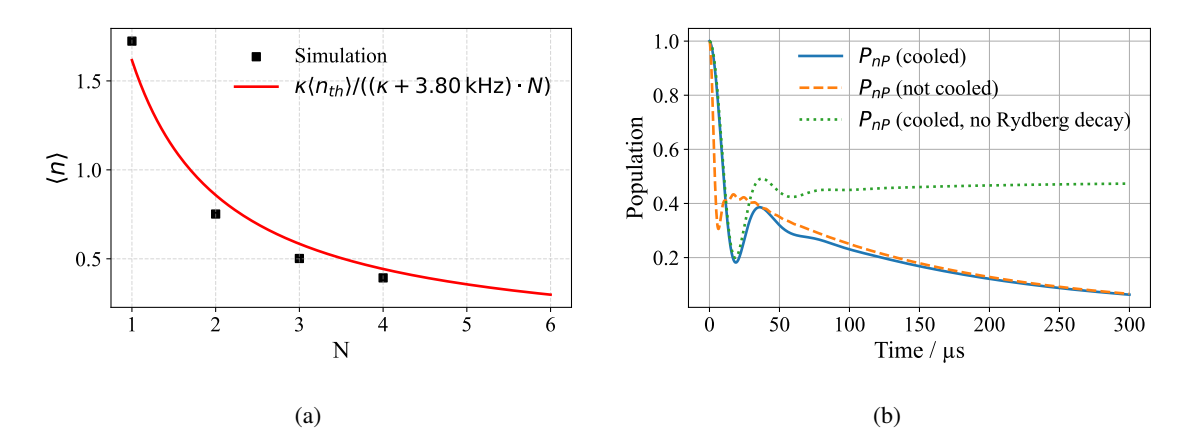


Figure 3.15: (a) shows the mean phonon number  $\langle n \rangle$  in the HBAR mode in the steady state in dependence of the number of superatoms N. The engineered decay rate of the upper Rydberg state is set to  $\gamma_P/2\pi = 54$  kHz. The pump rate is set to  $\gamma_{pump}/2\pi = 1$  MHz. The other simulation parameters are the same as in Table 3.2. The red line shows a fit according to Eq. (3.24) with  $\Gamma_{dis}$  as the only free parameter. (b) shows the time evolution of the expectation value of the population of the upper Rydberg state  $|P\rangle$  for a cooled (blue) and a non-cooled (orange) resonator. The green dashed line shows the time evolution of the population of the upper Rydberg state without Rydberg decay.

In Fig. 3.12(a), we already looked at the expected phonon number inside the resonator for different numbers of superatoms N. In the following, the dependence of the cooling on the number of atoms will be discussed in more detail. Fig. 3.15(a) shows the mean phonon number in the steady state in dependence of the number of superatoms N. The engineered decay rate is set to the optimal value for N=1 of  $\gamma_P=54$  kHz. The mean phonon number decreases with increasing number of superatoms. With the choosen parameters, four atoms are already enough to reach a mean phonon number below 0.5. There is no direct analytical expression for the dependence of the mean phonon number on the number of atoms because of the indirect dependence of the dissipation rate on the resonator occupation, as discussed in Section 3.2.1. However, we derived Eq. (3.13) from rate equations, where we calculated the resonator occupation after the cooling under the assumption of an independent dissipation rate. The occupation is given by

$$\langle n \rangle_{\text{eq}} = \frac{\langle n_{\text{th}} \rangle \kappa}{\kappa + N \cdot \Gamma_{\text{dis}}} \,.$$
 (3.24)

As a first approximation, we can fit this resonator occupation to the simulation result. We fix the values of  $\kappa$  and  $n_{th}$  to the values used for the qutip simulation, and leave  $\Gamma_{dis}$  as the only free parameter for the fit. The fit is shown as the red line in Fig. 3.15(a). One can see that there is an overestimation of the cooling performance in case of a single atom and an underestimation for larger numbers of atoms (a better fit would be obtained when omitting N=1). This can be understood by the fact that the assumption of a phonon number independent dissipation rate becomes a better assumption for a less wide phonon number distribution. A narrower distribution is achieved when more superatoms contribute to the cooling scheme. To conclude, Eq. (3.24) gives a good first estimate for the scaling with superatom number.

The next step would be to study the coherent interaction between the Rydberg atoms and the HBAR, by measuring rabi oscillations between the two Rydberg states as this two-level system exchanges excitations with the HBAR. Fig. 3.15(b) shows the time evolution of the expectation value of the population of the

upper Rydberg state  $|P\rangle$  for a cooled and a non-cooled resonator. One can see that the cooled oscillator allows longer coherent dynamics. Two oscillations are visible before they are completely damped out. For the non-cooled resonator, this is not the case. The reduction of population over time comes from the decay of the Rydberg states which can be seen by looking at the green dashed line in Fig. 3.15(b) which shows the time evolution of the population of the upper Rydberg state without Rydberg decay. One thing to notice here is that the amount of Rabi oscillations is fundamentally limited by

$$\frac{\Omega_{\text{HBAR}}}{\kappa \cdot \langle n_{\text{th}} \rangle},$$
 (3.25)

because the heating rate out of the ground state is given by  $\kappa \cdot \langle n_{\rm th} \rangle$ . This means that being able to cool the resonator and observing coherent interactions are two separate things. A good cooling scheme can already work with lower coupling strengths but a large amount of superatoms participating in the cooling process. To observe coherent dynamics, a large coupling strength and a low heating rate are needed.

#### **Outlook: Time-Dependent Engineered Decay Rate**

As discussed in the last Section, the optimal decay rate of the upper Rydberg state depends on the coupling strength between Rydberg atoms and the resonator and also the phonon number inside the resonator through  $\Omega_{\text{HBAR},n} = \sqrt{n+1}\,\Omega_{\text{HBAR}}$ . At the moment, the decay rate is kept constant throughout the cooling process. However, from the phonon number dependency, it becomes clear that there should be an optimal decay rate for each point in time during the cooling process. Therefore, it might be intersting to check if a time dependent decay rate could enhance the cooling performance. An idea would be to start with a large decay rate to quickly extract energy from the resonator and then lower the decay rate as the phonon number inside the resonator reduces. As a proof of concept, the decay rate could be decreased lineary to see if the cooling performance is enhanced.

#### **Outlook: Measuring the HBAR Temperature**

Until now, it is not clear how to actually measure the success of the cooling process. One possible idea is to measure the Rydberg state population in nS and nP. In Fig. 3.10(b), we looked at the time evolution of the expectation values of the atomic state population and the HBAR phonon occupation. It becomes clear that there is a strong correlation between the ratio of nS to nP population and the HBAR population. This might be used to infer the phonon number occupation in the HBAR from the atomic population. However, this needs to be analyzed quantitatively. In the experiment, a value which is proportional to the population in nS and nP could be measured via state selective ionization and detection.

### 3.4 Experimental Implementation

Throughout the discussion of the simulation, we did not specify the states involved in the cooling scheme in much detail. Fig. 3.16 shows a possible combination of levels in rubidium-87 that allows realization of the scheme. The ground state atoms are coupled to the lower  $|nS\rangle$  Rydberg state via the probe and control laser at 780 nm and 480 nm, respectively. The lasers are detuned from the intermediate  $|5P_{3/2}\rangle$  state such that they drive the two photon transition with an effective driving strength  $\Omega$ . The  $|nS\rangle$  state is coupled to the  $|nP\rangle$  state via the interaction with the HBAR mode m. The interaction strength is

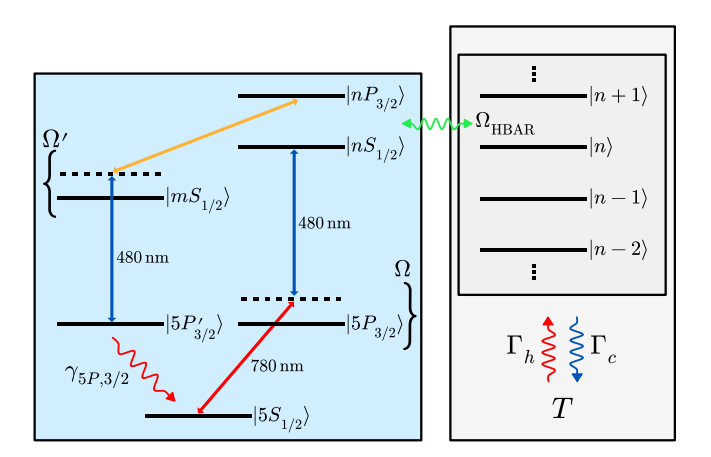


Figure 3.16: Possible experimental implementation of the cooling scheme. The ground state atoms are coupled to the lower Rydberg state via a two–photon transition with effective Rabi frequency  $\Omega$ . The lower Rydberg state is coupled to the upper Rydberg state via the interaction with the HBAR mode with strength  $\Omega_{HBAR}$ . The upper Rydberg state is coupled to an intermediate state via a two–photon transition with effective Rabi frequency  $\Omega'$ . The intermediate state decays fast with rate  $\gamma_{5P,3/2}$ , which introduces the desired dissipation channel.

characterized by  $\Omega_{\rm HBAR}$  and is controlled by the distance between atoms and resonator surface. Now we would like to introduce a dissipation channel for the extracted energy. One idea would be to couple the upper Rydberg state to a different hyperfine level of the  $|5P_{3/2}\rangle$  state which then decays fast with a decay rate of  $\gamma_{5P,3/2}/2\pi \sim 6$  MHz [97]. Since the direct coupling is dipole-forbidden, one could introduce an external microwave driving field that couples the  $|nP\rangle$  state to a nearby  $|mS\rangle$  Rydberg state. The  $|mS\rangle$  state can then be coupled to the  $|5P_{3/2}\rangle$  state via a second 480 nm laser, which is already part of the experimental setup. By detuning the laser and the microwave driving field from the intermediate  $|mS\rangle$  state, this process also happens via a two-photon transition with effective driving strength  $\Omega'$  (in general we are not limited to the  $|5P_{3/2}\rangle$  state, it is only a convenient option as the laser needed for that is already available).

# **Atom Chip Characterization**

The HQO experiment is built with the purpose of interfacing Rydberg atoms with an electromechanical oscillator. In the last two chapters, we discussed the properties of the oscillator and how it can couple to the Rydberg atoms. A necessary prerequisite for this is the ability to trap atoms close to the resonator surface. This will be achieved with an on-chip magnetic trap that is generated by a current carrying wire on the atom chip. However, the atom trapping is not the only requirement to perform successful experiments. Another key requirement is the ability to detect the Rydberg atoms after the interaction with the resonator. As the planned setup with the electromechanical oscillator is in itself already a challenging experiment that has not been demonstrated before, it is crucial to have a well-established detection scheme for the Rydberg atoms. For this, we plan to use a coplanar waveguide (CPW) resonator on a first-generation atom chip without the electromechanical oscillator that can be used to drive the specified Rydberg-Rydberg transition. The chip has been fabricated and should allow testing and establishing the Rydberg excitation and detection scheme independently of the coupling to the electromechanical oscillator.

To determine whether the chip is ready for use in the planned experiment, we will test its two core functions in this Chapter: the CPW resonator and the magnetic confinement via the trapping wire. Since both parts derive from specific design choices, a brief overview of the chip layout is provided to clarify their intended roles in more detail before discussing the characterization. After this, we begin by characterizing two versions of the resonators, where the second version was designed to correct the frequency mismatch observed in the first. Using cryogenic transmission measurements, we extract resonance frequencies, quality factors, and their temperature dependence, and compare the results to theoretical expectations. In the second part, we measure the critical current of different types of trapping wires, both on a test chip and on the experiment chip, in order to test their suitability for generating the required magnetic trapping fields.

## 4.1 Overview of Atom Chip Design

The first-generation atom chip was designed by Leon Sadowski in his Master thesis [62] and fabricated by the Forschungszentrum Jülich. An image of the fabricated chip is shown in Fig. 4.1. The chip includes a superconducting niobium trapping wire which can, in combination with an external magnetic bias field, form a magnetic trap for the atoms above the chip. The exact position can be controlled via the current

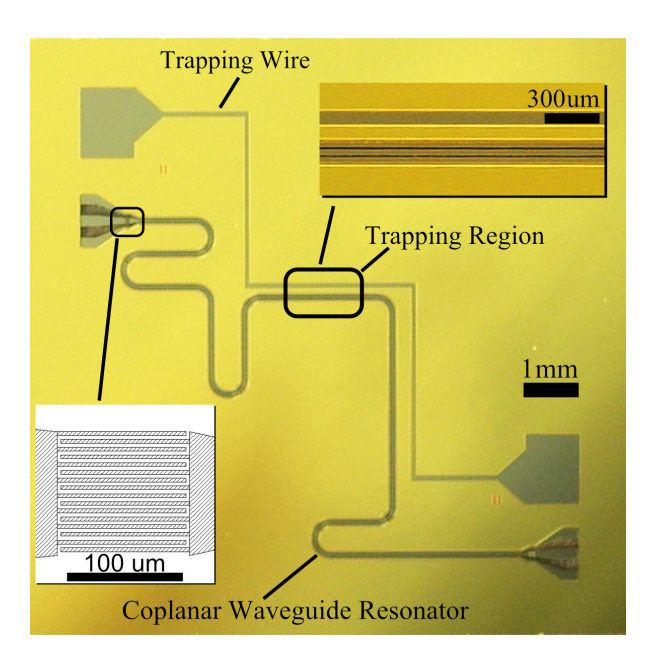


Figure 4.1: Image of the atom chip that includes a superconducting niobium trapping wire and a superconducting niobium coplanar waveguide resonator. The chip is fabricated on a c-cut Sapphire substrate and covered with a 500 nm thick gold layer that is grounded. The left inset shows a zoom-in into the finger capacitors that couple the resonator to the feedlines. The top right inset shows a zoom-in into the trapping region. For this chip, the bondpads for the trapping wire were increased in size compared to the first design from Ref [62]. Reasons for that will be discussed in Section 4.3.5.

that runs through the wire and the external bias field. The wire is chosen to be superconducting which means that below a critical temperature  $T_c$  and critical current  $I_c$ , the wire has zero resistance [103]. The reason for it is to avoid any heating close to the atoms (for more details, the reader is referred to Ref [62]).

Furthermore, the chip features a superconducting niobium CPW resonator to couple to the Rydberg atoms. The resonator is coupled to the feedlines via finger gap capacitors that are shown in the inset on the left in Fig. 4.1. The top right inset shows a zoom-in into the trapping region. For the experiment, it is planned to use the second harmonic mode of the resonator to couple to the Rydberg atoms. This is because the fundamental mode has a node of the electric field at the position of the atoms, which would result in no coupling. The second harmonic has an antinode at this position, which maximizes the coupling strength [62]. Apart from the superconducting niobium structures, the chip is covered with a 500 nm thick gold layer that will be grounded which should help to shield the atoms from stray electric fields from the substrate [104].

In the experiment, the chip is soldered onto a sample holder made out of copper. Flexible PCBs (printed circuit boards) are attached to the copper sample holder and wirebonded to the chip using Aluminium wire bonds. Flexible PCBs are used to safe space inside the cryogenic region.

## 4.2 Coplanar Waveguide Resonator Characterization

The section about the resonator characterization is structured in the following way: First, the theory about CPW resonators that is needed to understand subsequent measurements is discussed. After this,

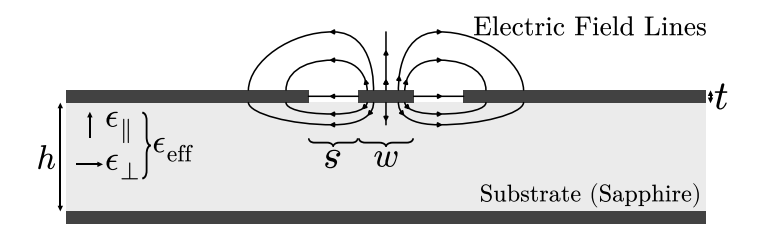


Figure 4.2: Cross-section of a coplanar waveguide. It consists of three conductors on top of a substrate. The outer two are grounded while the central conductor carries the signal. The bottom conductor is grounded as well. The waveguide is characterized by the width w of the central conductor, the gap s, the thickness t of the conductors and the relative permittivity of the substrate which is given by  $\epsilon_{\text{eff}}$  for an isotropic material. For Sapphire, the permittivity parallel to the surface is different to the permittivity orthogonal to it. Consequences of this will be discussed later in Section 4.2.1. Qualitative electric field lines are shown with black arrow lines.

the measurement method is presented, followed by the measured resonator transmission spectra. Finally, we will discuss and interpret the results and arrive at implications for the next chip design.

#### 4.2.1 Dependence of Resonance Frequency on System Parameters

In this section, only those properties of CPW resonators are summarized that are required to later interpret the temperature-dependent resonance measurements. For details beyond that, the reader is referred to the literature [62, 87, 105]. The main objective is to arrive at a compact expression for the resonance frequency that incorporates all relevant system parameters. The central result of this section is Eq. (4.9), which provides an explicit expression for the resonance frequency.

An illustration of a coplanar waveguide is shown in Fig. 4.2. It consists of a center conductor separated by gaps from two ground planes on either side. The ground and central conductors are fabricated on a substrate. By fabricating a trace of such a CPW that is open at both ends, a resonator can be formed. The resonance frequency  $\omega_n$  of the mode n can be tuned by changing the length of the trace and the dielectric properties of the substrate. By adding capacitive couplings at both ends, the resonator can be coupled to feedlines to drive it externally. Around the resonance, the coupled resonator can be well described by an LCR circuit [87], which is capacitively coupled to the feedlines. This is shown in Fig. 4.3. As the resonator is made out of superconducting niobium, the resistance R is set to zero from now on. The resonance frequency can then be expressed as [87]:

$$\omega_n = \frac{1}{\sqrt{L_n(T)(C + 2C_\kappa)}},$$
(4.1)

where  $L_n(T)$  is the temperature dependent inductance of the resonator at mode n, C is the capacitance of the resonator and  $C_{\kappa}$  is the coupling capacitance at each end. For Eq. (4.1) to hold, it is assumed that the coupling capacitance  $C_{\kappa}$  is much smaller than the resonator capacitance C [87]. The inductance  $L_n$  and the capacitance C can be expressed in terms of the inductance per unit length  $L_I(T)$ , the capacitance

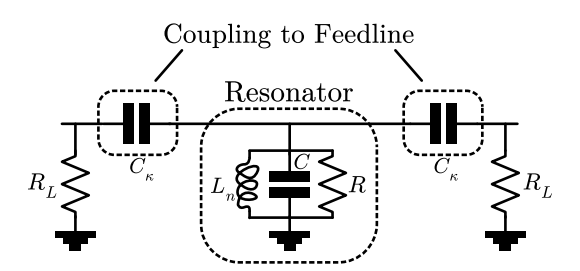


Figure 4.3: Circuit representation of a CPW resonator that is capacitively coupled to feedlines at both ends. Around the resonance, the resonator can be described as an LCR circuit with an inductance  $L_n$ , a capacitance C and a resistance R. The coupling capacitors at both ends are represented by  $C_K$ . Adapted from Ref [87].

per unit length  $C_l$ , the length of the resonator l and the mode number n as [87]:

$$L_n = \frac{2L_l(T)l}{n^2\pi^2}$$
 (4.2)

$$C = \frac{C_l l}{2} \ . \tag{4.3}$$

The inductance per unit length  $L_l(T)$  can be composed of two parts [106]:

$$L_l = L_l^g + L_l^k(T) . (4.4)$$

Here,  $L_l^g$  is the geometric inductance per unit length and  $L_l^k(T)$  is the kinetic inductance per unit length. The geometric inductance and capacitance per unit length can be calculated via conformal mapping techniques [105]. For this, calculation tools are available online [107]. Important parameters that influence  $L_l^g$  and  $C_l$  are the width of the center conductor w, the width of the gaps s and the relative permittivity  $\epsilon_r$  of the substrate.

The kinetic inductance is a property of importance for superconducting resonators [108] and arises from the kinetic energy of the charge carriers [106]. For the current design, the kinetic inductance can be expressed as [109]

$$L_l^k(T) = \frac{\mu_0 \lambda(T)}{w} q(d/\lambda(T)) g_{\epsilon}(w/b, \epsilon) , \qquad (4.5)$$

under the assumption that  $w \gg \lambda^2/t$ , where t is the thickness of the superconducting film,  $\lambda$  is the penetration depth and w is the central trace width. Here,  $g_{\epsilon}(w/(s+w), \epsilon)$  is a geometric factor that is of order unity [109] and q(x) is a function that depends on the thickness of the superconducting film and the penetration depth. The function q(x) is given by [109]:

$$q(x) = \frac{\sinh(x) + x}{8\sinh(x/2)^2} \,. \tag{4.6}$$

The penetration depth determines how deep magnetic fields can penetrate into the superconductor. It is

temperature dependent [103] and can be expressed with

$$\lambda(T) = \frac{\lambda(0)}{\sqrt{1 - \left(\frac{T}{T_c}\right)^4}} \ . \tag{4.7}$$

The penetration depth at zero temperature  $\lambda(0)$  and the critical temperature  $T_c$  are material properties of the superconductor. For our resonator, we expect  $\lambda(0) \sim 100\,\mathrm{nm}$  [62] and  $T_c = 9.2\,\mathrm{K}$  [62]. As a result, the kinetic inductance increases with temperature and diverges when approaching the critical temperature  $T_c$ . This results in a decrease of the resonance frequency with increasing temperature. This feature is commonly used to tune the resonance frequency of superconducting resonators [104, 110]. Furthermore, it allows to clearly identify the resonance of a superconducting resonator from the background spectrum when measuring the transmission spectrum at different temperatures. Combining Eqs. (4.5) to (4.7) allows expressing the kinetic inductance explicitly in dependence of the temperature. Furthermore, combining Eqs. (4.1) to (4.4) allows writing down the expected resonance frequency of the n-th mode of the resonator as

$$\omega_n(T) = \frac{n\pi}{l} \frac{1}{\sqrt{C_l \left(L_l^g + l_l^k(T)\right) \left(1 + \frac{4C_\kappa}{C_l l}\right)}}$$
(4.8)

For our design, we expect to have  $L_l^g \gg L_l^k$  and  $C_l l \gg C_{\kappa}$  [62]. Therefore, we can expand the resonance frequency to first order in  $L_l^k/L_l^g$  and  $C_{\kappa}/(C_l l)$  to obtain:

$$\omega_n(T) \approx \frac{n\pi}{l\sqrt{L_l^g C_l}} \left( 1 - \frac{L_l^k(T)}{2L_l^g} - \frac{2C_{\kappa}}{C_l l} \right) . \tag{4.9}$$

It shows that for zero kinetic inductance and zero coupling capacitance, the bare resonance frequency is recovered. However, the kinetic inductance and the coupling capacitance both reduce the resonance frequency linearly to first order.

#### **Effective Dielectric Constant of Substrate**

Before we can use Eq. (4.9) and apply it to the measurements, we have to discuss the properties of the dielectric substrate of the CPW resonator. The substrate of our chip is made out of c-cut Sapphire. Sapphire is an anisotropic material with two different values for the relative permittivity, one along the c-axis ( $\epsilon_r^{\parallel}=11.5$ ) and one orthogonal to it ( $\epsilon_r^{\perp}=9.4$ ) [111]. As illustradted in Fig. 4.2, the electric field lines start and end at the conducting planes of the CPW, and sample both directions of the permittivity. Therefore, we need to calculate an effective permittivity  $\epsilon_{\rm eff}$  that takes this into account. According to Ref [105], one can transform the substrate into an insotropic one with an effective isotropic permittivity that can be expressed as:

$$\epsilon_{\text{eff}} = \sqrt{\epsilon_r^{\parallel} \cdot \epsilon_r^{\perp}} = 10.4 \ .$$
 (4.10)

This allows us now to calculate values for the capacitance per unit length  $C_l$  using Ref [107].

#### 4.2.2 Designed Resonator Versions

Based on the resonance model introduced above, the CPW resonators were initially designed using only the geometric contributions to the inductance and capacitance. Specifically, the target frequency was calculated from

$$\omega_n = \frac{n\pi}{l\sqrt{L_l^g C_l}} \,, \tag{4.11}$$

where the kinetic inductance  $L_l^k$  was neglected under the assumption that it would be small compared to the geometric contribution  $L_l^g$  [62]. The coupling capacitance  $C_{\kappa}$  was likewise omitted, not because it was expected to be negligible, but because its exact value could not be reliably estimated at the design stage [62]. Furthermore, the sapphire substrate was treated as isotropic with a relative permittivity of  $\epsilon_r = 11.5$  [62], rather than using the effective permittivity  $\epsilon_{\rm eff}$  introduced in Section 4.2.1. Two versions of resonators were produced, with the key design differences and the corresponding measurement outcomes, which will be analysed in the next Section, summarized in Table 4.2:

- **Version 1** was designed to match the atomic transition at 5.818 GHz using the second harmonic of the resonator, under the assumption of negligible kinetic inductance and coupling capacitance.
- **Version 2** retained the same geometry and layout but featured an increased resonator length. The modification served two purposes: (i) to compensate the frequency deviation observed in the first measurement, and (ii) to detune the resonance by -80 MHz on purpose to be able to account for possible quadratic Stark shift of the Rydberg transition in the experiment.

The parameters assumed during the design, as well as those extracted from later measurements and model fits, are summarized in Table 4.1. These values provide the reference for interpreting the measurement data presented in the following Sections. The deviations observed in the first-version measurements motivated the design modifications implemented in the second version. In the next Sections, the characterization measurements of both resonator versions will be discussed in detail.

Table 4.1: Expected CPW resonator parameters that determine the resonance frequencies.  $^{\dagger}$  marked values are inferred from fitting Eq. (4.9) to the fundamental mode resonance frequency of the second version resonator, \* marked values were used in the previous calculation of resonance frequencies [62], \* marked values were expected values [62]. The capacitance per unit length is changed by the effective relative permittivity of the substrate ( $\epsilon_{\text{eff}} = 10.4$ ) compared to the previously used value of  $\epsilon = 11.5$ . Geometry dimensions of the waveguide are given in Ref [62].

Symbol	Description	Updated Value (this work)	Value Used in Design	Unit
$L_l^{ m g}$	Geometric inductance per unit length	$4.295 \times 10^{-7}$	$4.295 \times 10^{-7}$	${\rm Hm}^{-1}$
$L_l^{\mathrm{k}}$	Kinetic inductance per unit length	$^{\dagger}6.461 \times 10^{-9}$	*0 *1.050 × 10 <sup>-9</sup>	${\rm Hm}^{-1}$
$\overline{C_l}$	Capacitance per unit length	$1.479 \times 10^{-10}$	$1.634 \times 10^{-10}$	$Fm^{-1}$
$\overline{C_{\kappa}}$	Coupling capacitance	$^{\dagger}55.0 \times 10^{-15}$	*0 *56.4 × 10 <sup>-15</sup>	F

Table 4.2: Comparison of first and second version CPW resonator designs. The second version was designed to correct the frequency mismatch observed in the first. The trapping wire bond pads were also enlarged to facilitate wire bonding. An additional design change was the introduction of a 20 µm gap between the CPW center conductor and the gold layer. The detuning of -80 MHz in the second version was chosen to account for possible quadratic DC-Stark shifts of the Rydberg atoms close to the atom chip by adsorbate fields.

Parameter	Version 1	Version 2
Design Intent	Match 5.818 GHz (2nd har-	Detuned by -80 MHz (2nd har-
	monic)	monic)
Target atomic transition	$85S_{1/2} \leftrightarrow 85P_{3/2}$	Same
Designed target resonance	5.818 GHz	~5.74 GHz
Geometric Design		
Resonator length	20.449 mm	21.222 mm
Coupling capacitor design	2 × 8 finger capacitors	Same
Substrate	c-cut sapphire	Same
Measurement Outcome		
Measured resonance (1st harmonic @4K)	-	2.83 GHz
Extracted Q-factor (1st harmonic @4K)	-	~ 200
Measured resonance (2nd harmonic @4K)	Ambiguous ~ 5.955 GHz	5.66 GHz
Extracted Q-factor (2nd harmonic @4K)	Not reliable	~ 100 (expected)
Trapping Wire		
Bond Pads	$200 \times 700 \mu m$	$800 \times 1300 \mu m$
Additional change:		Added 20 µm gap between CPW center conductor and gold layer

#### 4.2.3 Measurement Method

The transmission measurements were performed by collaborators at the Forschungszentrum Jülich. As shown in Fig. 4.4, the chip was mounted on our sample holder which was then mounted into their dilution refrigerator sample holder. The flexible PCBs were wirebonded to the chip. The flex PCBs were interfaced with coaxial lines leading to a vector network analyzer (VNA). The input signal was attenuated by approximately 70 dB before the chip, while the output signal was amplified by a cryogenic HEMT amplifier (gain  $\sim 40$  dB) followed by room-temperature amplification of  $\sim 40$  dB. Since the absolute gain of the full setup is not precisely known, the recorded  $|S_{21}|$  transmission spectra (input voltage / output voltage) are reported in arbitrary units.

The transmission around the expected resonance frequencies of the first and second harmonic was recorded repeatedly while slowly warming the setup from the base temperature of a few millikelvin up to the niobium critical temperature of  $9.2\,\mathrm{K}$ . For both chips, the measurements were performed with an input power of  $-10\,\mathrm{dBm}$  from the VNA.

#### 4.2.4 Measured Resonance Spectra

In the following, the measured resonance spectra of both resonator versions will be presented and discussed.

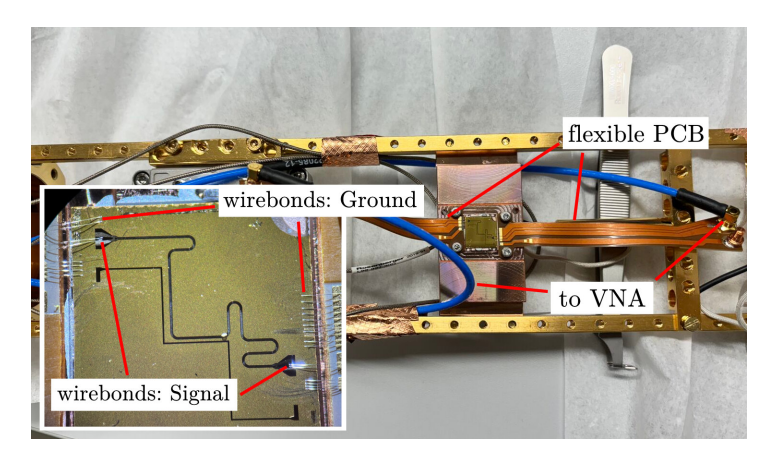


Figure 4.4: First version of chip mounted in the sample holder of the Forschungszentrum Jülich. The chip is wirebonded to flexible PCBs that are connected to coaxial lines leading to a vector network analyzer (VNA). The inset on the left shows a zoom-in into the chip where the wirebonds to the signal trace of the CPW and ground are visible. Image courtesy of Roudy Hanna, FZ Juelich.

#### **First Version**

A zoom into the region of interest around the expected resonance frequency of the second harmonic mode is shown in Fig. 4.5. A lot of different peak structures can be seen in the spectrum which can stem from various signal reflections in the setup (cables, connectors, attenuators, amplifiers, flexible PCBs, wirebonds, ...). Around the expected position of the resonance frequency, there is no clear peak visible. However, at higher frequencies (> 5.87 GHz), there are multiple overlaped peaks while one of them at 5.955 GHz at 4 K is cleary larger than the rest. One can see that at 7 K, the spectrum vanishes in the noise floor. This behaviour is unexpected as the theoretical critical temperature of niobium is around 9.2 K which should allow seeing a visible spectrum beyond 7 K. The reason for this is not known. One feature that was used as an indication that the 5.955 GHz peak might be the resonator resonance was that the amplitude of this peak decreases faster with temperature than the rest of the spectrum. It looks like there is a slight change in frequency with temperature, however, this can also be a result from the decrease in peak amplitude relative to the amplitude of the peak to the left. Under the assumption that this is indeed the resonator resonance, we can extract a deviation of about 140 MHz from the target frequency. As the source of this possible deviation could not be identified from this one measurement, it was decided to measure a second version of the chip with an adapted resonator length to account for the frequency shift.

#### **Second Version**

The second version of the atom chip was designed with a slightly larger resonator length to account for the frequency shift that was observed in the first version. The new target frequency was chosen to lie about 80 MHz below the target frequency of the first version. This choice was made to account for possible DC-Stark shifts of the Rydberg atoms close to the atom chip by adsorbate fields. The chosen  $85S_{1/2} \leftrightarrow 85P_{3/2}$  transition shifts due to the quadratic Stark effect only to lower frequencies. Under the assumption of a linear change in resonance frequency with the total resonator length, the new resonator

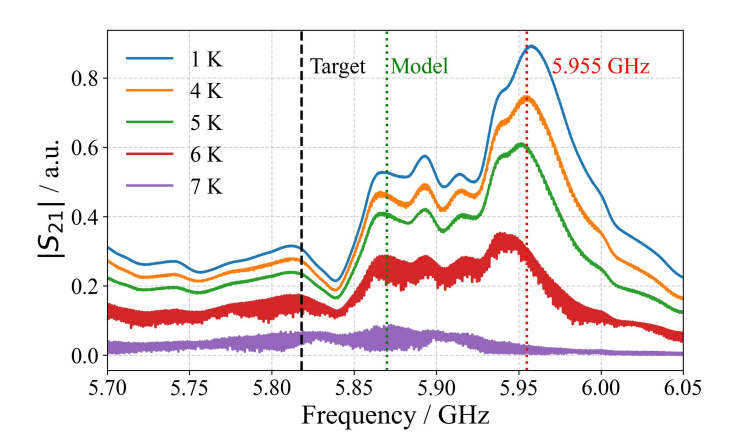


Figure 4.5: Transmission  $|S_{21}|$  of first chip. The spectrum is shown for different temperatures between 1 K and 7 K. The target frequency of 5.818 GHz is shown in black. The resonance frequency of the identified resonator resonance at 4 K is shown in red. The green dotted line represents the expected resonance frequency using Eq. (4.9) and the new values from Table 4.1.

length was chosen to be

$$l_2 = 20.449 \,\text{mm} \cdot \frac{5.955 \,\text{GHz}}{5.818 \,\text{GHz} - 80 \,\text{MHz}} = 21.222 \,\text{mm} \ .$$
 (4.12)

Here, 20.449 mm is the length of the first resonator version.

For this resonator, the same measurement was carried out by the Forschungszentrum Jülich as for the first version. The temperature dependent transmission spectrum around the target frequency for the first and second harmonic mode is shown in Figs. 4.6 and 4.7. Different to the previous measurement, for both modes, a clear temperature dependent resonance is visible which is expected from the temperature dependent kinetic inductance. This, plus the fact that the position of the higher resonance is exactly a multiple of the lower resonance, is a very strong indication that these two resonances are indeed the first two modes of the CPW resonator. Furthermore, Figs. 4.6 and 4.7 also show a fit of Eq. (4.9) to the data. Results from this will be discussed in the next Section. Extracted resonance frequencies at 4 K are  $\omega_{n=1}/2\pi = 2.83$  GHz and  $\omega_{n=2}/2\pi = 5.66$  GHz. For the fundamental mode, the quality factor can be extracted by fitting a Lorentzian function to the resonance peak at 4 K as shown in Fig. 4.8. We obtain a quality factor of  $Q \approx 200$  and a resulting linewidth of  $\delta\omega/2\pi \approx 15$  MHz at 4 K.

As one can see in Fig. 4.7, there is still a deviation of about 80 MHz from the target frequency left (for the second harmonic). In the following, we will analyze the measured data in more detail to understand the unknown resonator parameters and the frequency deviation.

#### 4.2.5 Extraction of Resonator Parameters from Measurement Data

With Eq. (4.9), the resonance frequency and its temperature dependence was established in Section 4.2.1. We now apply it to the measured spectra in order to extract the previously unknown circuit parameters and to assess to what extent the observed frequency shifts can be quantitatively understood with Eq. (4.9).

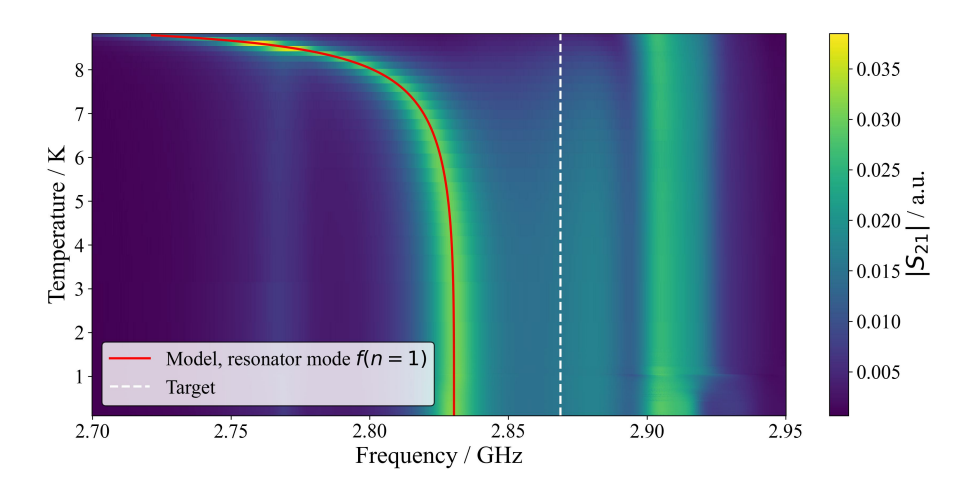


Figure 4.6:  $|S_{21}|$  transmission spectrum around the identified n=1 resonance in dependence of the temperature. The white line represents the target frequency. The red curve represent a fit of Eq. (4.9) using the coupling capacitance and kinetic inductance as free parameters. Extracted values are given in the main text. The strong temperature dependence arises from the temperature dependence of the kinetic inductance close to the critical temperature of 9.2 K.

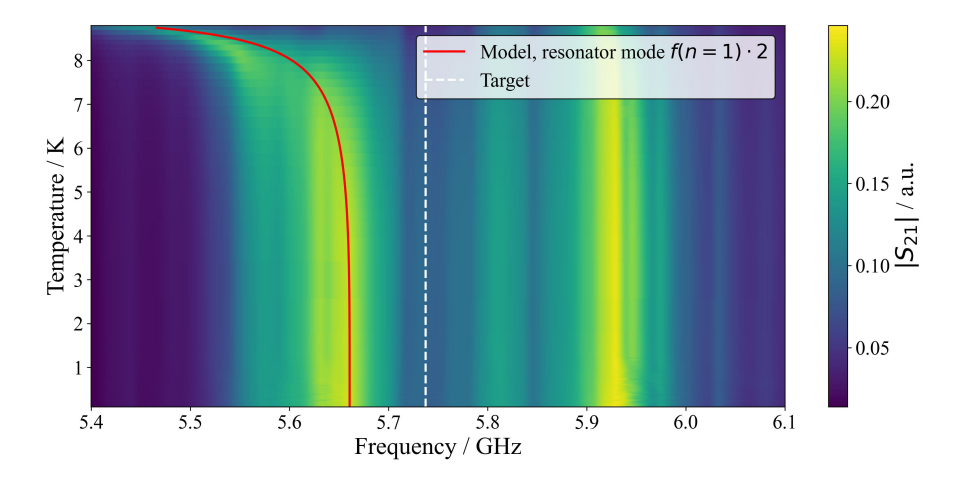


Figure 4.7:  $|S_{21}|$  transmission spectrum around the identified n=2 resonance in dependence of the temperature. The white line represents the target frequency. The red curve represents the fitted model from Fig. 4.6. The extracted frequency is multiplied by two (second harmonic) according to Eq. (4.9). The strong temperature dependence arises from the temperature dependence of the kinetic inductance close to the critical temperature of 9.2 K. Background structures of unknown source interfer with the resonator resonance in the region around 5.6 GHz.

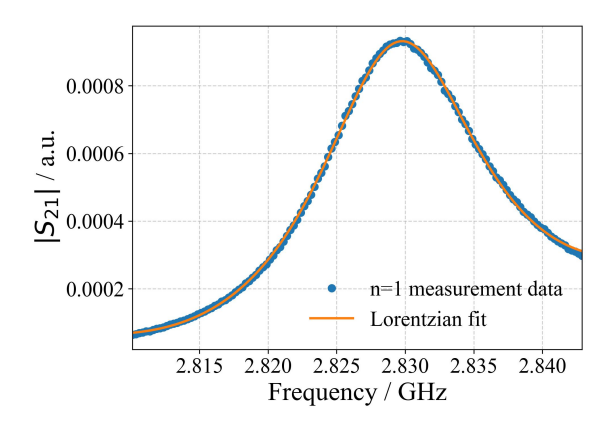


Figure 4.8: Zoom into the measured transmission spectrum around the resonance frequency of the first mode of the CPW resonator at 4 K. The data is fitted with a Lorentzian function and a quadratic background. We obtain a quality factor of  $Q \approx 200$  and a resulting linewidth of  $\delta \omega/2\pi \approx 15$  MHz at 4 K. The resonance frequency is determined to be  $\omega_{n=1}/2\pi = 2.83$  GHz. The quality factor can not be determined more precisely due to other background structures to the right (not visible in zoom-in) in the spectrum which influences the results depending on the frequency range that is used for the fit.

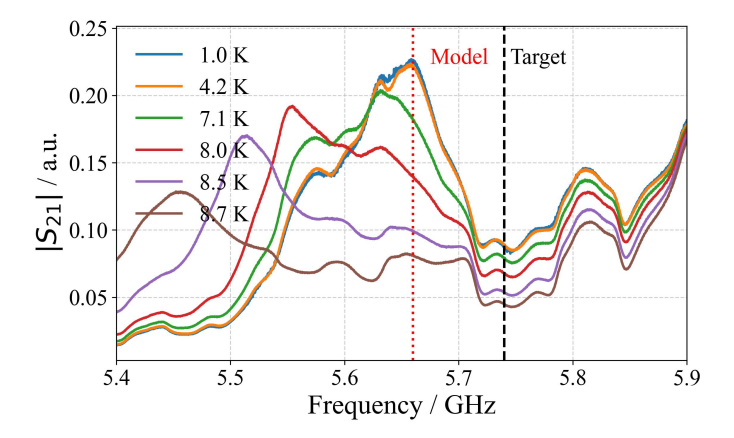


Figure 4.9:  $|S_{21}|$  transmission spectrum around the identified n=2 resonance at different resonator temperatures. A shift of a resonance peak with increasing temperature can be observed. The black dashed line indicates the originally targeted resonance frequency at 4 K. The red dotted line represents the predicted resonance frequency at 4 K which is obtained by multiplying the extracted resonance frequency of the first mode by a factor of two.

#### Fit of Temperature-Dependent Resonance

Having the change in effective permittivty to the effective value of  $\epsilon_{\rm eff}=10.4$  and the temperature dependent behavior in Eq. (4.9) now established, there are two parameters that are not precisely known: The coupling capacitance  $C_{\kappa}$  and the kinetic inductance per unit length  $L_l^k(0\,\mathrm{K})$ . Using the values from Table 4.1 and using  $C_{\kappa}$  and  $L_l^k(0\,\mathrm{K})$  (expressed through the penetration depth  $\lambda(0)$ ) as free parameters, we can fit Eq. (4.9) to the measured temperature dependent resonance frequency of the first mode of the second version of the resonator. This is shown in Fig. 4.6. From the fit, we can extract a coupling capacitance of  $C_{\kappa}=55\,\mathrm{pF}$  and a kinetic inductance per unit length of  $L_l^k(0\,\mathrm{K})=6.48\times10^{-9}\,\mathrm{H\,m^{-1}}$ . The coupling capacitance is in good agreement with the design value of  $56.4\,\mathrm{pF}$  from Ref [87]. The kinetic inductance per unit length is about six times larger than the expected value of  $1.05\times10^{-9}\,\mathrm{H\,m^{-1}}$  from Table 4.1 but still in the same order of magnitude. This could be explained by a larger penetration depth  $\lambda(0)$  than the assumed 100 nm.

Using the obtained values for  $C_{\kappa}$ ,  $L_l^k(0\,\mathrm{K})$  and Eq. (4.9), we can plot the expected temperature dependent resonance frequency of the second harmonic of the second version. This is shown in Fig. 4.7. It visually agrees well with the measured data This can be seen more cleary for the expected resonance at 4 K, which is shown in Fig. 4.9. One has to note that there are multiple background peak structures which distorts the temperature dependent curve.

The model explains the measured second resonator very well, but it is still unclear how much it helps to understand the first version. If we take the extracted parameters ( $C_{\kappa}$ ,  $L_l^k$  and  $\epsilon_{\rm eff}$ ) and apply them to the geometry of the first resonator, we expect a shift of  $\sim -80$  MHz from the 5.955 GHz peak. It is shown in Fig. 4.5 as the dashed "Model"-line. The shift is noticeably smaller than  $\sim -140$  MHz shift from the originally intendified target transition. However, it is not certain that this peak was trully the resonator mode. The spectrum in Fig. 4.5 contains many overlapping features, and without an unambiguous temperature dependence it is difficult to identify the correct one.

#### **Extracted Linewidth and Quality Factor**

The resonator was intentionally designed to operate in the overcoupled regime, i.e. with an external coupling much stronger than internal losses ( $Q_{\rm ext} \gg Q_{\rm int}$ ). In this regime, the total quality factor is dominated by the external coupling and is therefore tunable via the coupling capacitance. The total quality factor is given by [87]

$$\frac{1}{Q} = \frac{1}{Q_{\text{int}}} + \frac{1}{Q_{\text{ext}}},$$
 (4.13)

so that for  $Q_{\rm ext}\gg Q_{\rm int}$  one finds  $Q\approx Q_{\rm ext}$ . This design choice is intentional as a lower quality factor yields a broader resonance linewidth,  $\delta\omega=\omega_n/Q$ . This relaxes the requirement for precise frequency matching between the resonator and the atomic transition.

In Section 4.2.4, a quality factor of  $Q \approx 200$  was extracted for the fundamental mode of the resonator (second version), corresponding to a linewidth of  $\delta\omega/2\pi\approx 15\,\mathrm{MHz}$  at a resonance frequency of  $\omega_{n=1}/2\pi=2.83\,\mathrm{GHz}$ . To check consistency, it can be compared to the expected external quality factor. In the overcoupled limit, where  $Q \simeq Q_{\mathrm{ext}}$ , one may use [87]

$$Q_{\simeq} \frac{C_l l}{4\omega_{n,0} R_L C_{\nu}^2} . \tag{4.14}$$

Table 4.3: Comparison between the originally designed resonance frequency ("Designed"), the experimentally measured value ("Measured"), and the now fully modelled contributions from changed effective permittivity, kinetic inductance, and coupling capacitance ("Current Model") for the second harmonic resonance of the second version resonator. Only the final frequency of 5.661 GHz is directly measured; all shifts are theoretically inferred. The designed final resonance was expected by the change of the resonator length compared to the measurement of the first version resonator, which is included in  $\Delta\omega_{\rm exp}$ 

Quantity	Designed	Measured	Current Model	Unit
Bare resonance and permittivity update				
Effective-permittivity shift $\Delta\omega_{\epsilon_{ m eff}}/2\pi$	_	_	0.288	GHz
Bare resonance $\omega_{0,n=2}/2\pi$ ( $L_l^k = 0, C_{\kappa} = 0$ )	5.625	_	5.913	GHz
Additional shifts				
Kinetic-inductance shift $\Delta\omega_{L_{l}^{k}}/2\pi$	_	_	-0.045	GHz
Coupling-capacitance shift $\Delta \omega_{C_u}/2\pi$	_	_	-0.207	GHz
Infered from first chip measurement $\Delta\omega_{\rm exp}/2\pi$	0.113	_	_	GHz
Final resonance $\omega_{n=2}/2\pi$	5.738	5.661	5.661	GHz

Here,  $R_L$  is the impedance of the feedline (typically 50,  $\Omega$ ), and  $\omega_{n,0}$  is the bare resonance frequency. Inserting  $C_{\kappa}=55\,\mathrm{pF}$  and  $R_L=50\,\Omega$  gives  $Q_{\mathrm{ext}}\approx280$ , reasonably close to the measured  $Q\approx200$ . The remaining discrepancy can be explained by deviations in the actual feedline impedance (e.g. due to wirebond or flex-PCB impedance mismatch), a slightly larger coupling capacitance, or additional unknown internal losses. For the second harmonic, the quality factor is expected to be half the value of the fundamental mode, i.e.  $Q_{n=2}\approx100$ , since the external quality factor scales inversely with frequency (see Eq. (4.14)). This agrees reasonably well with the intention of  $Q_{n=2}^{\mathrm{design}}\approx180$  [62].

#### **Decomposition of Frequency Shifts**

From Section 4.2.1, we have three different sources that shift the expected resonance frequency systematically: The shift  $\Delta\omega_{\epsilon_{\rm eff}}$  by the reduced effective permittivity  $\epsilon_{\rm eff}$ , the shift  $\Delta\omega_{L_l^k}$  by the kinetic inductance and the shift  $\Delta\omega_{C_\kappa}$  by the coupling capacitance. They are summarized in Table 4.3. This shows us that there are systematic shifts in total of about 500 MHz (when summing up all absolute values) allthough the total shift of the resonance frequency between the expected resonance frequency and the modelled frequency is only about 80 MHz (for the second harmonic of the second version). This is a result of the fact that the two largest systematic shifts (coupling capacitance and reduced substrate permittivity) shift in opposite directions.

The analysis shows that substrate anisotropy, kinetic inductance, and external coupling all have a noticeable impact on the resonance frequency. With these effects now quantified, they can be taken into account more quantitatively in future designs.

#### Implications for Future Resonator Design

To conclude the discussion, the measured resonance frequency in dependence of the temperature for the second chip can be well described by Eq. (4.9) when including a coupling capacitance and a kinetic

inductance per unit length as free parameters and correcting the effective permittivity of the substrate. The extracted coupling capacitance is in good agreement with the design value while the kinetic inductance per unit length is about six times larger than the initial estimate.

In future designs, these three systematic contributions can now be taken into account. Further measurerements will help to check the consistency of the results. Ideally, at least one chip with the same design parameters should be measured to check that there are no fabrication related variations and one with a different resonator length to check the predictions of the model. As an example, one could try to target the atomic transition at  $5.818\,\text{GHz}$  again with the second harmonic of the resonator. Using the extracted parameters from Table 4.1 and Eq. (4.9), this would require a resonator length of  $l=20.635\,\text{mm}$ .

Furthermore, it might be of interest to indentify the sources of background peaks in the transmission spectra. Especially for the second version, there were multiple overlapping peak structures around the second harmonic resonator resonance which might interfer with the resonace. Here, one could first measure the transmission spectra without a chip, just the cables that go to the VNA connected with each other, to check what peaks originate from sources inside the measurement setup and not the chip. Secondly, a chip with a normal waveguide instead of a resonator could be measured to check what peaks are directly related to the chip (e.g. reflection at impedance mismatched places like the wirebonds).

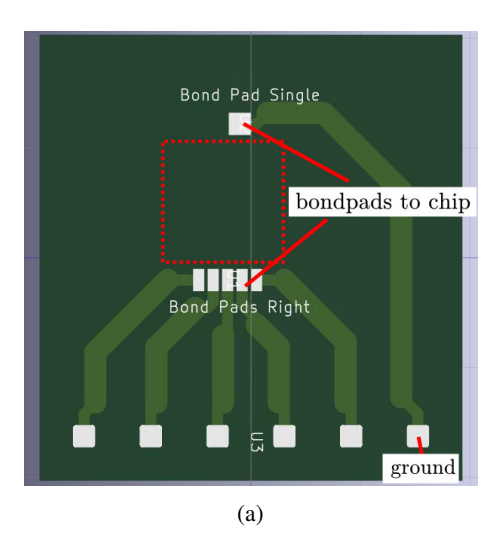
### 4.3 Trapping Wire Characterization

The operation of the atom chip depends on the trapping wire carrying the required currents to generate the trapping fields while remaining in the superconducting state. To test this for the current design and to obtain reference values for future layouts, critical current measurements of niobium z-shaped trapping wires were carried out at liquid helium temperature (4 K). The aims were: (i) to check whether the trapping wire of the gold-coated experiment chip reaches the expected current and to measure the available safety margin, (ii) to measure the current-carrying capacity of niobium wires of different widths on a dedicated test chip for future chips with different traps, and (iii) to identify possible design limitations, e.g. regarding the connections to the feedlines via wirebonds.

#### **Measurement Strategy**

For the measurements, the gold coated experiment chip and the test chip, shown in Fig. 4.11, are glued on custom PCBs and operated in a liquid helium dewar. This provides a straightforward way to reach 4 K without the need of a cryostat [112], while also allowing for high current of up to 10 A which is required for larger trapping wires on the test chip. For the measurement, a sensing and protection circuit is designed and tested to detect the superconducting-to-normal transition. It should be able to resolve small resistance jumps of  $\sim 10\,\mathrm{m}\Omega$  expected in the gold-coated chip (resistance jumps in the multi-z-wire test chip are expected to be larger), and to switch off the transport current quickly in order to avoid damaging the chip by overheating.

The measurements were carried out together with Cedric Wind in the laboratory of the Linden group. In the following, the chip mounting and PCB design is described in Section 4.3.1. Section 4.3.3 discusses the sensing and protection circuit which meets the technical requirements described in Section 4.3.2. Section 4.3.4 provides details about the measurement procedure while the results and implications are discussed in Section 4.3.5.



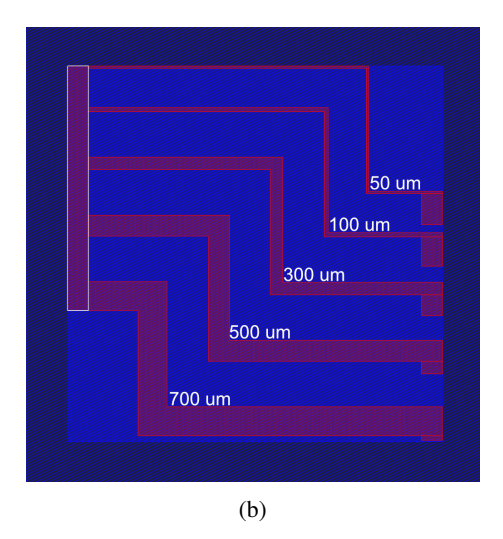


Figure 4.10: (a) shows a PCB design for the critical current measurements (Image taken from KiCad software). The PCB has a dimension of 38 mm x 40 mm and has space in the middle for an 11 mm x 11 mm chip (marked with red dotted square). Five traces plus ground are routed to the edge of the chip position with pads for wirebonding. (b) shows the lithography mask of the test chip with five superconducting niobium *z*-wires (red) of different widths (widths are written at each wire). All blue areas are bare substrate.

#### 4.3.1 Chip Mounting and PCB Design

The mounting of the two chips on custom PCBs are described in the following.

#### **PCB Layout and Design Choices**

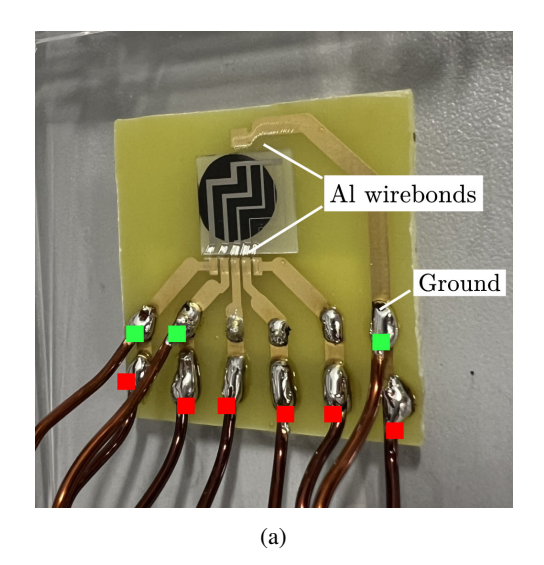
A printed circuit board (PCB), shown in Fig. 4.10(a), was designed to mount the chips such that they fit into the helium dewar through a *KF 50* flange with all cables routed from the same side. The design allows using it with the experiment chip and the test chip as we will see later. The area where a chip should be placed in marked in red in Fig. 4.10(a). The PCB allows for five different connections to a chip with a common ground for all of them. The chip itself will be electrically connected to the PCB via Aluminium wirebonds, the connection pads on the circuit board are therefore designed such that multiple wirebonds can fit on one pad.

#### Interfacing Chips with PCB

Both chips were glued onto the PCB using two-component epoxy (Stycast 2850FT epoxy with Catalyst 9) as shown in Fig. 4.11. Aluminium wirebonds of 25  $\mu$ m diameter were attached from the PCB bondpads to the chip bondpads. The wirebonding was performed by Max Wegerhoff from the Linden group. The maximally achievable number of wirebonds per pad were used to reduce heating from the bond resistance as much as possible.

#### **Test Chip**

To measure the critical current of z-wire traps of different widths, a test chip was designed. It includes five different z-wire traps. It is not coated with gold because it is not required for this application



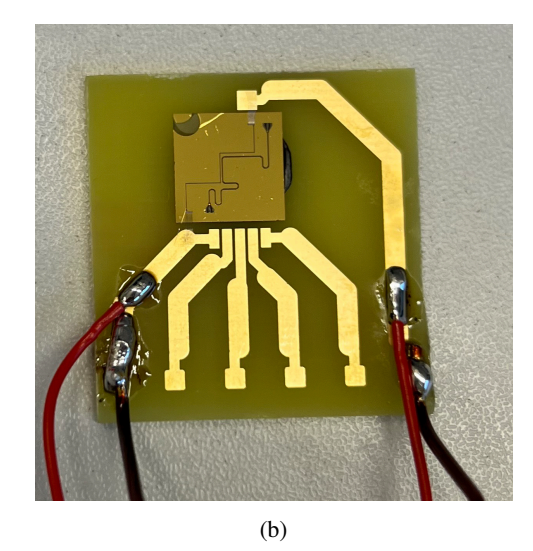


Figure 4.11: (a) shows the critical current test chip with five superconducting trapping wires of different width. The chip is glued using a two component epoxy onto the PCB. The wires are connected to the PCB with multiple wirebonds. Feed lines for measurement are soldered onto the PCB (current carrying wires are marked red), extra feedlines on ground and the two outer wires are for four point measurements (marked green). (b) shows the same setup with a real gold coated experiment chip. The trapping wire is wirebonded to the PCB. Two extra feedlines are connected for a four point measurement (red cables).

and reduces the number of required lithography steps. The lithography mask of this chip is shown in Fig. 4.10(b). The test chip was fabricated by the Forschungszentrum Jülich. Fig. 4.11(a) shows the test chip glued and wirebonded onto the PCB. Copper wires are soldered onto the PCB. Six of them are current carrying wires (5 different z-wires and ground). Additional copper wires for the two outer z-wires are soldered to be able to perform four-point measurements, which is a technique for low resistance sensing [112]. The copper wires can then be connected to a feed through that can be plugged on top of the helium dewar (see Fig. 4.15). In the following, this chip will be called "test-chip".

#### **Gold Coated Experiment Chip**

A gold coated experiment chip, described previously in Section 4.1, was glued and wirebonded onto the PCB, shown in Fig. 4.11(b). Here, two copper wires that carry the current are soldered onto the PCB. Two additional wires (later replaced by the same copper wires) are used for four-point measurements to be able to detect small resistance jumps in the order of  $\sim 10\,\mathrm{m}\Omega$ . In the following, this chip will be called "experiment-chip".

#### 4.3.2 Measurement Requirements and Estimates

To be able to measure the critical current, we have two main requirements. First, we need to be able to detect the expected resistance jump when the current exceeds the critical current  $I_c$ . Above this current, the superconductor transitions to the normal state. Second, we need to protect the wire from damage by melting [112] when exceeding  $I_c$  by switching off the current supply quickly.

To calculate the expected resistance of the trapping wire above the critical current, we make a simple

Table 4.4: Measured and expected resistances of niobium wires on the test chip at room temperature and expected resistances at 4 K.

Width / μm	Measured $R_{300K}$ / $\Omega$	Expected $R_{300K}$ / $\Omega$	Expected $R_{4K}$ / $\Omega$
50	$103.00 \pm 2.00$	70	3.5
100	$49.00 \pm 1.00$	35	1.7
300	$16.10 \pm 0.60$	12	0.6
500	$9.60 \pm 0.50$	7	0.4
700	$7.60 \pm 0.50$	5	0.3

estimation. We imagine our z-shaped trapping wire to be one long wire with a rectangular cross-section. In this case the resistance can be calculated with:

$$R = \rho \frac{l}{A} \ . \tag{4.15}$$

Here,  $\rho$  is the resistivity of the material, l is the length of the wire, and A is the cross-sectional area. The trapping wires on the chip have a thickness of 500 nm and a total length (ignoring the turns and the bond pads) of 11.6 mm. To calculate the resistivity, we start of with the value for bulk niobium at room temperature of  $\rho_{300K} \approx 0.15 \,\Omega$  mm<sup>2</sup> m<sup>-1</sup> [113]. This allow to calculate the expected resitances of the z-wires at room temperature, given in Table 4.4. The measured resistances at room temperature of the test chip are included in Table 4.4 as well and give the right order of magnitude compared to the estimation, higher measured values can be attributed to a higher resistivity in the sputtered niobium films compared to the bulk.

However, at liquid helium temperature, the resistivity is lower. We assume a residual-resistivity ratio (RRR =  $\frac{\rho_{300K}}{\rho_{10K}}$ ) of 20 [114], leading to the expected values in Table 4.4. Here one has to note that the value for the RRR depends on the quality of the sputtered film and can be smaller than 20 (between 9 and 21 in Ref [115]) which would relax the required measurement sensitivity. From the expected resistance values at 4 K above the critical current, we infer a required sensitivity in the order of  $\sim 100 \, \text{m}\Omega$ .

For the gold chip, the situation is different. At the moment the supercoductivity of the niobium wire breaks, the current can run through the gold film instead of the wire. The gold film is expected to have a much smaller resistance than the wire itself. We can make a very simple estimation of this resistance to get an idea of the order of magnitude we need to be able to detect where we assume contact resistance to be negligible. Assuming a resistivity of gold of  $\rho_{300K} \sim 2.4 \times 10^{-8} \,\Omega$  m [113] and an RRR of 10 (exact value depends also on the quality of the sputtered gold film [116]), we can calculate the sheet resistance  $R_S$  given a gold layer thickness of  $d=500\,\mathrm{nm}$  to be  $R_S=\frac{\rho_{300K}}{RRR\cdot d}\sim 5\,\mathrm{m}\Omega$ . Assuming a path length of  $l=11.6\,\mathrm{mm}$  and a free gold layer to the left and right of the niobium wire of width  $w=1\,\mathrm{mm}$  (which is already an overestimation because of the cpw resonator on one side of the trapping wire), we get an estimation for the resistance of the new current flow path through the gold layer of  $R_{\mathrm{Au}}=R_S\frac{l}{2w}\sim 30\,\mathrm{m}\Omega$ . From this, we conclude that we would like to be able to detect resistance jumps in the order of  $10\,\mathrm{m}\Omega$ .

#### 4.3.3 Sensing and Protection Circuit

In the last Section, we discussed the requirements for the sensing and protection circuit. The main goals are to detect the superconducting-to-normal transition, measure  $I_c$ , resolve small resistance jumps of  $10 \,\mathrm{m}\Omega$ , and switch off the transport current quickly to avoid damage from heating. In the following, the

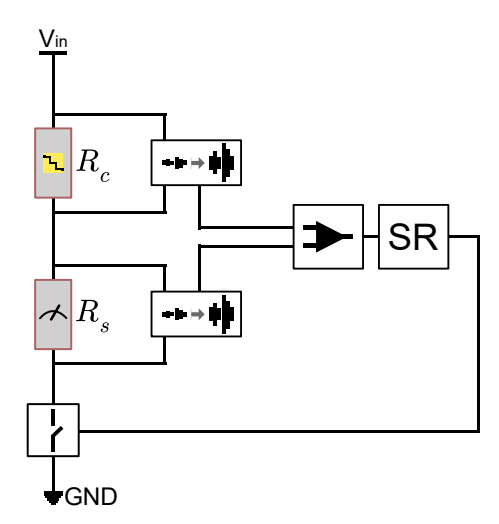


Figure 4.12: Sensing and protection setup, based on Ref [112]. The differential voltage drop across the chip (if needed via four-point measurement for increased sensitivity) is amplified and compared via a comparator to the amplified voltage drop across a shunt resistor  $R_s$ . A set-reset latch shuts down the current supply permanently if the amplified chip voltage exceeds the amplified shunt voltage.

implemented design is discussed.

The design process was guided by a chapter about setting up a critical-current measurement system in [112]. Fig. 4.12 shows the implementation idea for our measurements. A shunt resistor  $R_s$  is used as a resistance reference to compare to the resistance of the chip  $R_c$ . Both resistances are measured by measuring and amplifying the differential voltage drop across both. Depending on the needed sensitivty, a four-terminal measurement is used to only measure the differential voltage drop across the chip and not the feedlines. The amplified signals are then compared with a comparator. A set-reset latch is used to trigger a switch that interrupts the current supply, when the chip signal exceeds the reference signal, permanently until reset.

To implement the setup from Fig. 4.12, a circuit was designed and simulated in LTSpice (shown in Fig. 4.13). In the following, we will go through the important parts. In the circuit, the reference resistance is named R3 (chosen to be  $0.1\,\Omega$ ), the chip resistance R11 and the feed line resistance R13. Two intrumentation amplifiers, consisting of three operational amplifiers each, are used to measure the differential voltage drop across the reference resistor and the chip. The instrumentation amplifier for the chip can be wired in two different configurations. In the first configuration (shown in blue), a four-terminal measurement is performed by connecting the inputs to the four-terminal feedlines (higher sensitivity). In the second configuration (shown in red), a two-point measurement is performed by connecting the inputs to the two current-carrying feedlines (lower sensitivity). The amplification of both instrumentation amplifiers can be tuned with potentiometers R4 and R20 which is, in addition to having a high input impedance, the reason to for using an instrumentation amplifier instead of a simple differential amplifier.

The outputs of both amplifiers are fed into a comparator that outputs the negative rail voltage when the chip signal exceeds the reference signal and the positive rail voltage otherwise. A non-inverting Schmitt trigger is used to supply a low signal to the switching MOSFET when the input is negative, meaning the chip signal exceeds the reference signal. Once this state is reached, the output of the Schmitt-trigger

remains negative until reset. This is important to avoid oscillations of the MOSFET after the switching due to undefined comparator output.

The potentiometers of the instrumentation amplifiers were chosen to be  $100 \text{ k}\Omega$ . The amplification G of an instrumentation amplifier is given by [117]:

$$G = 1 + \frac{2R_8}{R_4} \,, \tag{4.16}$$

where  $R_4$  and  $R_8$  are in reference to Fig. 4.13. If we assume  $U_c$  and  $U_s$  to be the amplified differential voltage drops across the chip and the reference resistor, respectively, we can express the ratio as:

$$\frac{U_c}{U_s} = \frac{R_c}{R_s} \frac{G_c}{G_s} \,, \tag{4.17}$$

where  $R_c$  and  $R_s$  are the chip and reference resistances, respectively, and  $G_c$  and  $G_s$  are the gains of the chip and reference instrumentation amplifiers, respectively. Assuming the differential voltage increase across the chip to be  $R_c = 0.1R_s = 10\,\mathrm{m}\Omega$ , we can see that a detection of this resistance (and switching the MOSFFET), where  $U_c$  exceeds  $U_s$ , is no problem for  $G_c > 10G_s$ . The circuit is therefore suited for our application. However, it is important to note that the resistors used for the amplifiers are 1% tolerance resistors as we wanted to build a circuit from readily available components. Consequently, the circuit is not intended for high-accuracy current measurements, since the resistor tolerances lead to gain errors and poor common-mode rejection [117]. In our case, this is acceptable because the amplifiers are not used for precise current sensing, but only to detect the expected resistance steps of  $\leq 10\,\mathrm{m}\Omega$  and trigger the MOSFET switching. The actual current through the chip is measured independently using a current clamp.

The circuit was built on a perforated board and tested with a dummy load of  $0.1 \Omega$  to verify its functionality before using it in the actual measurement. The built board in shown in Fig. 4.14. The switching time  $\tau$  was measured to be  $\tau \le 20 \, \mu s$ , where the determination of  $\tau$  was limited by the bandwidth of the current clamp of 20 MHz [118]. This switching time is expected to be fast enough.

#### 4.3.4 Measurement Procedure

To perform the measurement, a power supply for the sensing circuit and a voltage controlled power supply for the current supply were set up with a common ground. The characterization was first conducted on the five-wire test chip. The connection wires were trimmed such that the PCB remained fully immersed in liquid helium without touching the bottom of the dewar. The wires were routed through an external feedthrough mounted on top of the dewar, as shown in Fig. 4.15. To reduce thermal stress and prevent detachment of the chip from the PCB during cooldown, the assembly was pre-cooled in liquid nitrogen before being gradually lowered into the helium bath. Superconductivity of the z-wires was verified by measuring the resistance between the feedthrough terminals using a standard multimeter. A reading of zero resistance confirmed that, as any residual resistance would have been detectable otherwise (see Table 4.4).

The sensing and protection circuit was connected to the feedlines of one trapping wire per measurement. Current was monitored using a current clamp on the supply lead. The signals from the instrumentation amplifiers were recorded via an oscilloscope to configure the amplifier gains such that the amplified voltage drop across the reference resistor slightly exceeded that across the superconducting chip. This

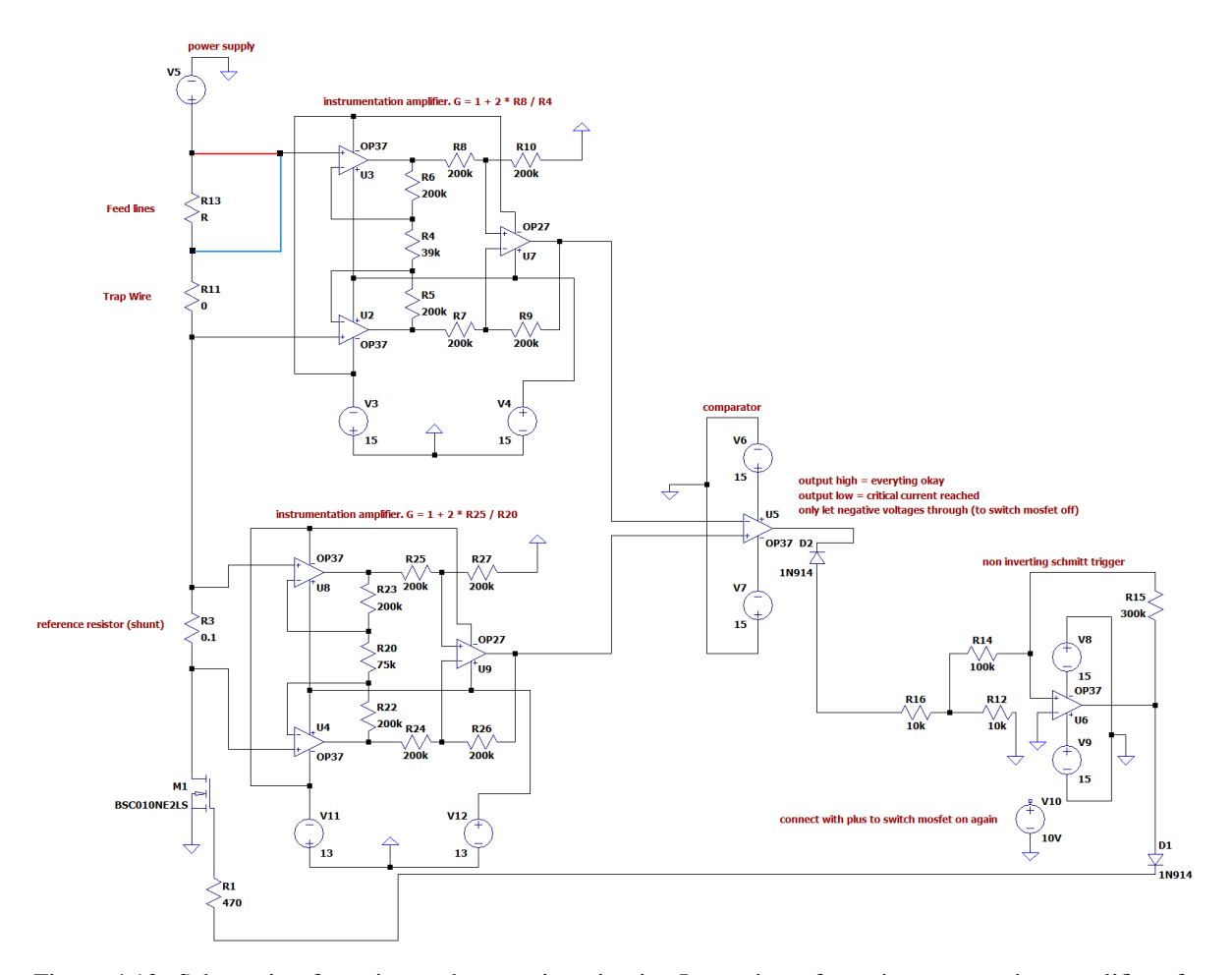


Figure 4.13: Schematic of sensing and protection circuit. It consists of two instrumentation amplifiers for differential voltage drop measurements across the chip and a sensing resistor, a comparator and Schmitt trigger for state detection and switching trigger and a MOSFET for fast on/off switching of current supply. More details are provided in the main text. The upper instrumentation amplifier is either wired to measure the voltage drop only across the trapping wire (four-terminal measurement, shown in blue) or across the entire chip + current feedlines (shown in red). Resistors R4 and R20 are tunable  $100 \,\mathrm{k}\Omega$  potentiometers to set the amplification factor.

ensured that after reaching the critical current  $I_c$ , the comparator triggers the MOSFET to switch off the current supply. The current at the trigger point is recorded as the critical current  $I_c$ . Multiple measurements were acquired for each wire.

The same procedure was applied to the experiment chip, with two adjustments. First, the expected resistance jump at  $I_c$  is much smaller (see Section 4.3.2). Consequently, the amplifier inputs were reconfigured for four-point sensing to increase sensitivity to small resistance jumps. Second, damage to the wire was not anticipated as the current can flow through the gold layer instead of the z-wire, after reaching  $I_c$ . The shunt resistance amplification was therefore increased such that no comparator triggering could happen, allowing uninterrupted recording of the full current-voltage trace.

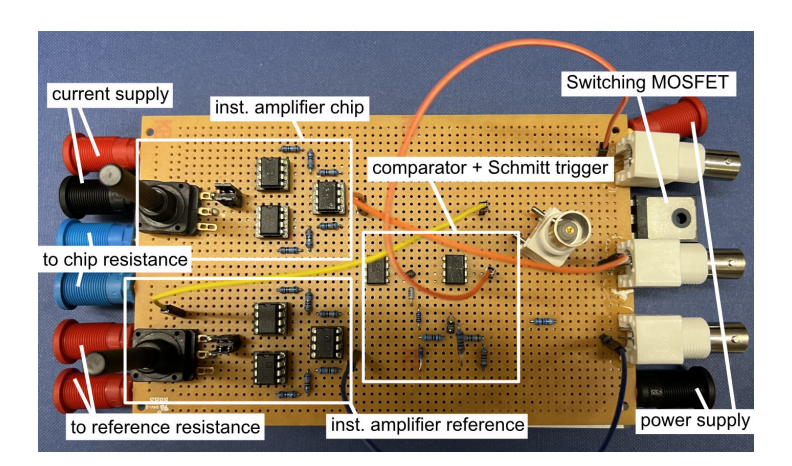


Figure 4.14: Picture of assembled sensing and protection circuit. Black knobs are the potentiometers that tune the amplification factors of the instrumentation amplifiers. The BNC outputs are used to monitor the following: both instrumentation amplifier output and the gate voltage of the MOSFET. For the reference resistor, 10 parallel 1  $\Omega$  resistors were used.

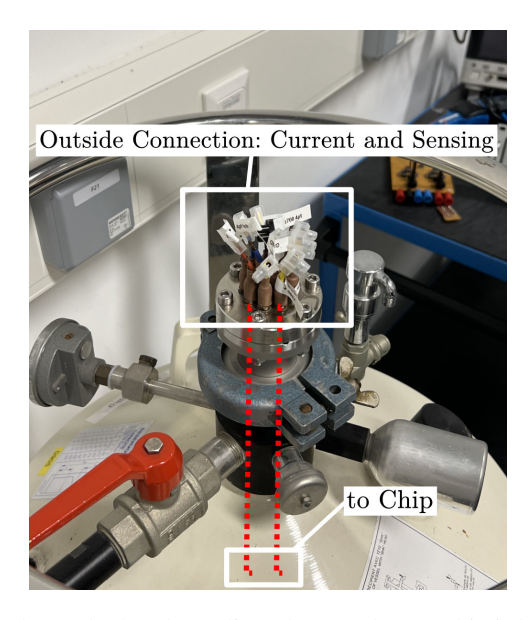


Figure 4.15: Image of feed through attached to the Helium dewar. The test chip is hanging into the dewar (indicated by dashed lines) and is held in place by the wires soldered onto the PCB that are connected to the feed through. The corresponding wires were connected to the sensing and protection circuit outside the dewar (not shown in the image).

#### 4.3.5 Results and Discussion

Here we discuss the results obtained from the critical current measurements for the test chip and the experiment chip. The measured critical currents for the test chip are summarized in Fig. 4.16(a). The first important observation is that the 100  $\mu$ m wire reaches 2 A while staying superconducting which is the required current for the atom trapping. The measured critical current  $I_c$  of about 2.75 A agrees reasonably well with the estimated critical current of  $I_c \approx 2.9$  A [62]. The smaller critical current is expected due to the sharp beding of the wires that can lead to current crowding [119]. The wires show an increase of the measured critical current with the wire width, which is expected as more current can flow at the same current density due to the larger wire cross-section. One thing to notice is the small critical current of the 50  $\mu$ m wire compared to the other ones.

To understand the measured data, we will take a look into the expected dependence. In the ideal case of a uniform current distribution across the entire cross-section of the wire, the critical current  $I_c$  is reached when the current density equals the depairing limit. In this regime, the maximum current is directly proportional to the wire width [103]:

$$I_c \propto w$$
. (4.18)

However, this assumption is only valid for thin wires where the magnetic self-field can be neglected. In our case, the wire width ( $\sim 100 \, \mu m$ ) is much larger than both the thickness (500 nm) and the London penetration depth ( $\sim 100 \, nm$  [62]). Under these conditions, the current distribution is modified by the wire's self-field, and the critical current is instead expected to follow a square-root dependence [120]:

$$I_c \propto \sqrt{w}$$
 (4.19)

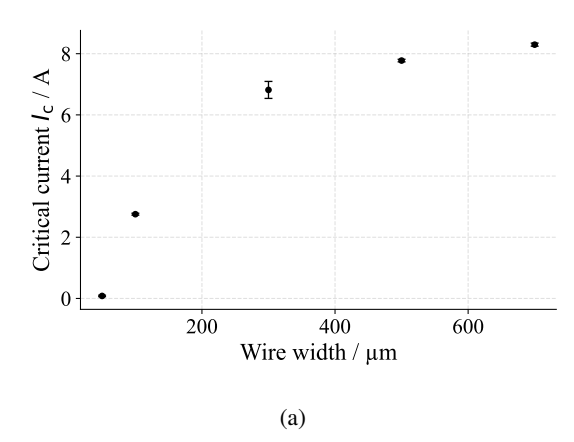
A further reduction is expected due to geometry. The trapping wires contain multiple 90° bends, which are known to induce current crowding at the inner corners, suppressing the critical current below the straight-wire limit [119]. This effect is also width-dependent.

From the measured data in Fig. 4.16(b) it becomes clear that the increase of the critical current with the wire width is smaller than Eq. (4.19) suggest for wires of width  $> 100\,\mu m$ . This indicates two points, first that we are most likely self-field-limited and second that the 90 degree turns seem to have significant influence on the critical current. The low critical current in the  $50\,\mu m$  wire may be attributed either to stronger current crowding at small widths or to a fabrication defect.

These observations suggest that if the critical current of a trapping wire becomes a limiting element in future designs, the geometry should be optimized, for example by replacing sharp corners with rounded ones, to mitigate current crowding and increase the critical current [119].

For the experiment chip, the important results are depicted in Fig. 4.17. Here, the measured current and the measured amplified voltage drop across the chip are shown as a function of time (current was increased over time by hand). The lower plots show the calculated resistance using Eq. (4.16) and a potentiometer value during this measurement of  $18 \, \mathrm{k}\Omega$ .

A jump of the voltage drop across the chip and a dip in the current occurs at  $I \approx 2.8$  A which agrees well with the previously measured value of  $I_c = 2.75$  A on the test chip. This indicates that this jump arises due to the breakdown of the supercoductivity of the whole wire. The increase in resistance of  $\sim 10 \text{ m}\Omega$  qualitatively agrees with the expected resistance jump from Section 4.3.2. However, these were not the only observed resistance jumps. In Fig. 4.17(b), two distinct jumps in the voltage drop across the chip are observed at around 0.6 A. These jumps were reproducable within the range of 0.6 A - 0.9 A.



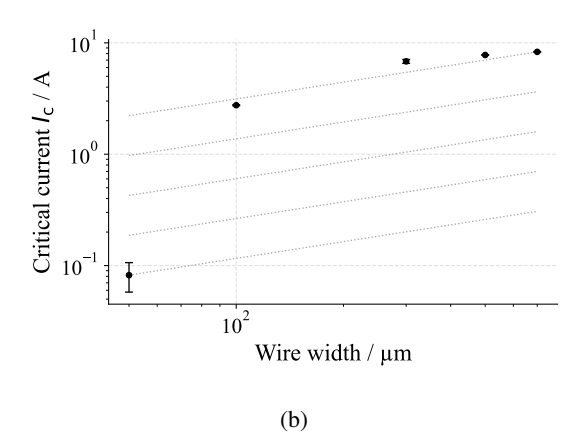


Figure 4.16: (a) Measured critical current of z-shaped superconducting niobium wires on the test chip as a function of wire width. The  $100 \, \mu m$  wire reaches the atom trapping requirement of 2 A. The small critical current of the  $50 \, \mu m$  wire is discussed in the main text. Error bars are the standard deviation of multiple measurements per wire. (b) Shows same data as in (a), but shown on a log-log scale. A slope of 1/2 is included in the plot for comparison.

The calculated resistance jumps are shown in the bottom which are on the order of  $\sim 1~\text{m}\Omega$ . The origin of these jumps is not fully clear. A possible explanation could be that parts of the wire become normal conducting near the pads for wirebonding due to local heating at the wirebonds or current crowding [119] at the wire bends. This would agree that always two jumps appear at similar current values. This would be expected if the cause is at the wirebond pads as we have the same geometry of them on both sides. The fact that the resistance jump is an order of magnitude smaller than the one at 2.8 A also indicates that not the whole wires changes to the normal conducting state. This measurement motivated the increase of the size of the bondpads for the z-wire from  $200~\mu\text{m} \times 700~\mu\text{m}$  to  $800~\mu\text{m} \times 1~300~\mu\text{m}$ , which we already saw in the beginning in Fig. 4.1.

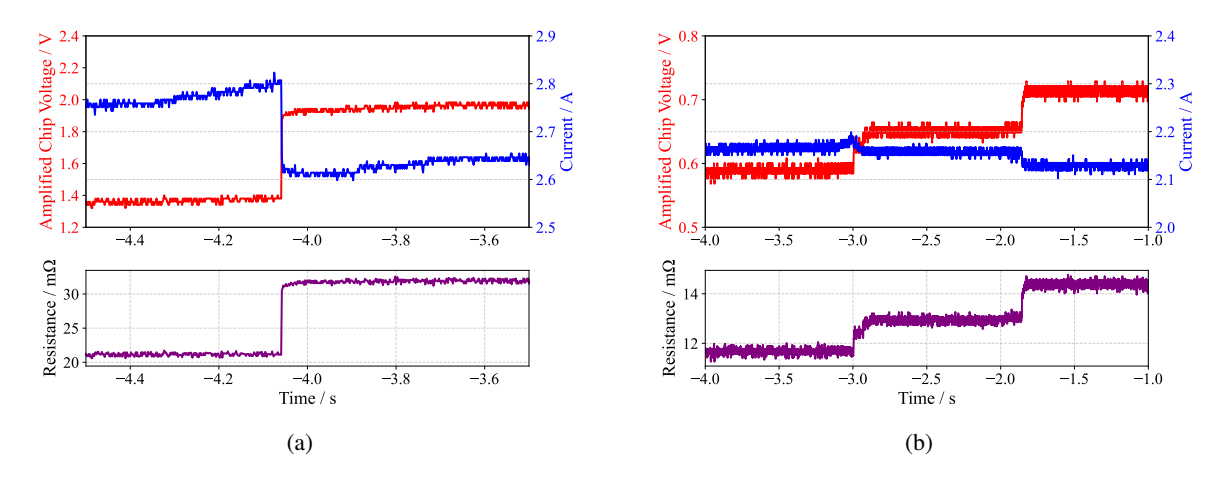


Figure 4.17: (a) Time trace of the experiment chip current (blue) and the amplified voltage drop across the chip (red). A distinct current drop at approximately 2.8 A, accompanied by a simultaneous voltage rise, indicates the transition out of the superconducting state. This critical current is consistent with the values shown in Fig. 4.16(a). (b) Time trace showing two separate voltage jumps (red), each accompanied by a small reduction in current (blue), reproducibly observed within the range  $0.6 \, \mathrm{A} - 0.9 \, \mathrm{A}$ . The lower panels display the corresponding resistance, calculated as  $R = U_c/G_c I$  using a potentiometer setting of  $18 \, \mathrm{k}\Omega$  for the instrumentation amplifier gain.

### **Conclusion and Outlook**

In this thesis, significant steps towards interfacing Rydberg atoms with a high-overtone bulk acoustic wave resonator (HBAR) were taken. An analytic model for the evanescent electric field of the resonator was developed. It allowed for an understanding of the piezoelectric effect that can mediate atom-phonon coupling and to derive scaling laws of the electric field in dependence of important system parameters such as the resonance frequency. Building on this, numerical electrostatic simulations were performed to obtain quantitative results for the single phonon electric field. This enabled the determination of the electric field in dependence of all experimentally tunable system parameters, i.e., the resonator frequency, the resonator thickness, the resonator mode waist and the atom-surface distance. Building on these results, the single phonon Rabi frequency of Rydberg atoms coupled to the HBAR was determined. The results showed that single phonon Rabi frequencies in the 20 kHz regime are achievable with realistic experimental parameters. Comparing this to the expected decay rates of both systems, about 1 kHz for the Rydberg atoms and below 1 kHz for the HBAR, indicates that the strong coupling regime is within reach.

As the experiment will be conducted in a cryogenic environment at finite temperatures around 4 K, the HBAR will be thermally occupied by phonons. For the targeted frequency of 5.8 GHz, a mean thermal phonon occupation of about 14 phonons is expected. The first goal of the HQO experiment is to cool the HBAR to its quantum mechanical ground state using Rydberg atoms as an active cooling agent. To assess the feasibility of this, an appropriate master equation model for a continuous-wave-based cooling scheme using collective Rydberg excitations, so-called superatoms, was developed and numerically solved. The results revealed superiority of using *N* collective Rydberg excitations in a cloud of atoms compared to *N* single Rydberg atoms in terms of cooling performance. Using experimentally achievable parameters, already four Rydberg superatoms would theoretically be enough to reduce the mean phonon occupation inside the resonator below 0.5.

In parallel to the theoretical and numerical studies, this thesis also included the characterization and design adaptations of a first-generation atom chip without the HBAR. This device, incorporating a superconducting wire trap and a coplanar waveguide resonator, should serve as a testbed to establish atom trapping, Rydberg excitation, and microwave coupling in a cryogenic-compatible chip environment. During the work of this thesis, the coplanar waveguide resonator characterization measurements were analyzed. A model including an adapted substrate permittivity, the temperature-dependent kinetic inductance and frequency shifts due to external coupling allowed to understand systematic frequency shifts of the resonator resonance. Beyond the microwave resonator, superconducting trapping wires of different

widths were characterized at liquid helium temperatures. It allowed for important design adaptations of the trapping wire on the experiment chip regarding the pads for wire bonds and showed that expected currents for magnetic trapping can run through the wire without them leaving the superconducting state. Furthermore, the measurements provide references for possible future trapping wires of different geometries.

To conclude, the key outcome of this thesis is the ability to quantitatively evaluate the coupling strength between a Rydberg atom and an HBAR as a function of experimentally tunable parameters, together with the theoretical demonstration that ground state cooling of an HBAR is feasible using collective Rydberg excitations as an active cooling agent.

#### **Outlook**

Theoretical numbers are known now. The next step is to integrate an HBAR into an atom chip design that enables trapping of atoms at distances of 35–50 µm from the resonator surface to enable interaction between the atoms and the HBAR. As an intermediate step, a chip that combines a microwave resonator with an HBAR—so the HBAR can be driven classically by an external source—would provide strong classical atom—HBAR coupling and a practical first step before single-phonon interactions. In this regime the atoms can also serve as probes of the resonator surface (e.g., mapping adsorbate-induced stray fields). Here, care must be taken to stay in the undercoupled regime such that the quality factor is still determined by the high intrinsic quality factor of the HBAR and not through the external coupling [87]. In parallel with HBAR integration, effort should also be devoted to implementing a well-engineered electrode setup for stray electric field compensation, which is essential for stable Rydberg excitation close to the resonator surface as one expects adsorbate electric fields close to it [88–91] that can shift the Rydberg atoms out of resonance. Altogether, this platform provides a promising route to study interactions between atoms and a macroscopic mechanical resonator.

# **Appendix**

# A.1 FEM Eigenfrequency Study: Mesh Refinenment of inner Quad Mesh of HBAR

As an example, the variation of the quad mesh element number (inner mesh of HBAR) is shown in Fig. A.1. Here, a Gaussian function was fitted to the simulated strain profile inside the piezo. The plots show results from the fit: Strain amplitude, center position, mode waist and relative deviation between simulated strain profile and fitted Gaussian. All other mesh parmeters were kept constant. A number of 12 was found to be the optimum with a relative deviation from the fit bellow a percent.

The same methode was used for the mapped mesh (region between inner cylinder and outer free tetrahedal region) and the number of mesh elements of the swept mesh along the *z*-direction.

### A.2 Cooling Simulations: System Hamiltonian

The explicit atomic Hamiltonian is given by:

where  $\omega_w$ ,  $\omega_p$ , and  $\omega_E$  are the energies of the states  $|W\rangle$ ,  $|P\rangle$ , and  $|E\rangle$ , respectively. The Hamiltonian of the resonator mode is a simple harmonic oscillator (zero-point energy is dropped):

$$H_{\rm osc} = \omega_m \hat{a}^{\dagger} \hat{a} \tag{A.2}$$

where  $\hat{a}$  and  $\hat{a}^{\dagger}$  are the annihilation and creation operators for the resonator mode, respectively, and  $\omega_m$  is the frequency of the resonator mode. The interaction Hamiltonian describes the coupling between the upper Rydberg state and the bright and dark Rydberg state via the resonator mode. Here, the rotating

#### Mesh Refinement Study: Acoustic Eigenfrequency

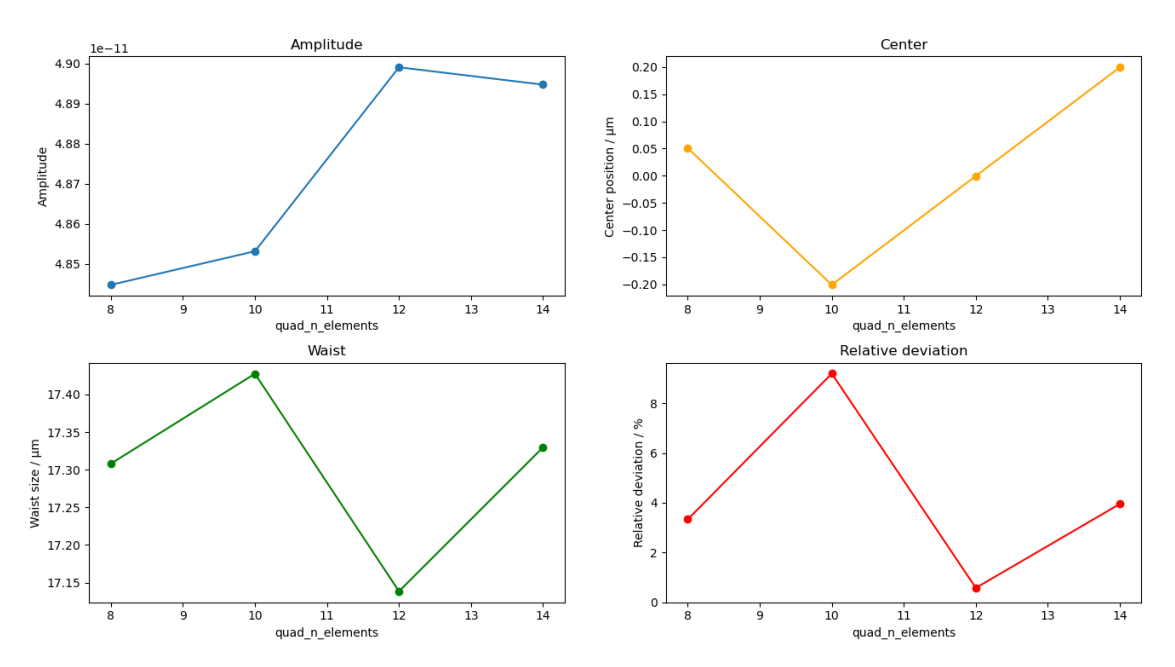


Figure A.1: Mesh refinement study for FEM eigenfrequency analysis. Here, the number of quad mesh elements in the inner cylinder of the HBAR was varied. A Gaussian function was fitted to the strain profile inside the piezo. The four plots show results from the fit: Strain amplitude, center position, mode waist and relative deviation between simulated strain profile and fitted Gaussian. All other mesh parmeters were kept constant. A number of 12 was found to be the optimum with a relative deviation from the fit bellow a percent.

wave approximation is alreay applied:

$$H_{\text{int}} = \frac{\Omega_{\text{HBAR}}}{2} \left( |P\rangle \left( \langle D| + \langle W| \right) \otimes \hat{a} + (|D\rangle + |W\rangle \right) \langle P| \otimes \hat{a}^{\dagger} \right). \tag{A.3}$$

We now transform the atomic Hamiltonian into an appropriate rotating frame where we can apply the rotating wave approximation using the unitary transformation

$$U = \sum_{i}^{N} e^{-i\omega_{i}t} |i\rangle \langle i|$$
(A.4)

$$\left\{\omega_{i}\right\}_{i=1}^{5}=\left\{1,\,\Delta+\omega_{W},\,\Delta+\omega_{W},\,\Delta+\omega_{P}-\omega_{c},\,\Delta-\Delta'-\omega_{m}+\omega_{E}\right\}$$

where  $\Delta = \omega - (\omega_W - \omega_G)$  and  $\Delta' = \omega' - (\omega_P - \omega_E)$  are the detunings of the two-photon transitions from the respective atomic transitions, and  $\omega_m = \omega_P - \omega_W$  is the Rydberg transition frequency which is set to be resonant with the resonator mode frequency.

The transformed Hamiltonian is then given by [92]:

$$H = U^{\dagger} H U - i U^{\dagger} \dot{U} \tag{A.5}$$

After transforming the Hamiltonian we arrive at the following time-dependent atomic Hamiltonian:

$$H_{\rm atom} = \begin{bmatrix} 0 & \frac{1}{2} \left( 1 + e^{-2it\omega} \right) \Omega & 0 & 0 & 0 \\ \frac{1}{2} \left( 1 + e^{2it\omega} \right) \Omega & -\Delta & 0 & 0 & 0 \\ 0 & 0 & -\Delta & 0 & 0 \\ 0 & 0 & 0 & -(\Delta - \omega_m) & \frac{1}{2} \left( 1 + e^{2it\omega'} \right) \Omega' \\ 0 & 0 & 0 & \frac{1}{2} \left( 1 + e^{-2it\omega'} \right) \Omega' & -(\Delta - \Delta' - \omega_m) \end{bmatrix} \tag{A.6}$$

We now apply the rotating wave approximation (RWA) by neglecting all oscillating terms in Eq. (A.6). We end up with the system Hamiltonian from Eq. (3.17) in Section 3.3.1.

### A.3 Statement on Digital Tools and Al Assistance

In the preparation of this thesis, digital tools—including AI-based assistance—were used for supporting tasks such as language polishing, code writing for data plotting and analysis, code debugging, code documentation and document formatting (see Table A.1). All results were verified independently by the author.

Table A.1: Overview of digital and AI-based tools structured by purpose of use.

Task / Purpose	Tools Used	Role of the Tools
Writing and Language Polishing	ChatGPT, GitHub Copilot	Grammar correction, spelling checks, sentence restructuring for clarity, sentence suggestions, synonym search, and text structuring.
LaTeX Formatting and Typesetting	ChatGPT, GitHub Copilot	Assistance with LaTeX syntax, table formatting, and reference styling.
Coding and Debugging	ChatGPT, GitHub Copilot, Gemini	Code writing for data plotting and analysis, code documentation, code debugging. Numerical models and simulations were designed and verified by the author.
Literature Search	ChatGPT, Perplexity, Gemini	Literature search.
Plotting of Data	Matplotlib (Python), COM-SOL	Plotting of data and plots exported in COMSOL
Data Analysis	Scipy (Python)	Fitting of functions to data

# **Bibliography**

- [1] G. Kurizki et al., *Quantum Technologies with Hybrid Systems*, Proceedings of the National Academy of Sciences **112** (2015) 3866.
- [2] M. Wallquist, K. Hammerer, P. Rabl, M. Lukin and P. Zoller, Hybrid Quantum Devices and Quantum Engineering, Physica Scripta 2009 (2009) 014001, ISSN: 1402-4896.
- [3] A. Reiserer and G. Rempe, Cavity-Based Quantum Networks with Single Atoms and Optical Photons, Reviews of Modern Physics 87 (2015) 1379.
- [4] Y. Kubo et al., *Strong Coupling of a Spin Ensemble to a Superconducting Resonator*, Physical Review Letters **105** (2010) 140502.
- [5] A. S. Sørensen, C. H. van der Wal, L. I. Childress and M. D. Lukin, *Capacitive Coupling of Atomic Systems to Mesoscopic Conductors*, Physical Review Letters **92** (2004) 063601.
- [6] Y. Chu et al., Quantum Acoustics with Superconducting Qubits, Science 358 (2017) 199.
- [7] Z.-L. Xiang, S. Ashhab, J. Q. You and F. Nori, *Hybrid Quantum Circuits: Superconducting Circuits Interacting with Other Quantum Systems*, Reviews of Modern Physics **85** (2013) 623.
- [8] M.-H. Jiang et al., *Quantum Storage of Entangled Photons at Telecom Wavelengths in a Crystal*, Nature Communications **14** (2023) 6995, ISSN: 2041-1723.
- [9] X.-L. Pang et al., A Hybrid Quantum Memory–Enabled Network at Room Temperature, Science Advances 6 (2020) eaax1425.
- [10] T. Blésin et al., Bidirectional Microwave-Optical Transduction Based on Integration of High-Overtone Bulk Acoustic Resonators and Photonic Circuits, Nature Communications 15 (2024) 6096, ISSN: 2041-1723.
- [11] Optical Readout of a Superconducting Qubit Using a Piezo-Optomechanical Transducer, ().
- [12] S. G. Menon, N. Glachman, M. Pompili, A. Dibos and H. Bernien, An Integrated Atom Array-Nanophotonic Chip Platform with Background-Free Imaging, Nature Communications 15 (2024) 6156, ISSN: 2041-1723.
- [13] X. Zhang, A Review of Common Materials for Hybrid Quantum Magnonics, Materials Today Electronics 5 (2023) 100044, ISSN: 2772-9494.

- [14] T. F. Gallagher, *Rydberg Atoms*, Cambridge Monographs on Atomic, Molecular and Chemical Physics, Cambridge: Cambridge University Press, 1994, ISBN: 978-0-521-02166-1.
- [15] P. Kharel et al., *Ultra-High-Q Phononic Resonators on-Chip at Cryogenic Temperatures*, APL Photonics **3** (2018) 066101, ISSN: 2378-0967.
- [16] M. Saffman, T. G. Walker and K. Mølmer, *Quantum Information with Rydberg Atoms*, Reviews of Modern Physics **82** (2010) 2313.
- [17] V. Bendkowsky et al., *Observation of Ultralong-Range Rydberg Molecules*, Nature **458** (2009) 1005, ISSN: 1476-4687.
- [18] F. Camargo et al., *Creation of Rydberg Polarons in a Bose Gas*, Physical Review Letters **120** (2018) 083401.
- [19] S. de Léséleuc et al., Observation of a Symmetry-Protected Topological Phase of Interacting Bosons with Rydberg Atoms, Science **365** (2019) 775.
- [20] T. Peyronel et al.,

  Quantum Nonlinear Optics with Single Photons Enabled by Strongly Interacting Atoms,
  Nature 488 (2012) 57, ISSN: 1476-4687.
- [21] C. Qiao et al.,

  Rydberg Blockade in an Ultracold Strontium Gas Revealed by Two-Photon Excitation Dynamics,
  Physical Review A 103 (2021) 063313.
- [22] A. P. Burgers et al., Controlling Rydberg Excitations Using Ion-Core Transitions in Alkaline-Earth Atom-Tweezer Arrays, PRX Quantum 3 (2022) 020326.
- [23] T.-L. Chen et al., Inverted-Ladder-Type Optical Excitation of Potassium Rydberg States with Hot and Cold Ensembles, Physical Review A 101 (2020) 052507.
- [24] M. Wu et al., *Electromagnetically Induced Transparency Spectra of 6Li Rydberg Atoms*, Photonics **10** (2023) 1367, ISSN: 2304-6732.
- [25] A. Paris-Mandoki et al., Free-Space Quantum Electrodynamics with a Single Rydberg Superatom, Physical Review X 7 (2017) 041010.
- [26] C. Tresp et al., *Single-Photon Absorber Based on Strongly Interacting Rydberg Atoms*, Physical Review Letters **117** (2016) 223001.
- [27] N. Stiesdal et al., *Controlled Multi-Photon Subtraction with Cascaded Rydberg Superatoms as Single-Photon Absorbers*, Nature Communications **12** (2021) 4328, ISSN: 2041-1723.
- [28] L. Ahlheit et al., *Magic Running- and Standing-Wave Optical Traps for Rydberg Atoms*, Physical Review A **111** (2025) 013115.
- [29] S. Anand et al., *A Dual-Species Rydberg Array*, Nature Physics **20** (2024) 1744, ISSN: 1745-2481.
- [30] J. A. Sedlacek et al.,

  Microwave Electrometry with Rydberg Atoms in a Vapour Cell Using Bright Atomic Resonances,

  Nature Physics 8 (2012) 819, ISSN: 1745-2481.

- [31] H. Fan et al., *Atom Based RF Electric Field Sensing*, Journal of Physics B: Atomic, Molecular and Optical Physics **48** (2015) 202001, ISSN: 0953-4075.
- [32] Y. Cui et al., Extending Bandwidth Sensitivity of Rydberg-atom-based Microwave Electrometry Using an Auxiliary Microwave Field, Physical Review A 107 (2023) 043102.
- [33] L. Ma, M. A. Viray, D. A. Anderson and G. Raithel, Measurement of Dc and Ac Electric Fields inside an Atomic Vapor Cell with Wall-Integrated Electrodes, Physical Review Applied 18 (2022) 024001.
- [34] S. Baur, D. Tiarks, G. Rempe and S. Dürr, *Single-Photon Switch Based on Rydberg Blockade*, Physical Review Letters **112** (2014) 073901.
- [35] A. Browaeys, D. Barredo and T. Lahaye, Experimental Investigations of Dipole–Dipole Interactions between a Few Rydberg Atoms, Journal of Physics B: Atomic, Molecular and Optical Physics 49 (2016) 152001, ISSN: 0953-4075.
- [36] M. D. Lukin et al.,

  Dipole Blockade and Quantum Information Processing in Mesoscopic Atomic Ensembles,
  Physical Review Letters 87 (2001) 037901.
- [37] D. Bluvstein et al., Logical Quantum Processor Based on Reconfigurable Atom Arrays, Nature **626** (2024) 58, ISSN: 1476-4687.
- [38] S. J. Evered et al., *High-Fidelity Parallel Entangling Gates on a Neutral-Atom Quantum Computer*, Nature **622** (2023) 268, ISSN: 1476-4687.
- [39] Y. O. Dudin, L. Li, F. Bariani and A. Kuzmich, Observation of Coherent Many-Body Rabi Oscillations, Nature Physics 8 (2012) 790, ISSN: 1745-2481.
- [40] E. Urban et al., *Observation of Rydberg Blockade between Two Atoms*, Nature Physics **5** (2009) 110, ISSN: 1745-2481.
- [41] C. Hölzl, A. Götzelmann, E. Pultinevicius, M. Wirth and F. Meinert, Long-Lived Circular Rydberg Qubits of Alkaline-Earth Atoms in Optical Tweezers, Physical Review X 14 (2024) 021024.
- [42] T. F. Gallagher and W. E. Cooke, *Interactions of Blackbody Radiation with Atoms*, Physical Review Letters **42** (1979) 835.
- [43] N. Schlossberger et al., Primary Quantum Thermometry of Mm-Wave Blackbody Radiation via Induced State Transfer in Rydberg States of Cold Atoms,
  Physical Review Research 7 (2025) L012020.
- [44] T. Cantat-Moltrecht et al., Long-Lived Circular Rydberg States of Laser-Cooled Rubidium Atoms in a Cryostat, Physical Review Research 2 (2020) 022032.
- [45] H. Y. Chen, E. R. MacQuarrie and G. D. Fuchs, Orbital State Manipulation of a Diamond Nitrogen-Vacancy Center Using a Mechanical Resonator, Physical Review Letters 120 (2018) 167401.

- [46] U. von Lüpke, *Quantum Control of a Multimode Bulk Acoustic Wave Resonator*, Doctoral Thesis: ETH Zurich, 2023.
- [47] L. Tenbrake, A. Faßbender, S. Hofferberth, S. Linden and H. Pfeifer, Direct Laser-Written Optomechanical Membranes in Fiber Fabry-Perot Cavities, Nature Communications 15 (2024) 209, ISSN: 2041-1723.
- [48] A. H. Ghadimi et al., *Elastic Strain Engineering for Ultralow Mechanical Dissipation*, Science **360** (2018) 764.
- [49] R. Manenti et al., Circuit Quantum Acoustodynamics with Surface Acoustic Waves, Nature Communications 8 (2017) 975, ISSN: 2041-1723.
- [50] H. H. Diamandi et al., Optomechanical Control of Long-Lived Bulk Acoustic Phonons in the Quantum Regime, Nature Physics 21 (2025) 1482, ISSN: 1745-2481.
- [51] M. Bonaldi et al., *Probing Quantum Gravity Effects with Quantum Mechanical Oscillators*, The European Physical Journal D **74** (2020) 178, ISSN: 1434-6079.
- [52] S. Marti et al., *Quantum Squeezing in a Nonlinear Mechanical Oscillator*, Nature Physics **20** (2024) 1448, ISSN: 1745-2481.
- [53] Y. Chu et al., Creation and Control of Multi-Phonon Fock States in a Bulk Acoustic-Wave Resonator, Nature 563 (2018) 666, ISSN: 1476-4687.
- [54] A Mechanical Qubit, URL: https://www.science.org/doi/10.1126/science.adr2464 (visited on 18/08/2025).
- [55] S. Meesala et al., *Strain Engineering of the Silicon-Vacancy Center in Diamond*, Physical Review B **97** (2018) 205444.
- [56] M. Gao, Y.-x. Liu and X.-B. Wang, Coupling Rydberg Atoms to Superconducting Qubits via Nanomechanical Resonator, Physical Review A 83 (2011) 022309.
- [57] J. Gamper, Frequenzstabilisierung Zur Laserkühlung von Rubidium, BA thesis: University of Bonn, 2022.
- [58] S. Germer, Frequency Stabilization of a Laser and a High Resolution Optical Setup for Excitation of Ultracold Rydberg Atoms, BA thesis: University of Bonn, 2023.
- [59] H. Hattermann et al.,

  Coupling Ultracold Atoms to a Superconducting Coplanar Waveguide Resonator,

  Nature Communications 8 (2017) 2254, ISSN: 2041-1723.
- [60] J. Gamper, *Atom Preparation and Rydberg Excitation of Rubidium Atoms*, MA thesis: University of Bonn, 2024.
- [61] V. Mauth, Machine Learning Based Optimization for the Preparation of Rubidium Rydberg Atoms and Characterization of the Detection, MA thesis: University of Bonn, 2025.
- [62] L. Sadowski, *Design of a Superconducting Atom Chip for Interfacing Rydberg Atoms with Microwave Resonators*, MA thesis: University of Bonn, 2024.

- [63] N. Šibalić, J. D. Pritchard, K. J. Weatherill and C. S. Adams, *ARC: An open-source library for calculating properties of alkali Rydberg atoms*, Computer Physics Communications **220** (2017) 319.
- [64] C. Kittel, *Introduction to Solid State Physics*, 8. ed., internat. ed., Hoboken, NJ: Wiley, 2005, ISBN: 978-0-471-68057-4.
- [65] J. Aramburu, P. Garcia-Fernandez, J. M. García-Lastra, M. Barriuso and M. Moreno, *Internal Electric Fields and Color Shift in Cr*\{3+\}-Based Gemstones, Phys. Rev. B **85** (2012).
- [66] P. L. Gould and Y. Feng, *Introduction to Linear Elasticity*, Cham: Springer International Publishing, 2018, ISBN: 978-3-319-73884-0 978-3-319-73885-7.
- [67] M. J. Musgrave,

  Crystal Acoustics Introduction to the Study of Elastic Waves and Vibrations in Crystals,

  Holden-Day Series in Mathematical Physics, Holden-Day, 1970.
- [68] COMSOL Multiphysics Reference Manual, URL: https://doc.comsol.com/5.5/doc/com.comsol.help.comsol/COMSOL\_ReferenceManual.pdf (visited on 06/10/2025).
- [69] COMSOL 6.3 Solid Mechanics Material Properties,
  URL: https://doc.comsol.com/6.3/doc/com.comsol.help.comsol/comsol\_ref\_
  materials.25.48.html (visited on 20/08/2025).
- [70] R. B. Thompson and B. P. Newberry, A Paraxial Theory for the Propagation of Ultrasonic Beams in Anisotropic Solids, URL: https://dr.lib.iastate.edu/entities/publication/3a722db0-9309-4500-9ad7-24c8534b9762 (visited on 16/01/2025).
- [71] W. G. Cady, Piezoelectricity An Introduction To The Theory and Applications Of Electromechanical Phenomena In Crystals, Mcgraw Hill Book Co, 1946.
- [72] J. F. Nye, *Physical Properties of Crystals Their Representation by Tensors and Matrices*, Reprint., Oxford Science Publications, Oxford: Clarendon Press, 1998, xvii+329, ISBN: 978-0-19-851165-6.
- [73] J. Yang, *An Introduction to the Theory of Piezoelectricity*, vol. 9, Advances in Mechanics and Mathematics, Cham: Springer International Publishing, 2018, ISBN: 978-3-030-03136-7 978-3-030-03137-4.
- [74] A. Arnau, Piezoelectric Transducers and Applications.
- [75] S. Sherrit and B. K. Mukherjee, *Characterization of Piezoelectric Materials for Transducers*, 2007, arXiv: 0711.2657 [cond-mat], URL: http://arxiv.org/abs/0711.2657 (visited on 05/10/2025), pre-published.
- [76] X. Zhao, L. Colombo and C. Cassella, *Aluminum Nitride Two-Dimensional-Resonant-Rods*, Applied Physics Letters **116** (2020) 143504, ISSN: 0003-6951.
- [77] F. Bernardini, V. Fiorentini and D. Vanderbilt, Spontaneous Polarization and Piezoelectric Constants of III-V Nitrides, Physical Review B **56** (1997) R10024.
- [78] S. T. Haider, M. A. Shah, D.-G. Lee and S. Hur, A Review of the Recent Applications of Aluminum Nitride-Based Piezoelectric Devices, IEEE Access 11 (2023) 58779, ISSN: 2169-3536.

- [79] H. Banderier, M. Drimmer and Y. Chu, Unified Simulation Methods for Quantum Acoustic Devices, Physical Review Applied 20 (2023) 024024.
- [80] D. A. Steck, Quantum and Atom Optics, URL: https://atomoptics.uoregon.edu/~tbrown/files/relevant\_papers/quantum-optics-notes.pdf (visited on 06/10/2025).
- [81] P. R. Gomez, Engineering Eigenstates in High-Overtone Bulk Acoustic Resonators, MA thesis: ETH Zürich.
- [82] S. Marti, Optimization of Phononic Radiation Loss Patterns in a High Overtone Bulk Acoustic Resonator, MA thesis: ETH Zürich, 2022.
- [83] J. D. Jackson, *Klassische Elektrodynamik*, 5. überarb. Aufl, De Gruyter Studium, Berlin; Boston: De Gruyter, 2013, 957 pp., ISBN: 978-3-11-033447-0.
- [84] COMSOL: Multiphysics Software for Optimizing Designs, COMSOL, URL: https://www.comsol.com/ (visited on 05/10/2025).
- [85] I. L. Guy, S. Muensit and E. M. Goldys, Extensional Piezoelectric Coefficients of Gallium Nitride and Aluminum Nitride, Applied Physics Letters 75 (1999) 4133, ISSN: 0003-6951.
- [86] H. Banderier, Towards a Hybrid EPR Method for cQAD Devices, MA thesis: ETH Zürich.
- [87] M. Göppl et al., Coplanar Waveguide Resonators for Circuit Quantum Electrodynamics, Journal of Applied Physics **104** (2008) 113904, ISSN: 0021-8979.
- [88] H. Hattermann et al.,

  Detrimental Adsorbate Fields in Experiments with Cold Rydberg Gases near Surfaces,
  Physical Review A 86 (2012) 022511.
- [89] A. Tauschinsky, R. M. T. Thijssen, S. Whitlock, H. B. van Linden van den Heuvell and R. J. C. Spreeuw, Spatially Resolved Excitation of Rydberg Atoms and Surface Effects on an Atom Chip, Physical Review A 81 (2010) 063411.
- [90] K. S. Chan, M. Siercke, C. Hufnagel and R. Dumke, Adsorbate Electric Fields on a Cryogenic Atom Chip, Physical Review Letters 112 (2014) 026101.
- [91] P. L. Ocola et al.,

  Control and Entanglement of Individual Rydberg Atoms near a Nanoscale Device,
  Physical Review Letters 132 (2024) 113601.
- [92] M. D. Lukin, *Modern Atomic and Optical Physics II*, 2016, URL: https://lukin.physics.harvard.edu/sites/g/files/omnuum6416/files/lukin/files/physics\_285b\_lecture\_notes.pdf (visited on 06/10/2025).
- [93] M. Aspelmeyer, T. J. Kippenberg and F. Marquardt, *Cavity Optomechanics*, Reviews of Modern Physics **86** (2014) 1391, ISSN: 0034-6861, 1539-0756.

- [94] D. A. Cardwell, D. C. Larbalestier and A. Braginski, eds., Handbook of Superconductivity: Fundamentals and Materials, Volume One, 2nd ed., Boca Raton: CRC Press, 2022, 472 pp., ISBN: 978-0-429-17918-1.
- [95] H. Zu, W. Dai and A. T. A. M. de Waele, *Development of Dilution Refrigerators—A Review*, Cryogenics **121** (2022) 103390, ISSN: 0011-2275.
- [96] L. F. Keary and J. D. Pritchard, Strong Coupling and Active Cooling in a Finite-Temperature Hybrid Atom-Cavity System, Physical Review A 105 (2022) 013707, ISSN: 2469-9926, 2469-9934.
- [97] D. A. Steck, *Rubidium 87 D Line Data*, URL: https://www.steck.us/alkalidata/rubidium87numbers.1.6.pdf (visited on 09/09/2025).
- [98] R. Löw et al., *An Experimental and Theoretical Guide to Strongly Interacting Rydberg Gases*, Journal of Physics B: Atomic, Molecular and Optical Physics **45** (2012) 113001, ISSN: 0953-4075.
- [99] C. Mewes and M. Fleischhauer, *Decoherence in Collective Quantum Memories for Photons*, Physical Review A **72** (2005) 022327.
- [100] J. Honer, R. Löw, H. Weimer, T. Pfau and H. P. Büchler, *Artificial Atoms Can Do More Than Atoms: Deterministic Single Photon Subtraction from Arbitrary Light Fields*, Physical Review Letters **107** (2011) 093601.
- [101] B. Zhao et al., A Millisecond Quantum Memory for Scalable Quantum Networks, Nature Physics 5 (2009) 95, ISSN: 1745-2481.
- [102] J. R. Johansson, P. D. Nation and F. Nori,

  QuTiP: An Open-Source Python Framework for the Dynamics of Open Quantum Systems,

  Computer Physics Communications 183 (2012) 1760, ISSN: 00104655,

  arXiv: 1110.0573 [quant-ph].
- [103] M. Tinkham, *Introduction to Superconductivity*, 2. ed., International Series in Pure and Applied Physics, New York: McGraw-Hill, 1996, ISBN: 978-0-07-064878-4.
- [104] M. Kaiser et al., Cavity-Driven Rabi Oscillations between Rydberg States of Atoms Trapped on a Superconducting Atom Chip, Physical Review Research 4 (2022) 013207.
- [105] R. Garg, I. J. Bahl and M. Bozzi, *Microstrip Lines and Slotlines*, Third edition., Artech House Microwave Library, Boston: Artech House, 2013, ISBN: 978-1-60807-535-5.
- [106] R. Meservey and P. M. Tedrow,

  Measurements of the Kinetic Inductance of Superconducting Linear Structures,

  Journal of Applied Physics 40 (1969) 2028, ISSN: 0021-8979.
- [107] Coplanar Waveguide Analysis/Synthesis Calculator, URL: https://wcalc.sourceforge.net/cgi-bin/coplanar.cgi (visited on 01/10/2025).
- [108] K. Watanabe, K. Yoshida and T. A. Kohjiro, Kinetic Inductance of Superconducting Coplanar Waveguides, Japanese Journal of Applied Physics 33 (10R 1994) 5708, ISSN: 1347-4065.

- [109] J. R. Clem, *Inductances and Attenuation Constant for a Thin-Film Superconducting Coplanar Waveguide Resonator*, Journal of Applied Physics **113** (2013) 013910, ISSN: 0021-8979.
- [110] A. Morgan, *Coupling Rydberg Atoms to Superconducting Microwave Circuits*, PhD thesis: University College London, 2020.
- [111] Properties of sapphire substrate and sapphire wafers, URL: https://valleydesign.com/sappprop/ (visited on 06/10/2025).
- [112] J. Ekin, Experimental Techniques for Low-Temperature Measurements: Cryostat Design, Material Properties and Superconductor Critical-Current Testing, Illustrated edition, OUP Oxford, 2006, 704 pp.
- [113] CRC Handbook of Chemistry and Physics: A Ready-Reference Book of Chemical and Physical Data, Boca Raton: CRC Press, 2017, 2560 pp., ISBN: 978-1-4987-8454-2.
- [114] N. Morton, B. W. James, G. H. Wostenholm and R. J. Nichols, The Electrical Resistivity of Niobium and Niobium-Zirconium Alloys, Journal of Physics F: Metal Physics 5 (1975) 85, ISSN: 0305-4608.
- [115] S. Wilde et al., *Dc Magnetometry of Niobium Thin Film Superconductors Deposited Using High Power Impulse Magnetron Sputtering*,
  Physical Review Accelerators and Beams **21** (2018) 073101.
- [116] N. Martin et al.,

  Low Temperature Dependence of Resistivity in Obliquely Sputter-Deposited Gold Thin Films,

  Surface and Coatings Technology 499 (2025) 131884, ISSN: 0257-8972.
- [117] P. Horowitz, *The Art of Electronics*, 3. ed., Cambridge: Univ. Press, 2015, ISBN: 978-0-521-80926-9.
- [118] AC/DC Current Clamp CC-65, URL: https://www.hantek.com/products/detail/77 (visited on 01/09/2025).
- [119] J. R. Clem and K. K. Berggren, Geometry-Dependent Critical Currents in Superconducting Nanocircuits, Physical Review B **84** (2011) 174510.
- [120] A. A. Babaei Brojeny and J. R. Clem, Self-Field Effects upon the Critical Current Density of Flat Superconducting Strips, Superconductor Science and Technology 18 (2005) 888, ISSN: 0953-2048.

## **Acknowledgements**

I would like to thank Sebastian Hofferberth for giving me the opportunity to work on the HQO experiment during my Master thesis and especially for giving me the opportunity to visit the labs at Zurich during my thesis time. I really appreciate that you trust me and the things I work on (at least it seemed like that to me :D). For me, this makes a big difference and it keeps me motivated a lot. Furthermore, I thank Daqing Wang for being my second supervisor. Of course, I thank all my lab mates from the HQO experiment who were part of the team during my thesis. I would like to thank Cedric, for a lot of physics discussions and support you can count on. I had lots of fun dipping chips into liquid helium with you. I would like to thank Julia — it's super cool working with you and discussing physics. It's (as you would probably say) amazing to have someone you know is always supporting you. I would like to thank Valerie for physics discussions, who is also a person you can always count on. I would like to thank Leon for teaching me a lot of stuff about (previously completely unknown) physics to me. I especially want to thank Nina and Lukas A. who offered me a lot of support throughout my thesis. I send a big hug to Eduardo Esquivel, who is a super chill guy. We went out for bouldering (and food!) lots of times during my thesis and I hope to continue that some day. Furthermore, he was an integral part to get more NQO people motivated to go bouldering: D. I enjoyed time with all members of the NOQ group, the 11:30 people and the 12:15 people. I would like to thank Wolfgang, who is a big inspiration to me, especially in terms of caring about all the little details in physics that are important in order for things to work out.